INFILTRATION AND SOLID-LIQUID PHASE CHANGE IN POROUS MEDIA

A Dissertation

Presented to the Faculty of the Graduate School of

University of Missouri-Columbia

In Partial Fulfillment of the Requirements for the Degree of

Doctor of Philosophy

By

Piyasak Damronglerd

Dr. Yuwen Zhang Dissertation Supervisor

May 2009

The undersigned, appointed by the Dean of the Graduate Schoo1, have examined the dissertation entitled.

INFILTRATION AND SOLID-LIQUID PHASE CHANGE IN POROUS MEDIA

Presented by Piyasak Damronglerd

a candidate for the degree of Doctor of Philosophy

and hereby certify that in their opinion it is worthy of acceptance

_____

Dr. Yuwen Zhang

_____

Dr. Robert D. Tzou

_____

Dr. Carmen Chicone

_____

Dr. Hongbin Ma

_____

Dr. Douglas E. Smith

ACKNOWLEDGEMENT

I wish to thank Prof. Yuwen Zhang, who has been my excellent research adviser. Thank you for your constant support, unlimited patience, and enlightening guidance. Most importantly, I thank you for sharing your technical expertise.

I also would like to thank Dr. Robert Tzou, Dr. Hongbin Ma, Dr. Douglas E. Smith, and Dr. Carmen Chicone, who were my dissertation committee members and provided incisive guidance and sincere help.

I wish to thank Pat Frees and Melanie Gerlach for your help with staying on top of all the graduate work.

Finally, I would like to thank my family and my girlfriend for all your loves, supports, worries, suggestions, and patience. Thanks for always be there for me.

TABLE OF CONTENT

LIST OF FIGURES

LIST OF SYMBOLS

c	specific heat, ($J/kg \cdot K$)
c^0	coefficient for Forchheimer's extension
C	dimensionless coefficient for Forchheimer's extension, c^0/c_l
C_{sl}	dimensionless specific heat, c_s/c_l
C_v	heat capacity ($J/m^3 \cdot K$)
Da	Darcy's number
d	Coefficient in velocity correction
d_p	diameter of the particle in the laser sintered preform (m)
d_{ps}	particle diameter after partial solidification (m)
f	mass fraction of solid in the solidification region
F	F-function value
g	gravitational acceleration
H	height of the vertical wall (m)
$h_{s\ell}$	latent heat of melting or solidification, (J/kg)
k	thermal conductivity ($W/m \cdot K$)
K	dimensionless thermal conductivity
l	location of infiltration front (m)

L characteristic length (m)

L_x , L_y number of nodes on the X- and Y- direction

p pressure (Pa)

P dimensionless pressure difference

P^* initially guessed dimensionless pressure

P' dimensionless pressure correction

Pr Prandtl number, ν/α_l

Pr_l Prandtl number of liquid, ν_l / α_l

q_c'' average heat transfer rate on the right wall, W/m^2

Q_c dimensionless average heat transfer rate on the right wall, $q_c'' H / k_s (T_h^0 - T_m^0)$

Q_h dimensionless average heat transfer rate on the left wall, $q_h'' H / k_l (T_h^0 - T_m^0)$

Ra Raleigh number, $g\beta H^3 \left(T_h^0 - T_m^0\right) / \nu_l \alpha_l$

q_h'' average heat transfer rate on the left wall, W/m^2

s location of remelting front (m)

S dimensionless location of remelting front, s/L

Sc subcooling parameter, $(T_m - T_i)/(T_0 - T_m)$

S_c linearized source term

S_p linearized source term

Ste Stefan number, $c_l(T_0 - T_m)/h_{sl}$

T temperature (K)

t time (s)

T_0 inlet temperature of liquid metal (K)

T_i initial temperature of preform (K)

T_m melting point (K)

ΔT^0 one-half of phase change temperature range

ΔT one-half of dimensionless phase change temperature range

u superficial velocity (m/s)

U dimensionless superficial velocity (m/s)

V dimensionless liquid velocity in the Y- direction

V volume (m^3)

x vertical coordinate (m)

X dimensionless coordinate, x/L

Greek symbol

α thermal diffusivity (m^2/s)

$\bar{\alpha}_c$ dimensionless diffusivity in remelting region, eq.

β constant, $S/(2\sqrt{\tau})$

γ heat capacity ratio, $\rho_l c_l/(\rho_p c_p)$

δ constant, $\Delta/(2\sqrt{\tau})$

Δ dimensionless thermal penetration depth

ΔT $\Delta T^0/\left(T_h^0 - T_m^0\right)$

η similarity variable, $X/(2\sqrt{\tau})$

θ dimensionless temperature, $(T - T_m)/(T_0 - T_m)$

κ thermal conductivity ratio, k_l / k_p

λ constant, $\Lambda/(2\sqrt{\tau})$

Λ dimensionless infiltration front, l / L

μ viscosity (N-s/m^2)

ρ density (kg/m^3)

σ heat capacity of liquid in the remelting region,

τ dimensionless time, $\alpha_p t / L^2$

ε porosity (volume fraction of void), $(V_g + V_\ell)/(V_g + V_\ell + V_s)$

μ dynamic viscosity ($kg / m \cdot s$)

v liquid velocity in the y-direction (m / s)

φ porosity

φ_g volume fraction of gas, $V_g/(V_g + V_\ell + V_s)$

φ_ℓ volume fraction of liquid, $V_\ell/(V_g+V_\ell+V_s)$

φ_s volume fraction of solid, $V_s/(V_g+V_\ell+V_s)$

ϕ general dependent variable

ζ dimensionless permeability, K_e/K_l

Subscripts

c composite

E east neighbor of grid P

E control-volume face between P and E

eff effective

g gas

H High melting point powder

i initial

l liquid

L Low melting point powder

m melting point

N north neighbor of grid P

n control-volume face between P and N

nb neighbors of grid P

P grid point

p	preform
S	south neighbor of grid P
s	solid
W	west neighbor of grid P
w	control-volume face between P and W
0	surface

ABSTRACT

Many natural phenomenon and engineering systems involves phase change and infiltration in porous media. Some examples are the freezing of soil, frozen food, water barrier in construction and mining processes, chill casting [1], slab casting, liquid metal injection, latent-heat thermal-energy storage, laser annealing, selective laser sintering (SLS) and laser drilling, etc. These various applications are the motivation to develop a fast and reliable numerical model that can handle solid-liquid phase change and infiltration in porous media. The model is based on the Temperature Transforming Model (TTM) which use one set of governing equations for the whole computational domain, and then solid-liquid interface is located from the temperature distribution later. This makes the computation much faster, while it still provides reasonably accurate results. The first step was to create a model for solving Navier-Stokes and energy equation. The model was tested by solving a flow inside an enclosure problem. The next step was to implement TTM into the model to make it also capable of solving melting problem and then the program is tested with several phase change materials (PCM). The third step is to simplifying the complicated governing equations of melting and solidification in porous media problems into a simple set of equation similar to the Navier-Stokes equation, so that the program from previous step can be used. The final model was successfully validated by comparing with existing experimental and numerical results. Several controlling parameters of the phase change in porous media were studied. Finally, a one-dimensional infiltration process that involves both melting and resolidification of a selective laser sintering process was carefully investigated.

CHAPTER 1 INTRODUCTION

1.1. Introduction

Selective Laser Sintering (SLS) is a Rapid Prototyping (RP) technology that can fabricate complicated parts in a short time, and still keeps high quality with low costs. The process starts with 3D design in a Computer-Aided Design (CAD) program. SLS then constructs the part by melting and solidifying powder material layer by layer. The melting is obtained by projecting a laser beam onto a layer of powder bed. The laser beam scans the cross section of each layer by following the pattern in the 3D design.

However, the parts produced by SLS are usually not fully filled and have porous structure. In order to manufacture a fully densified part, post-processing is necessary. The existing post processing techniques include sintering, Hot Isostatic Pressing (HIP; [2]), and infiltration [3, 4]. Comparing to other post processes, infiltration can achieved full density without shrinkage and it is relatively inexpensive.

Infiltration uses capillary forces to draw liquid metal into the pores of a solid bed that caused by SLS of metal powder. The liquid advances into to solid and pushes vapor out, resulting in a relatively dense structure. The rate of infiltration depends on viscosity and surface tension of the liquid and the pore size of solid bed. Also, the natural convection must be considered because the infiltration is under the influence of gravity. In other words, capillary and gravitational forces are the major contributors in the infiltration process.

In order to draw liquid metal into the pores of the SLS parts, the liquid must be able to wet the solid and the surface tension of the liquid must be high enough to induce capillary

motion of the liquid metal into the pores of the compact solid. Consequently, the pore structure need to be interconnected and the pore size must not be too large or too small. The large pore size cannot produce sufficient capillary force, while the small pore size will create high friction which is not desirable in infiltration process. Tong and Khan [5] investigated infiltration and remelting in a two-dimensional porous preform. The driving force for the infiltration is an external pressure. The unique feature of infiltration is that solidification occurs and prevents the liquid metal to infiltrate to pores. Therefore, the solid bed must be preheated to a temperature near the melting point of the liquid metal. In addition, the temperature of the liquid metal must not be too high because melting of the solid bed may occur and the part may be distorted.

The challenge on modeling of the infiltration is that the part usually has complicated shape and the infiltration front will also has an irregular shape. Successful modeling of infiltration process requires correct handling of the complicated geometric shapes of the parts as well as the infiltration front. Also, the model must accurately simulate the melting and solidification processes to capture the movements of melting and resolidification fronts.

1.2. Modeling for Melting and Infiltration

Phase change heat transfer has received considerable attention in literature [6, 7] due to its importance in latent heat thermal energy storage devices [8-10] and many other applications. Many numerical models for melting and solidification of various Phase Change Materials (PCMs) have been developed. The numerical models can be divided into two groups [11]: *deforming grid schemes* (or strong numerical solutions) and *fixed grid schemes*

(or weak numerical solutions). Deforming grid schemes transforms solid and liquid phases into fixed regions by using a coordinate transformation technique. The governing equations and boundary conditions are complicated due to the transformation. These schemes have successfully solved multidimensional problems with or without natural convection. However, the disadvantage of deforming grid schemes is that it requires significant amount of computational time. On the other hand, fixed grid schemes use one set of governing equations for the whole computational domain including both liquid and solid phases, and solid-liquid interface is later determined from the temperature distribution. This simplicity makes the computation much faster than deforming grid schemes, while it still provides reasonably accurate results [12]. There are two main methods in the fixed grid schemes: the enthalpy method and the equivalent heat capacity method. The enthalpy method [13] can solve heat transfer in mushy zone but has difficulty with temperature oscillation, while the equivalent heat capacity method [14, 15] requires large enough temperature range in mushy zone to obtain converged solution.

Cao and Faghri [16] combined the advantages of both enthalpy and equivalent heat capacity methods and proposed a Temperature Transforming Model (TTM) that could also account for natural convection. TTM converts the enthalpy-based energy equation into a nonlinear equation with a single dependent variable – temperature. In order to use the TTM in solid-liquid phase change problems, it is necessary to make sure that the velocity in the solid region is zero. In the liquid region the velocity must be solved from the corresponding momentum and continuity equations. There are three wildly used velocity correction methods [17]: Switch-Off Method (SOM) [18], Source Term Method (STM), and Variable Viscosity Method (VVM). Voller [17] compared these three methods and concluded that

STM is the most stable method for phase-change problem. Ma and Zhang [19] proposed two modified methods that can be used with TTM: the Ramped Switch-Off Method (RSOM) and the Ramped Source Term Method (RSTM). These two methods were modified from the original Switch-Off Method (SOM) and the Source Term Method (STM) in order to eliminate discontinuity between two phases.

Because infiltration process involves at least two fluids: liquid metal and existing air, a special care must be taken to separate the fluids with a sharp interface. We will study the melting and resolidification of a selective laser sintering process. The program we develop will allow both incompressible and compressible fluid, and also blocking of any combinations of computational cells

Because infiltration process involves phase change between solid and liquid and interaction between the liquid and air inside the pores, the program that will be developed for this research will base on the ideas of TTM for melting and solidification, RSOM for handling the solid-velocity.

1.3. Dissertation Objectives

The goal of this research is to develop a program capable of simulating the complicated nature of infiltration process. In order to develop a program for post processing, certain steps must be taken in order to verify the accuracy and the validity of the program. The first step is to write a program for solving Navier-Stokes and energy equation. The program is tested by solving a flow inside an enclosure problem. The next step is to implement TTM model into the program to make it also capable of solving melting problem and then the program is

tested with several phase change materials (PCM). The third step is to simplifying the complicated governing equations of melting in porous media problems into a simple set of equation similar to the Navier-Stokes equation, so that the program from previous step can be used. Finally, we will study a one-dimensional infiltration process that involves both melting and resolidification of a selective laser sintering process.

1.3.1. Flow in Porous Media

A numerical study of transient fluid flow and heat transfer in a porous medium with partial heating and evaporation on the upper surface is performed in Chapter 2. The dependence of saturation temperature on the pressure was accounted for by using Clausius-Clapeyron equation. The model was first tested by reproducing the analytical results given in a previous research. A new kind of boundary condition was applied in order to reduce restrictions used in analytical solution and to study changes in velocity and temperature distributions before reaching the steady state evaporation. The flow in porous media was assumed to be at very low speed such that Darcy's Law is applicable. The effects of the new boundary on flow field and temperature distribution were studied.

1.3.2. Melting in Rectangular Enclosure

The Temperature Transforming Model (TTM) developed in 1990s is capable of solving convection controlled solid-liquid phase change problems. In this methodology, phase change is assumed to be taken place gradually through a range of temperatures and a mushy

zone that contains a mixture of solid and liquid phases exists between liquid and solid zones. The heat capacity within the range of phase change temperatures was assumed to be average of that of solid and liquid in the original TTM. In Chapter 3, a modified TTM is proposed to consider the dependence of heat capacity on the fractions of solid and liquid in the mushy zone. The Ramped Switch-Off Method (RSOM) is used for solid velocity correction scheme. The results are then compared with existing experimental and numerical results for a convection/diffusion melting problem in a rectangular cavity. Three working fluids with different heat capacity ratio were used to study the difference between the original TTM and the modified TTM. Those working fluids are octadecane whose heat capacity is very close to one, while the others are substances that have heat capacity further from one, such as 0.4437 for water and 1.2034 for acetic acid. In each case, the differences between each scheme were studied by tracking the movements of the melting fronts. Also, the total heat transfer was considered to study how the changes in mushy zone calculations would improve the numerical results.

1.3.3. Melting and Solidification in Porous Media

The complicated energy equation that usually governs the melting in porous media problem is simplified to a general equation used in TTM model. Conventionally, momentum equations is reduced to one pressure equation by assuming the Darcy's Law is valid since most flows in porous media have very small velocities. However, a modified Temperature-Transforming Model (TTM) that considers the dependence of heat capacity on the fractions of solid and liquid in the mushy zone is employed to solve melting in porous media. The velocity in the solid region is set to zero by the Ramped Switch-Off Method (RSOM). For

the liquid region, the momentum equations are modified and two drag forces (Darcy's term and Forchheimer's extension) are included to account for flows in porous media. This model also considers effects of natural convection through Boussinesq approximation. The results from these new governing equations will be compared to the results from the full form of momentum and energy equation. The new method will show improvement in computational time if its results can match up well with the conventional full-form equations.

1.3.4. Post-Processing by Infiltration

The parts fabricated by selective laser sintering of metal powder are usually not fully densified and have porous structure. Fully densified part can be obtained by infiltrating liquid metal into the porous structure and solidifying of the liquid metal. When the liquid metal is infiltrated into the subcooled porous structure, the liquid metal can be partially solidified. Remelting of the partially solidified metal can also take place and a second moving interface can be present. Infiltration, solidification and remelting of metal in subcooled laser sintered porous structure are analytically investigated in this paper. The governing equations are nondimensionlized and the problem is described using six dimensionless parameters. The temperature distributions in the remelting and uninfiltrated regions were obtained by an exact solution and an integral approximate solution, respectively. The effects of porosity, Stefan number, subcooling parameter and dimensionless infiltration pressure are investigated.

CHAPTER 2 FLOW IN POROUS MEDIA

In recent years, capillary pump loop (CPL) has been widely used in space application since its driving force is capillary force. A CPL system usually composes of an evaporator, a vapor line, a condenser, and a liquid line. Unlike conventional heat pipe, CPL does not have wick structure in condenser section. Consequently, a CPL system has lower pressure drop and can transport large heat loads over a longer distance. This makes the evaporator the most important section in a CPL system because its wick structure creates fluid circulation in additional of absorbing heat. The flow and heat transfer in the evaporator are complicated and influenced by (1) heat load [20], (2) characteristics of the porous media [21], (3) thermo-physical properties of working fluid and the porous media [22, 23], (4) liquid subcooling at the evaporator inlet [24], and (5) evaporator geometry. Due to the complexity of the evaporator, numerical model is required to predict the effects of these parameters on the evaporator performance.

Darcy's law is applicable when the particle Reynolds number, $Re_d = ud/\nu$, less than 2.3 [25]. There are several ways to implement the Darcy's law. Many researchers introduced stream function in order to eliminate the pressure gradient in the Darcy velocity for two-dimensional flow [26]. For three-dimensional flow, Stamp et al. [27] used vector potential in the pressure gradient elimination, while Kubitschek and Weidman [28] used eigenvalue equation to achieve the same goal. A few researchers combined Darcy's law with the continuity equation and came up with the Laplace equation of pressure instead of solving for each velocity component [29, 30].

After many general studies in flow in porous media, the studies of flow in the evaporator of CPL intensified since the year 2000. Mantelli and Bazzo [31] designed and investigated the performance of a solar absorber plates in both steady and transient states. In the same year, LaClair and Mudawar [32], investigated the transient nature of fluid flow and temperature distribution in the evaporator of a CPL prior to the initiation of boiling using Green's Function method to estimate temperature distribution. This method was shown to be best suited for CPL evaporator with fully-flooded startup because it determines the heat load at which nucleation is likely to occur in vapor grooves while maintaining subcool liquid core. Using Darcy's law for wick structure, Yan and Ochterbeck [24] studied the influences of heat load, liquid subcooing, and effective thermal conductivity of the wick structure on evaporator performance. They concluded that to reduce liquid core temperature either the applied heat flux and/or inlet liquid subcooling must be increased. Recently Pouzet [33] studied the dynamic response time of a CPL when applied with steps of various heat fluxes and found that CPL reacts badly to abrupt decreasing heat load.

Cao and Faghri [29] studied *steady-state* fluid flow and heat transfer in a porous structure with partial heating and evaporation on the upper surface, and obtained closed form solutions. During startup of the CPL or looped heat pipe, the fluid flow and heat transfer in the wick structure are not steady state and will have significant effect on the heat transfer performance. The present study considers a porous structure with liquid enters from the bottom and the top is partially heated and evaporation takes place on the rest of the upper surface, which is similar to that studied by Cao and Faghri [29]. The transient temperature distribution before and after evaporation occurring at the upper surface will be investigated. A more reasonable boundary condition will be applied in order to reduce restrictions used in analytical solution

and to study changes in pressure and temperature distributions before reaching the steady state evaporation. The effect of different boundary conditions on the steady-state flow and heat transfer, as well as transient flow and heat transfer will be investigated.

2.1. Physical Model

The schematic of the two-dimensional porous medium used in this study is shown in Fig. 2-1 Flow comes in at the bottom surface with a uniform velocity and goes out at the upper right surface. The left and right surfaces are insulated, while the upper left surface is a uniformly heated. The porous medium is made from sintered particles and fully flooded with saturated water before heat flux is applied. Before reaching the saturation temperature, it is assumed that there is no heat transfer at the outlet. After the temperature at the outlet reaches the saturation temperature corresponding to the pressure at the outlet, evaporation occurs and the temperature at right portion of the upper surface is fixed at the saturation temperature. The inlet flow has constant temperature, but the inlet velocity is guessed and later corrected based on global mass and heat balance.

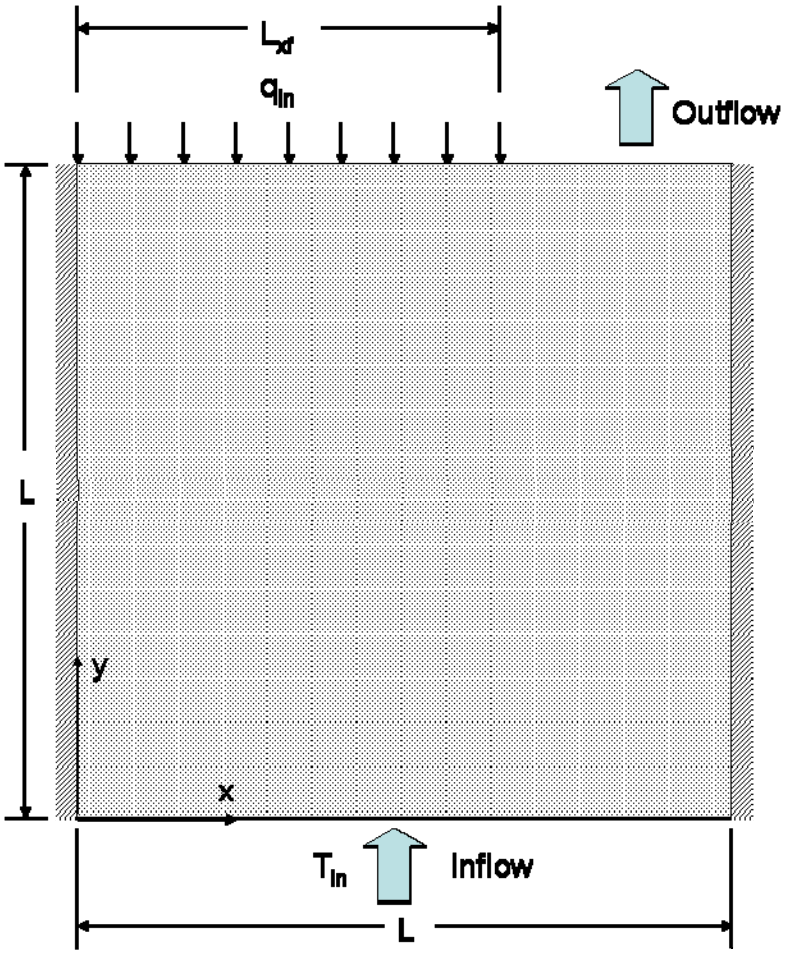

Fig. 2-1 Physical Model

These conditions allow fewer restrictions comparing to those of Cao and Faghri [29] and represent conditions closer to actual operation. The governing equations include continuity equation, Darcy's law, and energy equation.

Since flow in porous medium is very slow, the conventional momentum can be reduced to Darcy's law.

$$u = \frac{K}{\mu}\left(-\frac{\partial p}{\partial x}\right) \tag{2-1}$$

$$v = \frac{K}{\mu}\left(-\frac{\partial p}{\partial y}\right) \tag{2-2}$$

where u and v are velocity in x and y direction respectively, K is permeability of the porous medium, p is pressure, and μ is viscosity of water.

Assuming the liquid in the porous medium is incompressible, the continuity equation is

$$\frac{\partial u}{\partial x} + \frac{\partial v}{\partial y} = 0 \tag{2-3}$$

Substituting Eqs. (2-1) and (2-2) to Eq. (2-3), a Laplace equation of pressure is obtained.

$$\frac{\partial^2 p}{\partial x^2} + \frac{\partial^2 p}{\partial y^2} = 0 \tag{2-4}$$

The energy equation is

$$\frac{\partial \mathrm{T}^0}{\partial \mathrm{t}} + \mathrm{u}\frac{\partial \mathrm{T}^0}{\partial \mathrm{x}} + \mathrm{v}\frac{\partial \mathrm{T}^0}{\partial \mathrm{y}} = \alpha_{\mathrm{eff}}\left(\frac{\partial^2 \mathrm{T}^0}{\partial \mathrm{x}^2} + \frac{\partial^2 \mathrm{T}^0}{\partial \mathrm{y}^2}\right) \tag{2-5}$$

where T is temperature, t is time, and α_{eff} is effective diffusivity. The thermal diffusivity can be calculated from

$$\alpha_{\mathrm{eff}} = \frac{\mathrm{k}_{\mathrm{eff}}}{\rho \mathrm{c}_{\mathrm{p}}} \tag{2-6}$$

where k_{eff} is effective conductivity of the porous medium saturated with liquid, while ρ and c_p are density and specific heat of water [29].

To generalize the problem, several dimensionless parameters are introduced, while the temperature is reduced to a new parameter.

$$X = \frac{x}{H},\ Y = \frac{y}{H},\ P = \frac{H^2 p}{\rho \upsilon^2},\ U = \frac{uH}{\upsilon},\ V = \frac{vH}{\upsilon},\ \tau = \frac{\upsilon t}{H^2},\ T = T^0 - T_{in}^0 \qquad (2\text{-}7)$$

The governing equations are then transformed into

$$\frac{\partial^2 P}{\partial X^2} + \frac{\partial^2 P}{\partial Y^2} = 0 \qquad (2\text{-}8)$$

$$\frac{\partial \mathrm{T}}{\partial \tau} + \mathrm{U}\frac{\partial \mathrm{T}}{\partial \mathrm{X}} + \mathrm{V}\frac{\partial \mathrm{T}}{\partial \mathrm{Y}} = \frac{1}{\mathrm{Pr}}\left(\frac{\partial^2 \mathrm{T}}{\partial \mathrm{X}^2} + \frac{\partial^2 \mathrm{T}}{\partial \mathrm{Y}^2}\right) \qquad (2\text{-}9)$$

The boundary conditions of Eq. (2-8) are

$$\frac{\partial P}{\partial X} = 0, \quad X = 0 \ and\ 1 \qquad (2\text{-}10)$$

$$\frac{\partial P}{\partial Y} = -\frac{H^2}{K} V_{in}, \quad Y = 0 \qquad (2\text{-}11)$$

$$\frac{\partial P}{\partial Y} = \begin{cases} 0, & 0 < X < H_{xf} / H \\ -\dfrac{H^2}{K} V_{in}, & H_{xf} / H < X < 1 \end{cases} \qquad (2\text{-}12)$$

The initial and boundary conditions of Eq. (2-9) are

$$T = 0 \quad at \quad \tau = 0 \qquad (2\text{-}13)$$

$$\frac{\partial T}{\partial X} = 0 \quad at \quad X = 0 \ and\ 1 \qquad (2\text{-}14)$$

$$T = 0 \quad at \quad Y = 0 \; T^* = 0, \quad y^* = 0 \tag{2-15}$$

$$\frac{\partial T}{\partial Y} = \frac{H}{k} q_{in} \quad at \quad Y = 0 \; and \; 0 < X < H_{xf} / H \tag{2-16}$$

Cao and Faghri [29] prescribed the thermal boundary condition at the unheated portion of the upper surface based on the overall energy balance, i.e., the heat loss from the unheated portion is equal to latent heat carried away by the liquid exited from the unheated portion. While this treatment accurately described energy balance at steady-state, it cannot be applied to transient process because part of energy added from the heated portion of the upper surface is used to increase the temperature of the porous structure and consequently, the energy lost from the unheated portion of the upper surface is not equal to the heat added from the heated portion of the upper surface. In this paper the unheated portion of the upper surface is first treated as adiabatic. When the temperature at any point of the unheated upper surface reaches to the saturation temperature, the boundary condition is changed to constant temperature and evaporation is initiated. The new boundary condition at the unheated portion of the top surface is therefore

$$\frac{\partial T}{\partial Y} = 0 \quad at \quad Y = 1 \; and \; H_{xf} / H < X < 1, \quad \text{before evaporation} \left(T < T_{sat}^0 - T_{in}^0 \right) \tag{2-17}$$

$$T = T_{sat}^0 - T_{in}^0, \qquad \text{after evaporation} \tag{2-18}$$

The inlet velocity at the bottom of the computational domain, v_{in}, in Eq. (11) is computed from

$$V_{in} = \int_{H_{xf} / H}^{1} V \Big|_{Y=1} dX \tag{2-19}$$

because the liquid is incompressible.

2.2. Numerical Solution

The above problem is solved using the finite volume method [34]. Equation (2-9) is discretized using the power law scheme. The solution started with initial uniform temperature that is equal to the inlet temperature, uniform pressure. Once the temperature of the top surface reach to saturation temperature, evaporation takes place and fluid flow is initiated. After each iteration, v_{in} was calculated from Eq. (2-19) and T_{sat} was determined from the saturated pressure based on Clausius-Clapeyron equation.

$$T_{sat}^{0} = \frac{1}{\left[\frac{1}{T_{ref}^{0}} + \frac{R}{h_{fg}} \ln\left(\frac{p_{sat}}{p_{ref}}\right)\right]} \tag{2-20}$$

where R is universal gas constant, h_{fg} is latent heat of evaporation of water, T_{ref} is reference temperature (373 K) corresponding to the saturated pressure, and p_{ref} is reference pressure (101325 Pa) corresponding to the saturated temperature. The boundary condition is then changed following the new values of v_{in} and T^{0}_{sat}. The convergence criteria for each time step is that the conservation of mass flow rate in global level was satisfied and maximum differences of pressure and temperature to the previous iteration were less than 10^{-3} and 10^{-6} respectively. The steady state is reached when the maximum differences of pressure and temperature to the previous time step were less than 10^{-3} and 10^{-6} respectively. The conservation of heat rate in global level is also satisfied at the steady state.

2.3. Results and Discussions

The physical domain is a square, 0.75×0.75 mm^2, porous medium with permeability of 10^{-12} m^2. The effective thermal conductivity of the porous media saturated with liquid is assumed to be 4 W/m-K. A uniform grid with 38×38 nodes was used as the computational domain representing the physical model. The medium is insulated on left and right walls, ($L_{xf} < x < L$, L_{xf} = 0.5 mm), while it is partially heated at the upper wall ($0 < x < L_{xf}$). The time step size of 0.01 s was used with the power law to account for temperature changes in time.

In order to validate the code developed in this paper, computation for steady-state flow and heat transfer is performed using the same boundary condition as Ref. [29]. The results obtained by the present model and analytical solution of Ref. [29] are plotted in Fig. 2-2 for comparison.

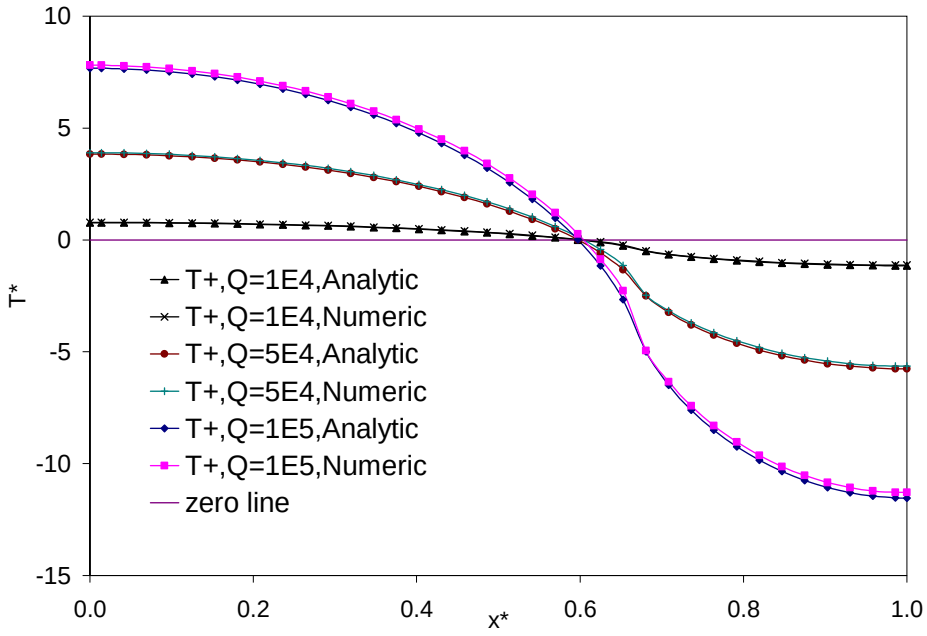

Fig. 2-2 Comparison of temperature obtained by analytical and numerical solutions at the top wall

The present model was able to provide very close values to the analytical values with the maximum difference of 7.98 % higher at location L_{xf} when applied with heat flux of 10^5 W/m^2. All numerical results gave higher values because in the analytical solution Cao and Faghri [29] used perturbation method and considered only the first two terms. Fig. 2-3 shows the velocity vector when applied with heat flux of 10^4 W/m^2. The temperature contour under the same condition is shown in Fig. 2-4. This velocity vector plot and the temperature distribution are very similar to those provided by Cao and Faghri [29]. Therefore, it is reasonable to conclude that the numerical model is able to recreate the analytical solution and will be a sufficient tool for simulating the present conditions.

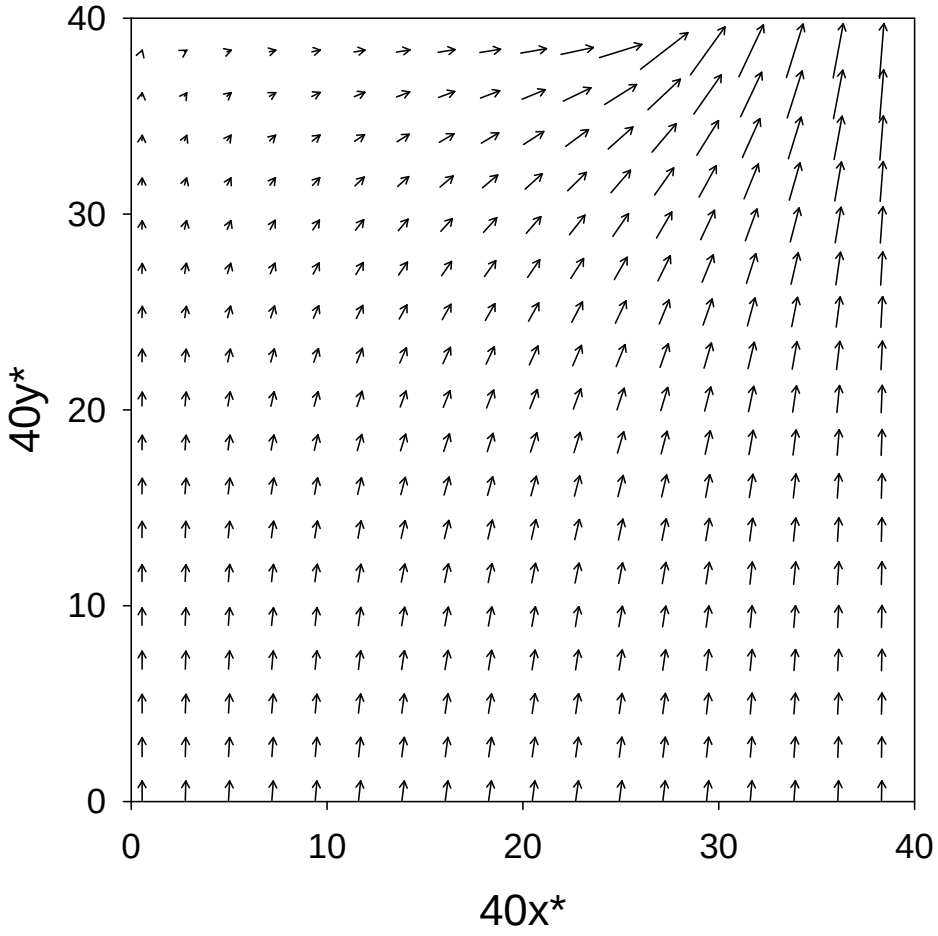

Fig. 2-3 Velocity vector plot when $q_{in} = 10^4$ W/m^2

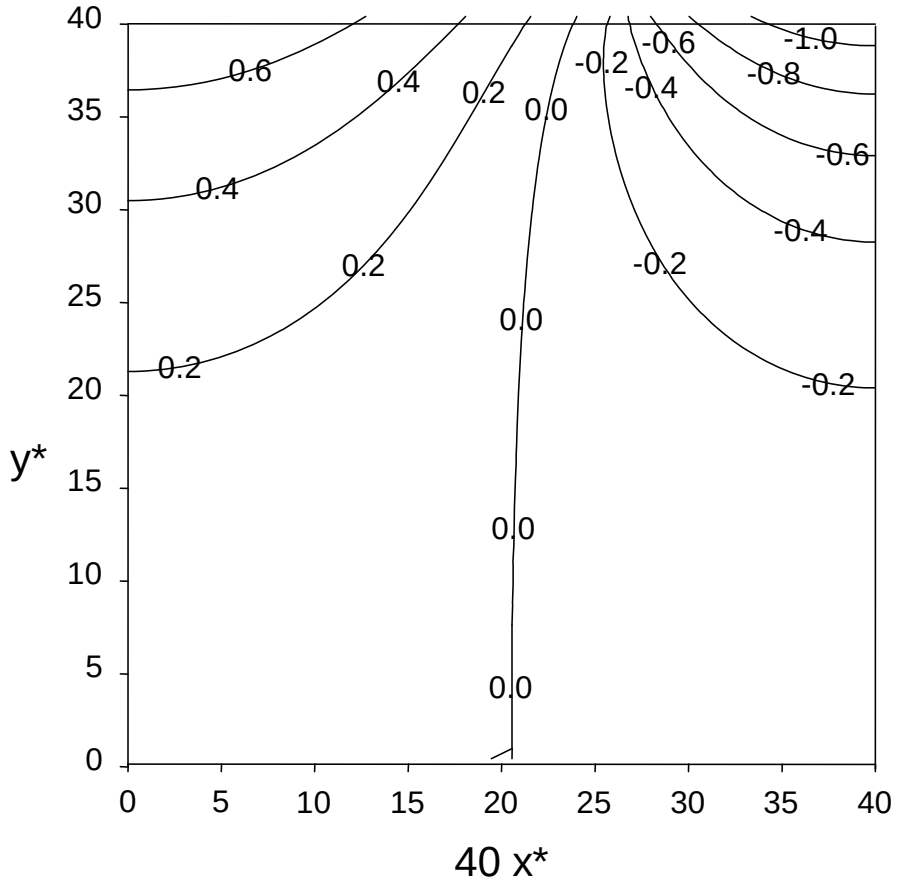

Fig. 2-4 Temperature contour plot when $q_{in} = 10^4$ W/m^2

The next step is to investigate fluid flow and temperature distribution when the present conditions were applied. Fig. 2-5 shows the comparison of temperature distribution at the upper surface when applied with different heat flux. All temperature distributions with saturated temperature boundary are higher than those of Cao and Faghri [24]. Also, the temperature on the heated surface is higher than saturated temperature, meaning the liquid near the heated surface must be superheated water in order to have evaporation at the outlet only.

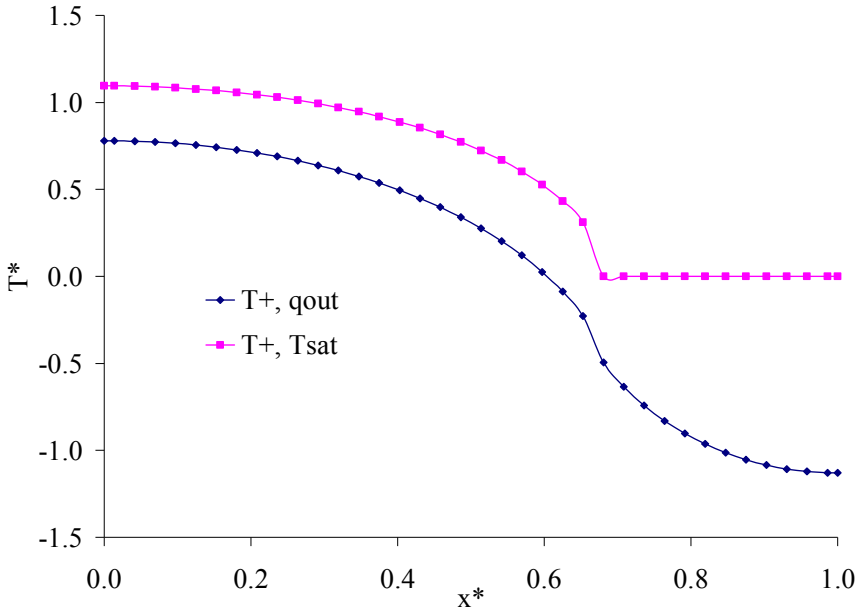

(a) $q_{in} = 10^4$ W/ m^2

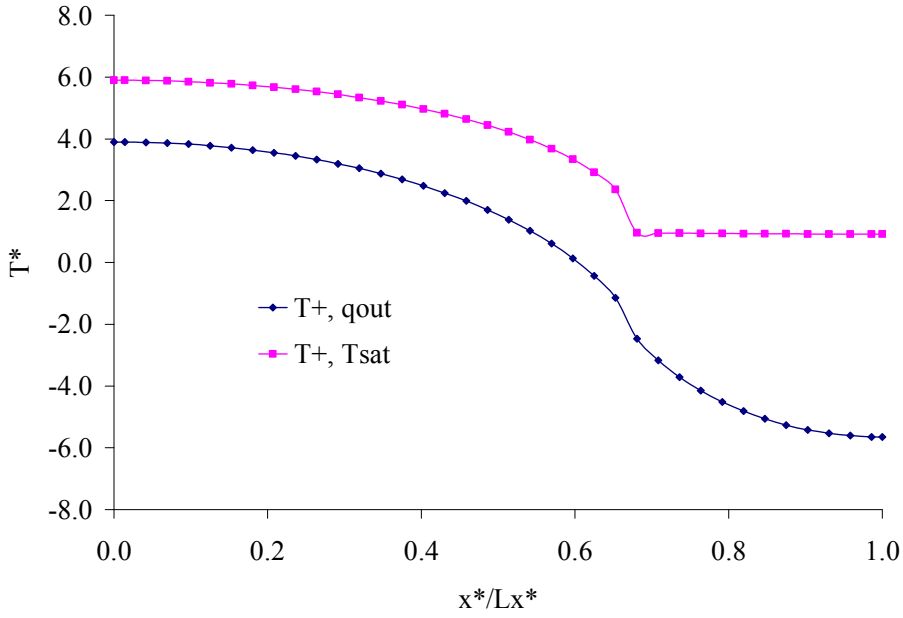

(b) $q_{in} = 5 \times 10^4$ W/ m^2

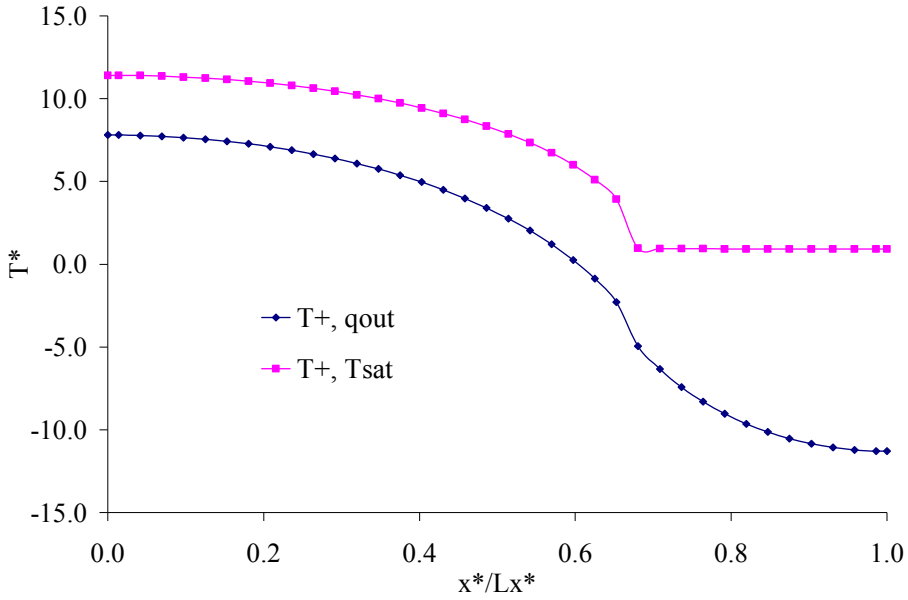

(c) $q_{in} = 10^5$ W/ m^2

Fig. 2-5 Comparison of temperature distribution on the top wall with different q_{in}

The velocity vector plots at 1 second and steady state (reached at t=37.2 s) in Fig. 2-6 shows that the velocity distribution is almost unchanged. The velocity vector plot is generally similar to that of Cao and Faghri [29] except the velocity profile at the outlet shows high velocity near the end of the heated surface. The temperature contour at different time is shown in Fig. 2-7.

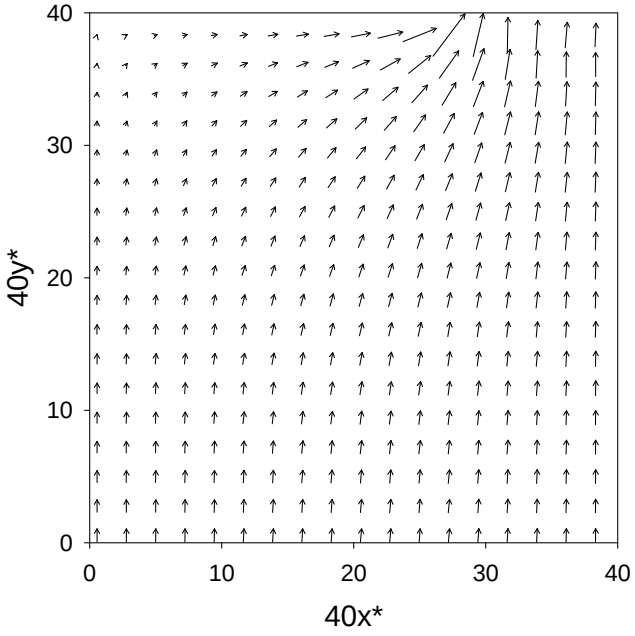

(a) 1 sec

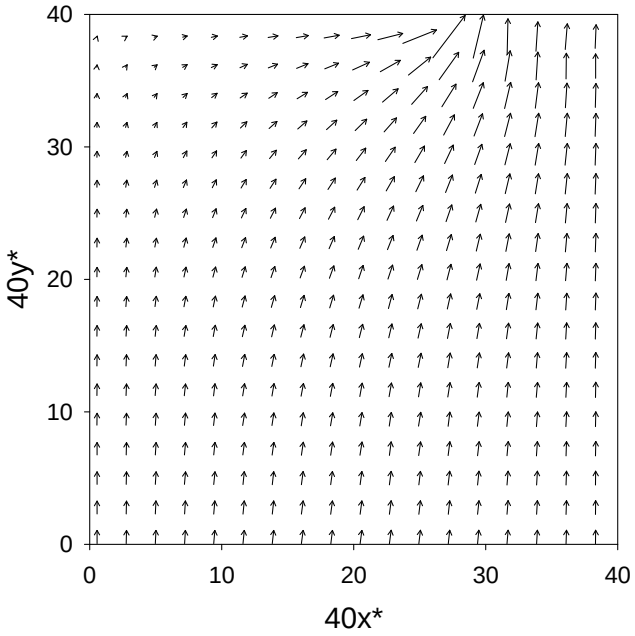

(b) Steady

Fig. 2-6 Velocity vector plots at different time when $T^*_{out}=T^*_{saT}$

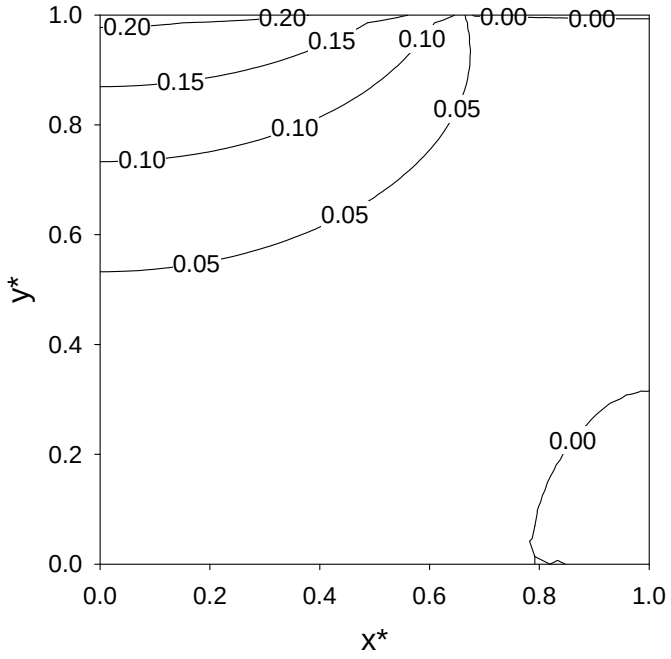

(a) 1 sec

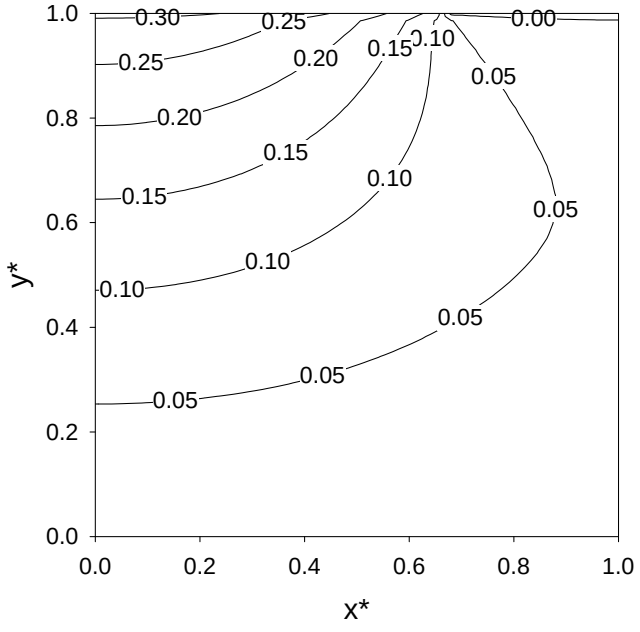

(b) 10 sec

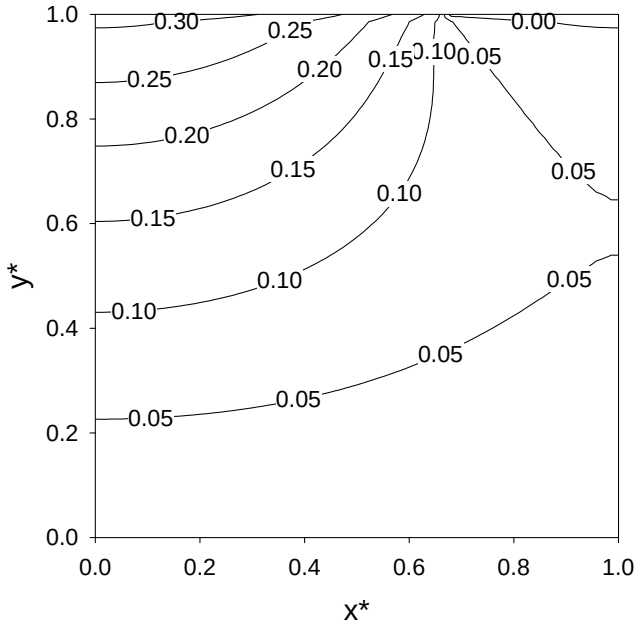

(c) 20 sec

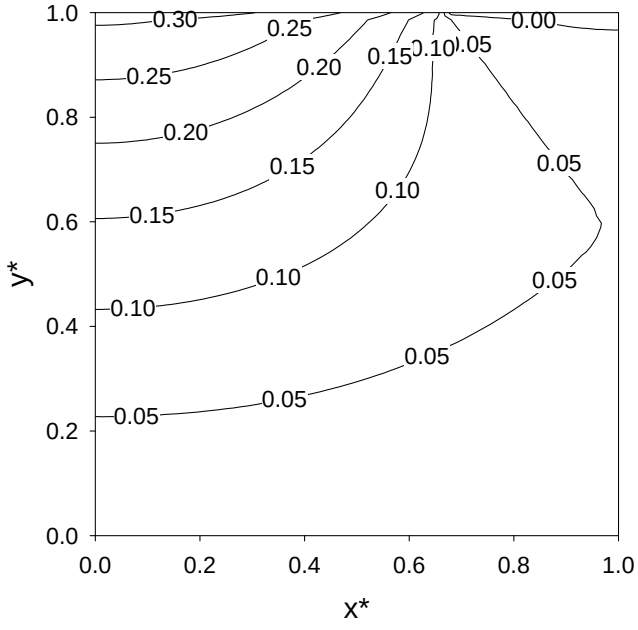

(d) 30 sec

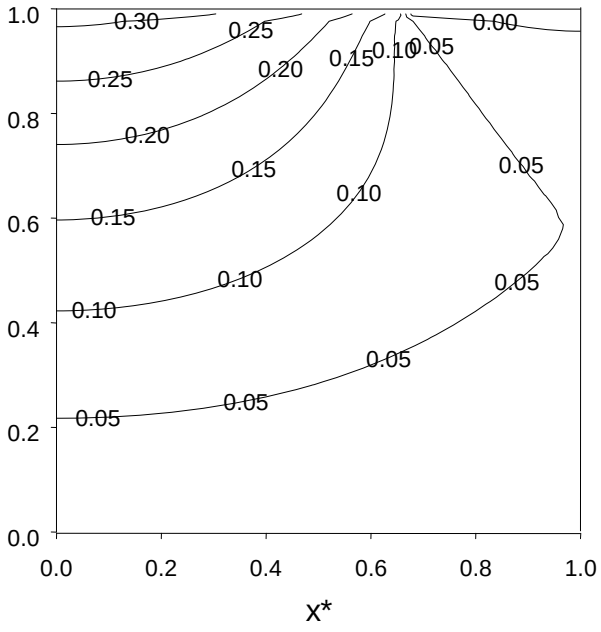

(e) steady

Fig. 2-7Temperature contour plots at different time when $T^*_{out} = T^*_{sat}$

Clearly, the trend and magnitude of temperature are totally different when comparing to Fig. 2-4. Generally, the new boundary conditions gives higher temperature and flatter temperature profile near the outlet because the temperature was set to saturated temperature corresponding to the pressure at the outlet. Again, the temperature gradient became larger as time passed. The highest gradient was located near the heated surface and under the outlet. The upper surface temperature at different time is shown in Fig. 2-8. It can be seen that the temperature increased rapidly for the first few seconds, and then the increment gradually slowed down as the time passed.

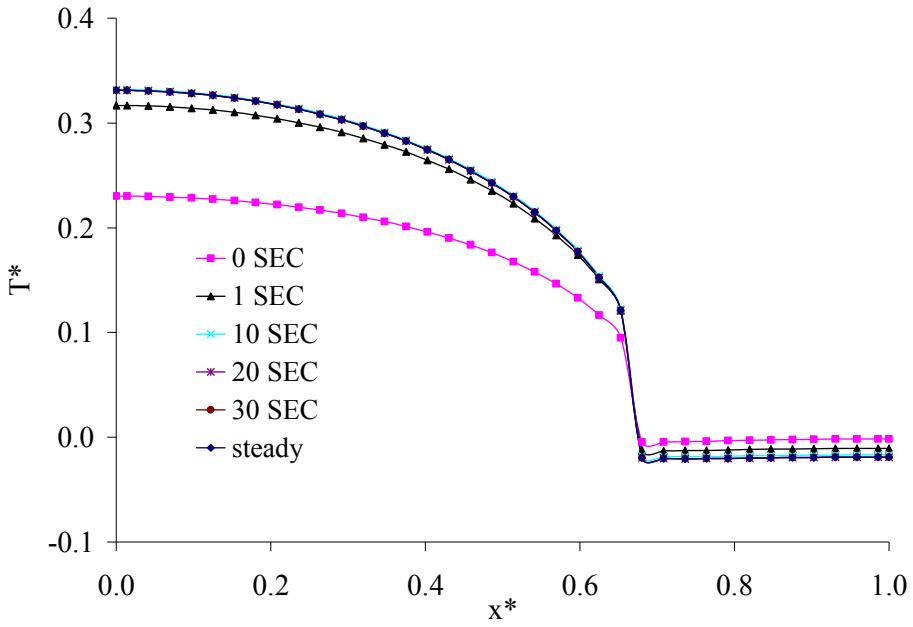

Fig. 2-8Temperature distributions at different time when $T^*_{out} = T^*_{sat}$

2.4. Conclusions

Transient fluid flow and heat transfer in a porous medium with partial heating and evaporation on the upper surface was investigated. The numerical model was able to reproduce steady-state analytical solution given by Cao and Faghri [29]. The history of velocity vector and temperature contour from the starting of the process until it reached steady state under new boundary condition is investigated. The results showed that as time passes the magnitude of velocity increases until the process reached steady state. The maximum velocity occurred near the end of heated plate. The temperature near the heated surface was higher than saturation temperature representing superheated liquid.

CHAPTER 3 MELTING IN RECTANGULAR ENCLOSURE

The temperature transforming model (TTM) that was proposed by Cao and Faghri [16] is based on the following assumptions: (i) solid-liquid phase change occurred within a range of temperatures; (ii) the fluid flow in the liquid phase is an incompressible laminar flow with no viscous dissipation; (iii) the change of thermal physical properties in the mushy region is linear; and (iv) the thermal physical properties are constants in each phase but may differ among solid and liquid phases, while density is constant for all phases. In this methodology, phase change is assumed to be taken place gradually through a range of temperatures and a mushy zone that contains a mixture of solid and liquid phases exists between liquid and solid zones. The heat capacity within the range of phase change temperatures was assumed to be average of that of solid and liquid in the original TTM. While this treatment could provide accurate results for the cases that heat capacity ratio of the PCM is close to one ($\rho_s c_{ps} \approx \rho_\ell c_{p\ell}$), an alternative method that can consider the dependence of heat capacity on the fractions of solid and liquid in the mushy zone is necessary for the case that the heat capacity ratio is not close to one. A modified TTM that consider heat capacity in the mushy zone as a linear function of solid and liquid fractions will be developed.

In this chapter, a modified TTM is proposed to consider the dependence of heat capacity on the fractions of solid and liquid in the mushy zone. The Ramped Switch-Off Method (RSOM) is used for solid velocity correction scheme. The results are then

compared with existing experimental and numerical results for a convection/diffusion melting problem in a rectangular cavity. The results show that TTM with the new assumption are closer to experimental results with octadecane as PCM even though its heat capacity ratio is very close to one. The modified TTM is then tested on substances that have heat capacity further from one, such as 0.4437 for water and 1.2034 for acetic acid. The results show that the original TTM under predicts the velocity of the solid-liquid interface when the heat capacity ratio is less than one and over predicts the velocity when the ratio is higher than one.

3.1. Physical Model

Melting inside a rectangular enclosure as shown in Fig. 3-1 will be studied in this chapter. The top and bottom walls are insulated, while the left and right walls are kept at high constant temperature T_h^0 and low constant temperature T_c^0, respectively. The initial temperatures were set to T_c^0 in all cases.

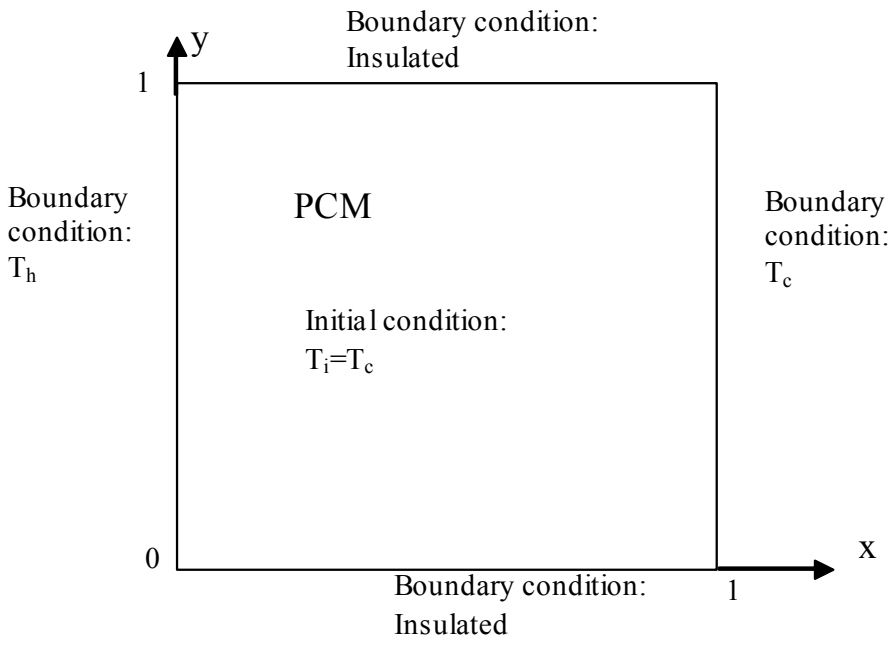

Fig. 3-1 Physical Model

3.2. Governing Equations

In TTM, conventional continuity and momentum equations for fluid flow problems are applicable, while the energy equation is transformed into a nonlinear equation similar to the method used in temperature-based equivalent heat capacity methods. The governing equations using the original TTM expressed in a two-dimensional Cartesian coordinate system are as follows (*y* axis is the vertical axis):

Continuity equation

$$\frac{\partial u}{\partial x}+\frac{\partial v}{\partial y}=0$$

(3-1)

Momentum equations in x and y directions

$$\frac{\partial(\rho u)}{\partial t}+\frac{\partial(\rho uu)}{\partial x}+\frac{\partial(\rho vu)}{\partial y}=-\frac{\partial p}{\partial x}+\frac{\partial}{\partial x}\left(\mu\frac{\partial u}{\partial x}\right)+\frac{\partial}{\partial y}\left(\mu\frac{\partial u}{\partial y}\right)$$

(3-2)

$$\frac{\partial(\rho v)}{\partial t}+\frac{\partial(\rho uv)}{\partial x}+\frac{\partial(\rho vv)}{\partial y}=-\frac{\partial p}{\partial y}+\rho g+\frac{\partial}{\partial x}\left(\mu\frac{\partial v}{\partial x}\right)+\frac{\partial}{\partial y}\left(\mu\frac{\partial v}{\partial y}\right)$$

(3-3)

Energy equation

$$\frac{\partial\left(C^0T^*\right)}{\partial t}+\frac{\partial\left(C^0uT^*\right)}{\partial x}+\frac{\partial\left(C^0vT^*\right)}{\partial y}=\frac{\partial}{\partial x}\left(k\frac{\partial T^*}{\partial x}\right)+\frac{\partial}{\partial y}\left(k\frac{\partial T^*}{\partial y}\right)-\left[\frac{\partial\left(S^0\right)}{\partial t}+\frac{\partial\left(S^0u\right)}{\partial x}+\frac{\partial\left(S^0v\right)}{\partial y}\right]$$

(3-4)

where $T^*=T^0-T_m^0$ is scaled temperature and coefficients C^0 and S^0 in equation (3-4) are

$$C^0(T)=\begin{cases}(\rho c)_s, & T<T_m^0-\Delta T^0\\ (\rho c)_m+\dfrac{\rho h_{sl}}{2\Delta T^0}, & T_m^0-\Delta T^0\le T\le T_m^0+\Delta T^0\\ (\rho c)_l, & T^*>T_m^0+\Delta T^0\end{cases} \tag{3-5}$$

$$S^0(T)=\begin{cases}(\rho c)_s\Delta T^0, & T<T_m^0-\Delta T^0\\ (\rho c)_m\Delta T^0+\dfrac{\rho h_{sl}}{2}, & T_m^0-\Delta T^0\le T^*\le T_m^0+\Delta T^0\\ (\rho c)_l\Delta T^0+\rho h_{sl}, & T>T_m^0+\Delta T^0\end{cases} \tag{3-6}$$

and the thermal conductivity is

$$k(T)=\begin{cases} k_s, & T<T_m^0-\Delta T^0 \\ k_s+(k_l-k_s)\dfrac{T^*+\Delta T^0}{2\Delta T^0}, & T_m^0-\Delta T^0\le T\le T_m^0+\Delta T^0 \\ k_l, & T>T_m^0+\Delta T^0 \end{cases} \tag{3-7}$$

where $T<T_m^0-\Delta T^0$ corresponds to the solid phase, $T_m^0-\Delta T^0\le T\le T_m^0+\Delta T^0$ to the mushy zone, and $T>T_m^0+\Delta T^0$ to the liquid phase. The heat capacity in the mushy zone was assumed to be the average of those of solid and liquid phases.

$$(\rho c)_m=\frac{1}{2}\left[(\rho c)_s+(\rho c)_l\right] \tag{3-8}$$

which will not be a suitable assumption when the heat capacity ratio of the substance is not close to 1. To improve the TTM, it is proposed that the heat capacity is a function the liquid fraction

$$(\rho c)_m=(1-\varphi_l)(\rho c)_s+\varphi_l(\rho c)_l \tag{3-9}$$

where φ_l is liquid fractions in the mushy zone and the solid fraction is $1-\varphi_l$. The liquid fraction is related to the temperature of the mushy zone by

$$\varphi_l=\frac{T-T_m^0+\Delta T^0}{2\Delta T^0} \tag{3-10}$$

The coefficients C^0, S^0 for the energy equation of the modified TTM becomes

$$C^0\left(T^0\right)=\begin{cases} \left(\rho c\right)_s, & T^0-T_m^0<-\Delta T^0 \\ \dfrac{\left(\rho c\right)_l+\left(\rho c\right)_s}{2}+\dfrac{\rho h_{sl}}{2\Delta T^0}+\dfrac{\left(\rho c\right)_l-\left(\rho c\right)_s}{4}(T^0-T_m^0), & -\Delta T^0\le T^0-T_m^0\le\Delta T^0 \\ \left(\rho c\right)_l, & T^0-T_m^0>\Delta T^0 \end{cases}$$

(3-11)

$$S^0\left(T^0\right)=\begin{cases}\left(\rho c\right)_s \Delta T^0, & T^0-T_m^0<-\Delta T^0 \\ \dfrac{\left(\rho c\right)_l+3\left(\rho c\right)_s}{4}\Delta T^0+\dfrac{\rho h_{sl}}{2}, & -\Delta T^0\le T^0-T_m^0\le\Delta T^0 \\ \left(\rho c\right)_s \Delta T^0+\rho h_{sl}, & T^0-T_m^0>\Delta T^0\end{cases} \tag{3-12}$$

and the thermal conductivity is

$$k\left(T^0\right)=\begin{cases}k_s, & T^0-T_m^0<-\Delta T^0 \\ \dfrac{k_l+k_s}{2}+\dfrac{\left(k_l-k_s\right)}{2\Delta T^0}T^*, & -\Delta T^0\le T^0-T_m^0\le\Delta T^0 \\ k_l, & T^0-T_m^0>\Delta T^0\end{cases} \tag{3-13}$$

Introducing these following non-dimensional variables:

$$\mathrm{X}=\frac{\mathrm{x}}{\mathrm{H}},\ \mathrm{Y}=\frac{\mathrm{y}}{\mathrm{H}},\ \ \mathrm{U}=\mathrm{u}\frac{\mathrm{H}}{\nu_l},\ \mathrm{V}=\mathrm{v}\frac{\mathrm{H}}{\nu_l},\ \tau=\frac{\nu_l \mathrm{t}}{\mathrm{H}^2},\ T=\frac{T^0-T_m^0}{T_h^0-T_m^0},$$

$$\Delta T=\frac{\Delta T^0}{T_h^0-T_m^0},\ \mathrm{C}=\frac{\mathrm{C}^0}{(\rho \mathrm{c})_l},\ S=\frac{S^0}{\left(\rho c\right)_l\left(T_h^0-T_m^0\right)},\ \mathrm{K}=\frac{\mathrm{k}}{\mathrm{k}_l},$$

$$Ste=\frac{c_l\left(T_h^0-T_m^0\right)}{h_{sl}},\ C_{sl}=\frac{\left(\rho c\right)_s}{\left(\rho c\right)_l},\ K_{sl}=\frac{k_s}{k_l},\ P=\frac{H^2}{\rho\nu_l^2}\left(p+\rho g\right) \tag{3-14}$$

The governing equations can be non-dimensionalized as:

$$\frac{\partial \mathrm{U}}{\partial \mathrm{X}}+\frac{\partial \mathrm{V}}{\partial \mathrm{Y}}=0 \tag{3-15}$$

$$\frac{\partial \mathrm{U}}{\partial \tau}+\frac{\partial(\mathrm{U}^2)}{\partial \mathrm{X}}+\frac{\partial(\mathrm{UV})}{\partial \mathrm{Y}}=-\frac{\partial \mathrm{P}}{\partial \mathrm{X}}+\frac{\partial}{\partial \mathrm{X}}\left(\frac{\mathrm{Pr}}{\mathrm{Pr}_l}\frac{\partial \mathrm{U}}{\partial \mathrm{X}}\right)+\frac{\partial}{\partial \mathrm{Y}}\left(\frac{\mathrm{Pr}}{\mathrm{Pr}_l}\frac{\partial \mathrm{U}}{\partial \mathrm{Y}}\right) \tag{3-16}$$

$$\frac{\partial \mathrm{V}}{\partial \tau}+\frac{\partial(\mathrm{UV})}{\partial \mathrm{X}}+\frac{\partial(\mathrm{V}^2)}{\partial \mathrm{Y}}=-\frac{\partial \mathrm{P}}{\partial \mathrm{Y}}+\frac{\mathrm{Ra}}{\mathrm{Pr}_l}\mathrm{T}+\frac{\partial}{\partial \mathrm{X}}\left(\frac{\mathrm{Pr}}{\mathrm{Pr}_l}\frac{\partial \mathrm{V}}{\partial \mathrm{X}}\right)+\frac{\partial}{\partial \mathrm{Y}}\left(\frac{\mathrm{Pr}}{\mathrm{Pr}_l}\frac{\partial \mathrm{V}}{\partial \mathrm{Y}}\right) \tag{3-17}$$

$$\frac{\partial(\mathrm{CT})}{\partial\tau}+\frac{\partial(\mathrm{UCT})}{\partial \mathrm{X}}+\frac{\partial(\mathrm{VCT})}{\partial \mathrm{Y}}=\frac{\partial}{\partial \mathrm{X}}(\frac{\mathrm{K}}{\mathrm{Pr}_l}\frac{\partial \mathrm{T}}{\partial \mathrm{X}})+\frac{\partial}{\partial \mathrm{Y}}(\frac{\mathrm{K}}{\mathrm{Pr}_l}\frac{\partial \mathrm{T}}{\partial \mathrm{Y}})-[\frac{\partial \mathrm{S}}{\partial\tau}+\frac{\partial(\mathrm{US})}{\partial \mathrm{X}}+\frac{\partial(\mathrm{VS})}{\partial \mathrm{Y}}]$$

(3-18)

where

$$C=\begin{cases} C_{sl}, & T<-\Delta T \\ \dfrac{1+C_{sl}}{2}+\dfrac{1}{2Ste\Delta T}+\dfrac{1\text{-}C_{sl}}{4\Delta T}T, & -\Delta T\le T\le \Delta T \\ 1, & T>\Delta T \end{cases} \tag{3-19}$$

$$S=\begin{cases} C_{sl}\Delta T, & T<-\Delta T \\ \dfrac{1+3C_{sl}}{4}\Delta T+\dfrac{1}{2Ste}, & -\Delta T\le T\le \Delta T \\ C_{sl}\Delta T+\dfrac{1}{Ste}, & T>\Delta T \end{cases} \tag{3-20}$$

and the thermal conductivity is

$$K=\begin{cases} K_{sl}, & T<-\Delta T \\ \dfrac{1+K_{sl}}{2}+\dfrac{1-K_{sl}}{2\Delta T}T, & -\Delta T\le T\le \Delta T \\ 1, & T>\Delta T \end{cases} \tag{3-21}$$

It should be noted that the body force in equation (3-17) will be changed to $\mathrm{Ra}\left|\mathrm{T}-\mathrm{T}_{\max}\right|^{\mathrm{q}}/\mathrm{Pr}$ when the working fluid is water, where $\mathrm{T}_{\max}$ is the temperature at which water has maximum density (4.029325 °C) and q is 1.894816.

3.3. Numerical Solution Procedure

3.3.1. Discretization of governing equations

The two-dimensional governing equations are discretized by applying a finite volume method [25], in which conservation laws are applied over finite-sized control volumes around grid points and the governing equations are then integrated over the control volume. Staggered grid arrangement is used in discretization of the computational domain in momentum equations. A power law scheme is used to discretize convection/diffusion terms in momentum and energy equations. The main algebraic equation resulting from this control volume approach is in the form of

$$a_P \phi_P = \sum a_{nb} \phi_{nb} + b \tag{3-22}$$

where ϕ_P represents the value of variable ϕ (U, V or T) at the grid point P, ϕ_{nb} are the values of the variable at P's neighbor grid points, and a_P, a_{nb} and b are corresponding coefficients and terms derived from original governing equations. The numerical simulation is accomplished by using SIMPLE algorithm [25]. The velocity-correction equations for corrected U and V in the algorithm are

$$\mathrm{U}_e = \mathrm{U}_e^* + d_e(\mathrm{P}'_\mathrm{P} - \mathrm{P}'_\mathrm{E}) \tag{3-23}$$

$$\mathrm{V}_n = \mathrm{V}_n^* + d_n(\mathrm{P}'_\mathrm{P} - \mathrm{P}'_\mathrm{N}) \tag{3-24}$$

where according to the staggered grid arrangement e and n respectively represent the control-volume faces between grid P and its east neighbor E and grid P and its north neighbor N. The source term S in governing equations is linearized into the form

$$S = S_C + S_P \phi_P \tag{3-25}$$

in a control volume, and by discretization S_P and S_C are then respectively included in a_P and b in equation (3-22).

3.3.2. Ramped Switch-off Method (RSOM)

To avoid discontinuity of the values of U and V at the phase-change fronts, Ma and Zhang [27] develop a Ramped SOM (RSOM), in which the whole domain is divided into three regions: solid region, mushy region and liquid region. In the solid region ($\mathrm{T} \le -\Delta\mathrm{T}$), the value of a_P is set as very large positive number, 10^{30}, while d_e and d_n are set as very small positive numbers, 10^{-30}. In the mushy region where $-\Delta\mathrm{T} \le \mathrm{T} \le \Delta\mathrm{T}$, the adjustments for a_P, d_e and d_n satisfy the following linear relations:

$$a_P = a_{Pi} + \frac{\mathrm{T} - \Delta\mathrm{T}}{2\Delta\mathrm{T}}(a_{Pi} - 10^{30}) \tag{3-26}$$

$$d_e = d_{ei} / a_P, \quad d_n = d_{ni} / a_P \tag{3-27}$$

where a_{Pi}, d_{ei} and d_{ni} are the values of these coefficients in the mushy region originally computed by SIMPLE algorithm. For the liquid area ($T \ge \Delta T$), a_P, d_e and d_n are just directly computed by the SIMPLE algorithm.

3.4. Results and discussions

The modified Temperature Transforming Model (TTM) was validated by comparing its results to an experimental result and other numerical results. Figure 3-2 shows the positions of melting fronts obtained by the modified TTM compared with Okada's

experimental results [35], Cao and Faghri's TTM simulation [16], and Ma and Zhang's numerical results [19] at a dimensionless time of $\tau = 39.9$. The PCM used in those researches were octadecane which has solid-liquid heat capacity ratio (C_{sl}) of 0.986, thermal conductivity ratio (K_{sl}) of 2.355, and Prandtl number of 56.2. All researches started with a temperature very close to melting point, in other word the subcooling parameter (Sc) was equal to 0.01 and Stefan number (Ste) was 0.045 and Raleigh number (Ra) was 10^6. Following the suggestion by Ma and Zhang [19], the grid number of 40×40 and time step of 0.1 was used for this step. Even though the heat capacity ratio of octadecane is very close to 1, the modified TTM results show a slight improvement by moving closer toward experimental results in Ref. [35].

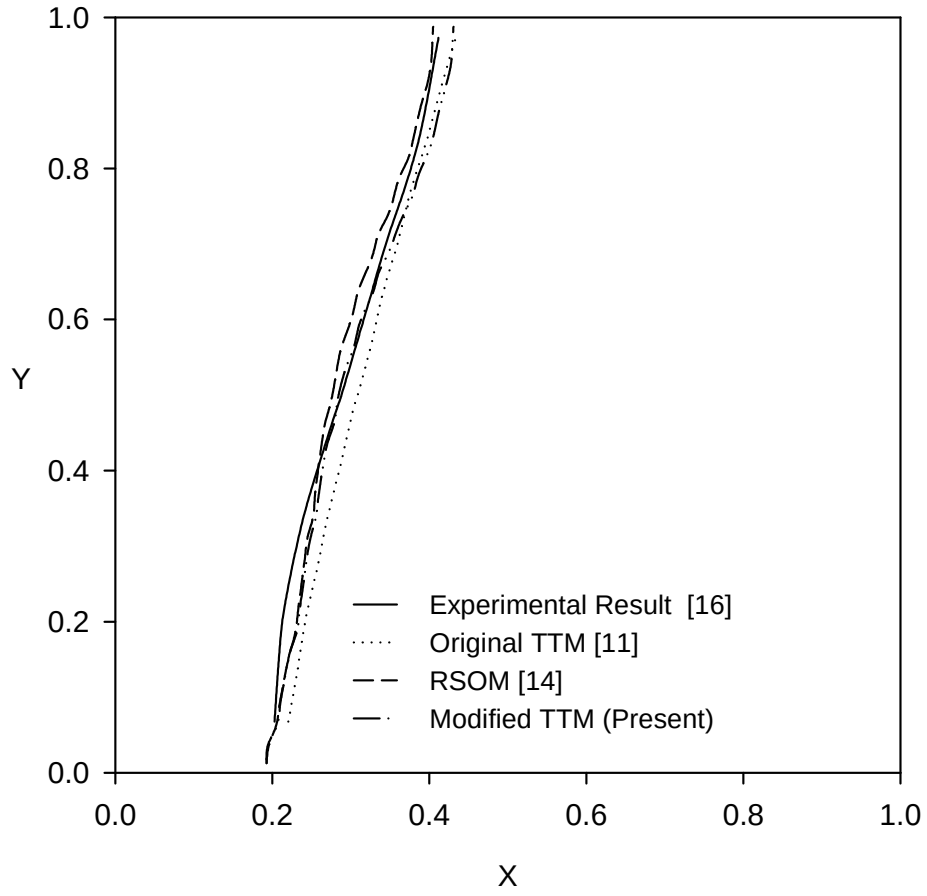

Fig. 3-2 Comparison of the locations of the melting fronts at $\tau = 39.9$ (grid size: 40×40, time step $\Delta\tau = 0.5$)

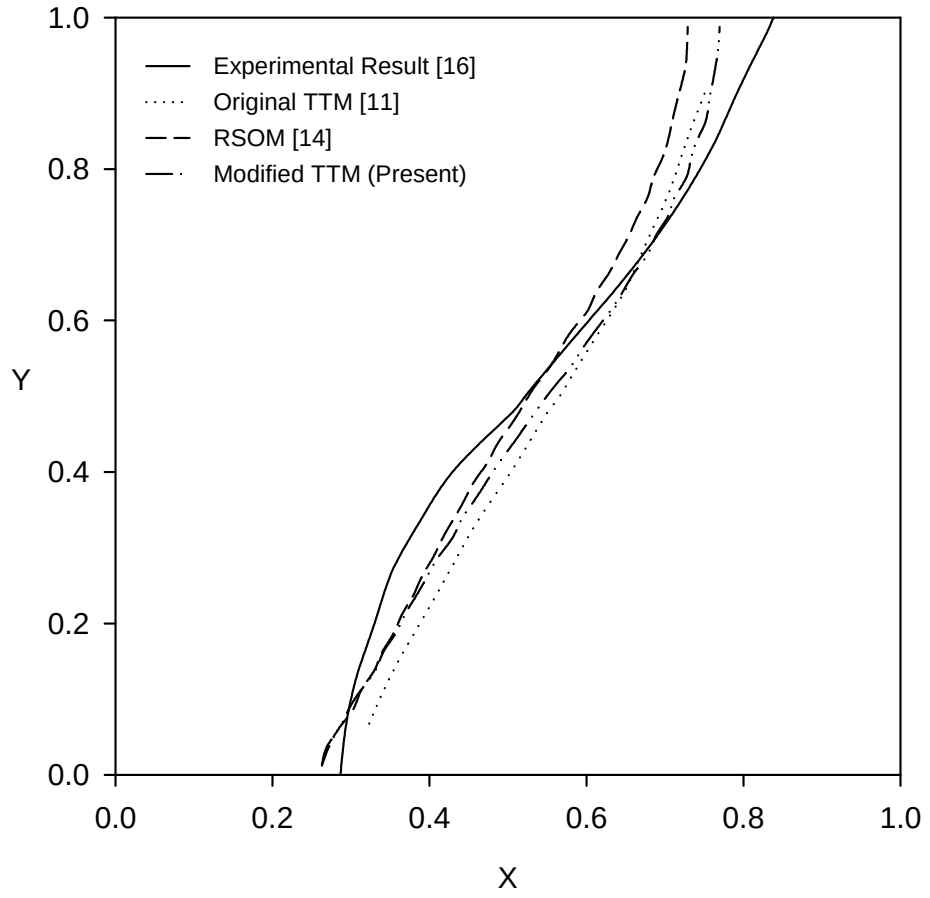

Fig. 3-3 Comparison of the locations of the melting fronts at $\tau = 78.68$ (grid size: 40×40, time step $\Delta\tau = 0.1$)

Fig. 3-3 shows those positions at τ = 78.6. As time progresses, the modified TTM gives results closer to the experimental result. The velocity vector contour for τ = 78.6 is given in Fig. 3-4. It can be seen that the liquid flows upward near the heated wall and flows downward near the solid-liquid interface, which is consistent with the typical natural convection problem with higher temperature on the left wall. The modified TTM

with RSOM can provide accurate prediction for phase-change problems with natural convection.

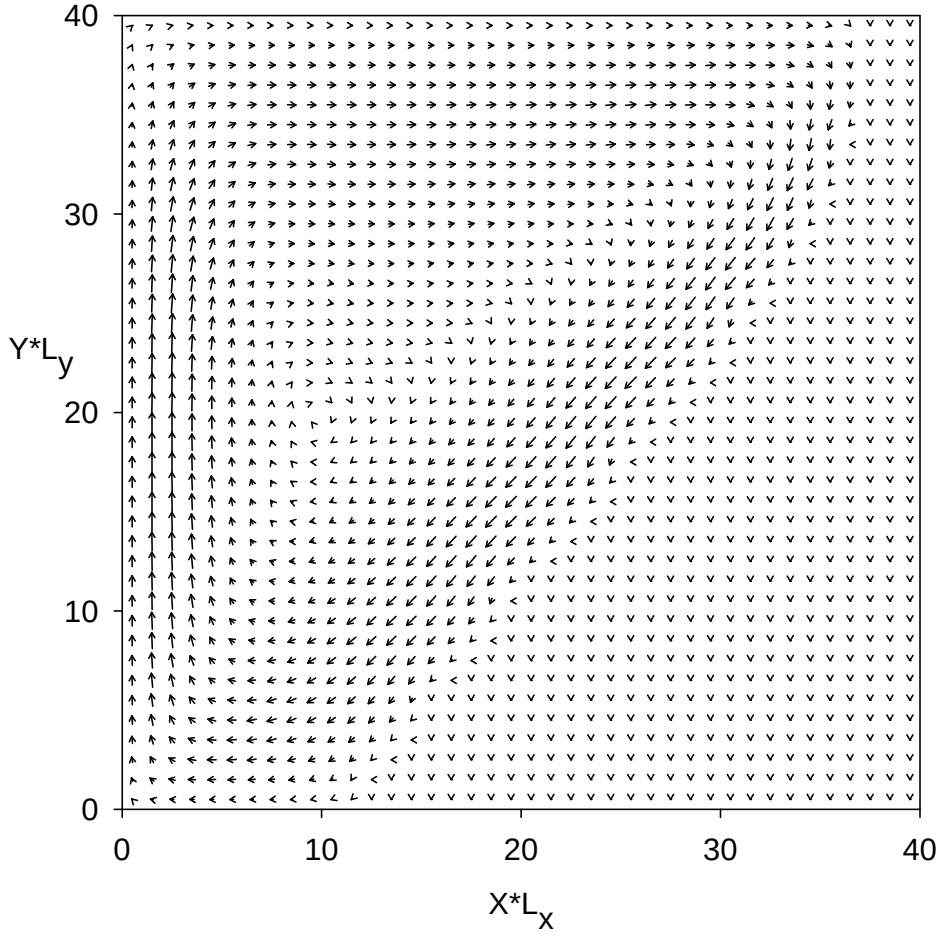

Fig. 3-4 Velocity vector when $\tau = 78.68$ for modified TTM (grid size: 40×40, time step $\Delta\tau = 0.1$)

The modified TTM with RSOM is further tested with substances that has heat capacity ratio far from one. The substance of choice is water which has C_{sl} of 0.477, K_{sl} of 3.793, and Prandtl number of 11.54. The subcooling, Sc, is 0.25 and the Stefan number,

Ste, is 0.101. After extensive grid dependent study, 50×50 grid and time step size of 10^{-4} were chosen as the optimum grid and time step for modified TTM to be applied with water. Fig. 3-5 shows the velocity vectors at different heating temperatures. It can be seen that the modified TTM can capture the unique flow pattern of water: water has one circulation when temperature is less than 4.029325 °C (the temperature with highest density) and it has two circulations when temperature is higher than 4.029325 °C.

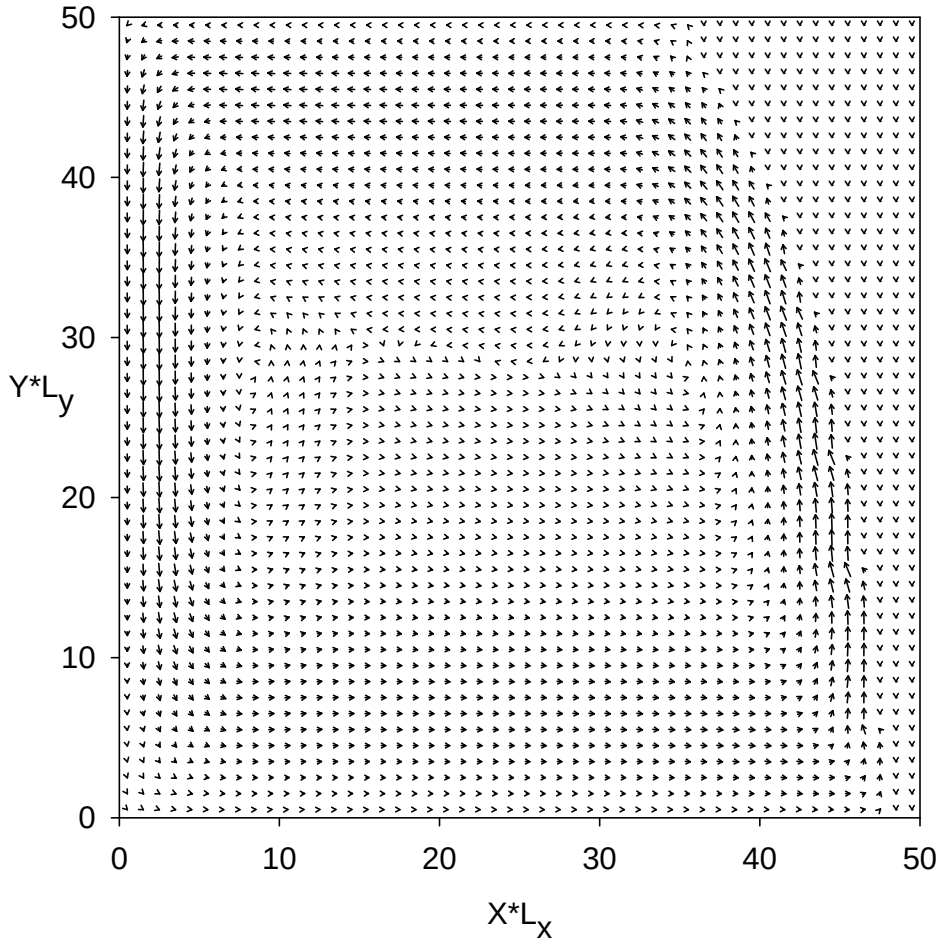

(a) $T_h = T_{max} = 4.029325$ °C

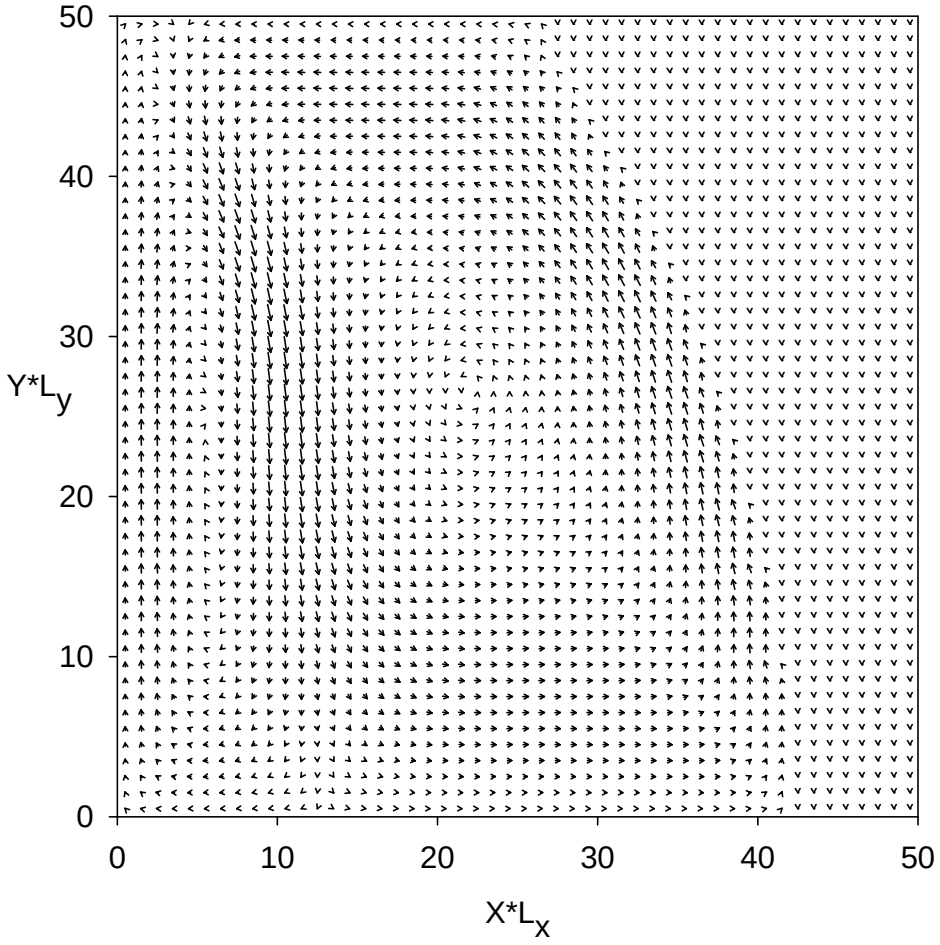

(b) T_h =8 °C > T_{max}

Fig. 3-5 Velocity vector plot shows the unique ability of water flow in different temperature on the right wall

Fig. 3-6 shows the comparison of total volume fraction V_L, total heat on the right wall Q_H, and total heat on the left wall Q_L between modified and original TTM results to those of Ho and Chu [36]. Both modified and original TTM under predict total heat

transfer inside the domain when comparing to [36]. However, modified TTM still gives results closer to [36] than original TTM.

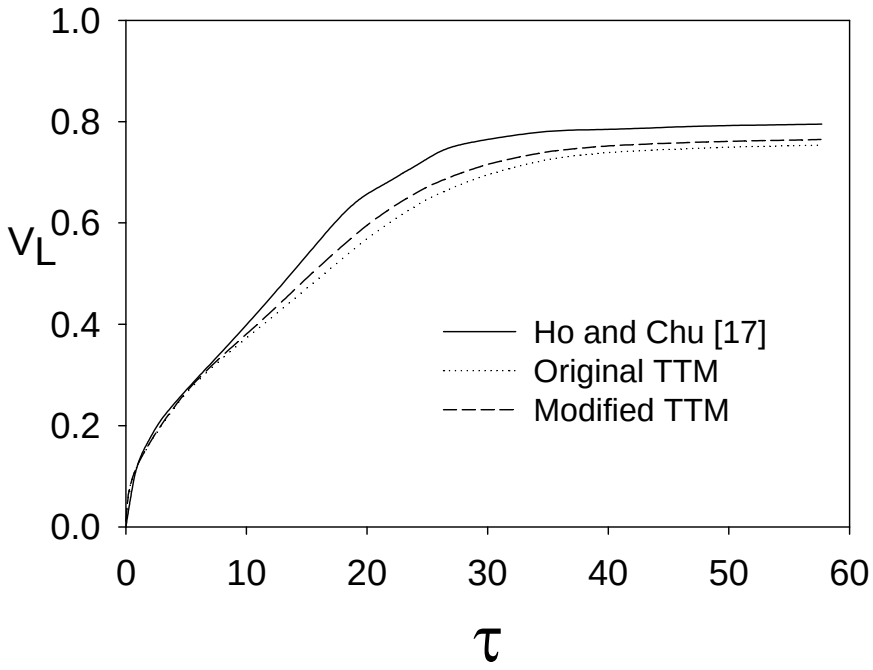

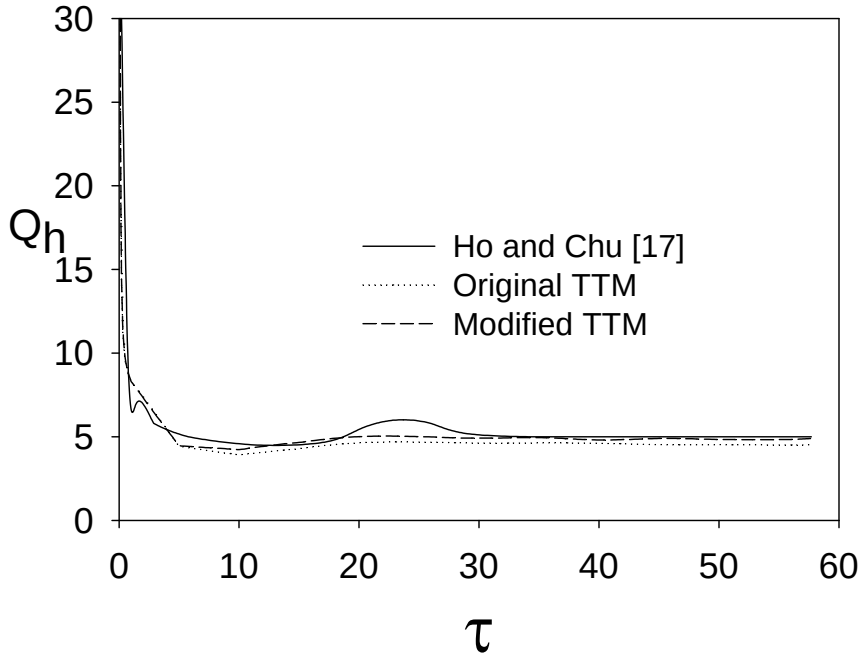

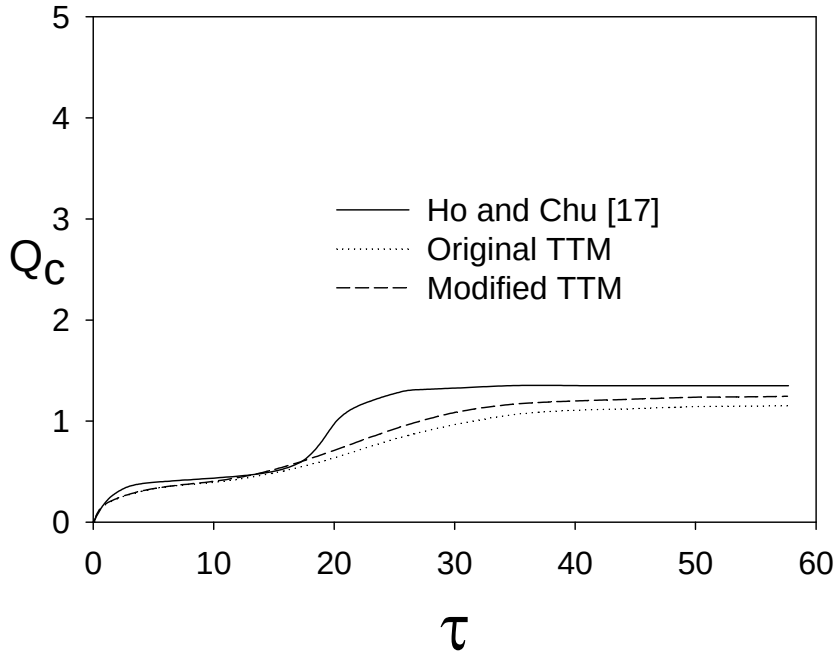

Fig. 3-6 Comparison of volume fraction and total heat on right and left walls (grid size: 40×40, time step $\Delta\tau = 0.1$)

Fig. 3-7 shows the comparison of the locations of the solid-liquid interface obtained by different models. It can be seen that the original TTM under predicts the melting rate of substance with heat capacity ratio less then one.

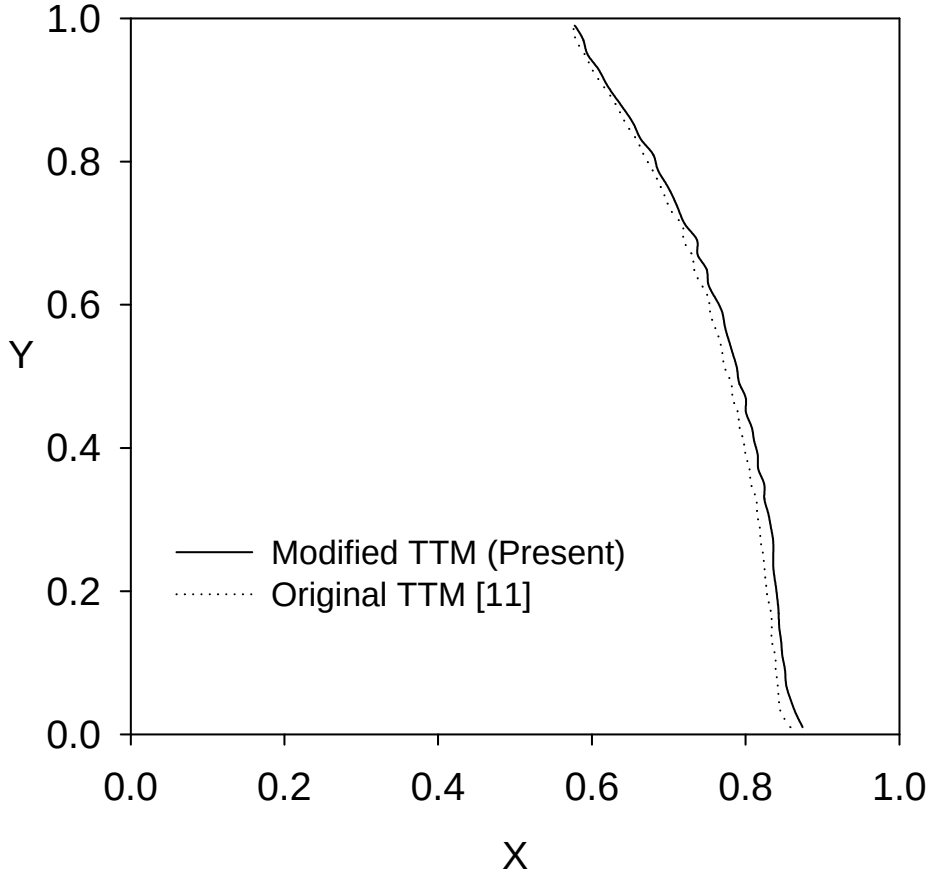

Fig. 3-7 Comparison of the locations of the melting fronts for water at time 57.7 (C_{sl} = 0.477, K_{sl} = 3.793, grid size 50x50, time step = 10^{-4})

Finally, melting of a substance with heat capacity ratio higher than 1 (Acetic Acid, C_{sl} = 1.203) was studied. The Acetic acid has K_{sl} of 1.2 and Prandtl number of 14.264. The Stefan number is chosen to be 0.045. The optimum grid size for melting of acetic acid cases is 40×40 and the time step is 0.1. Since the original TTM uses the average of heat capacity in mushy zone and it under predicts the total heat transfer when the heat

capacity ratio less than one, so the opposite effect is expected when the ratio is higher than one. Fig. 3-8 shows that the original TTM over predicts the movement of solid-liquid interface when the working fluid has heat capacity ratio higher than one.

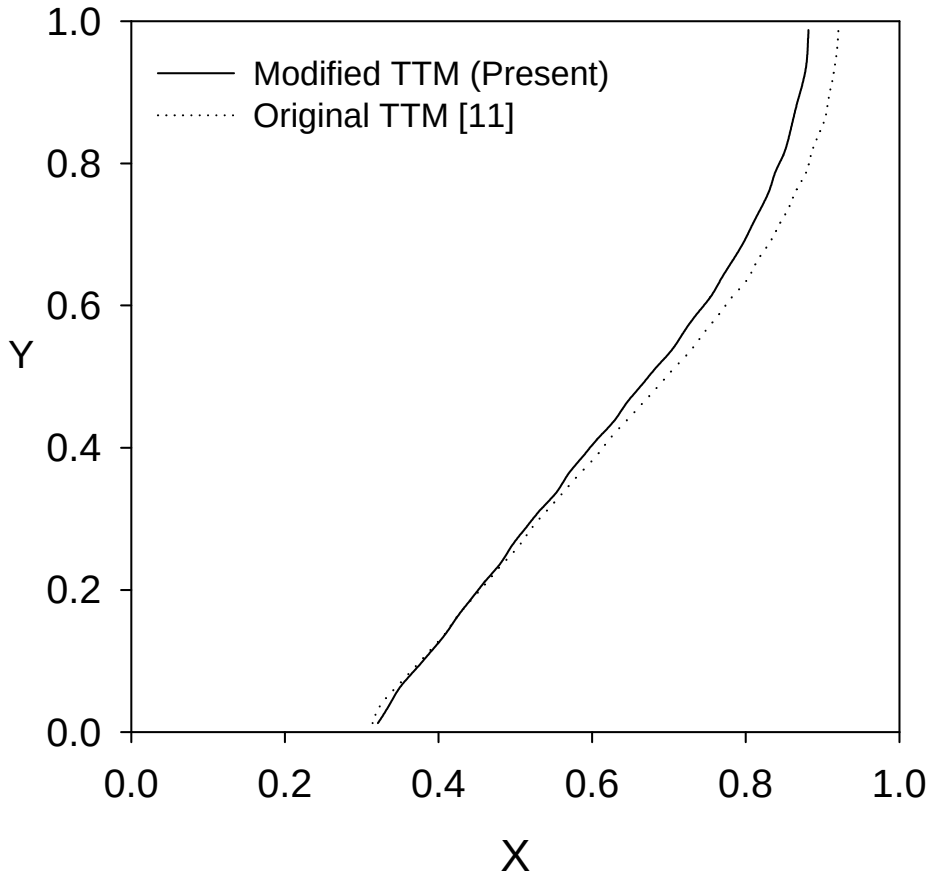

Fig. 3-8 Comparison of the locations of the melting fronts for acetic acid at time 100 (C_{sl} = 1.203, K_{sl} = 1.2, grid size 40x40, time step = 0.1)

Fig. 3-9 shows velocity vector for the acetic acid flow inside the rectangular cavity, which is also consistent with conventional natural convection with high temperature at the left-wall.

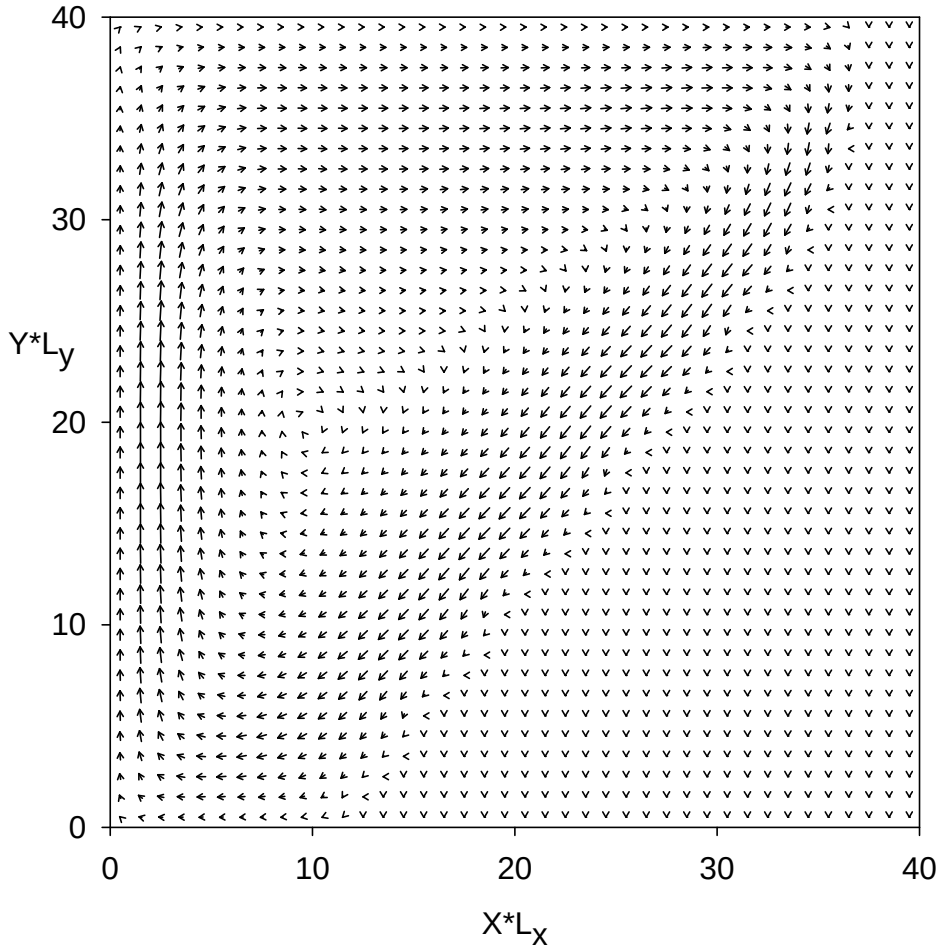

Fig. 3-9 Velocity vector for acetic acid at time 57.7(C_{sl} = 1.203, K_{sl} = 1.2, grid size 40x40, time step = 0.1)

3.5. Conclusions

A modified TTM was proposed and numerical simulation for three substances were carried out. Even for the PCM with heat capacity ratio close to one, the present model yields results closer to the experimental results than the original TTM. The difference in melting rate prediction becomes larger when the heat capacity ratio is further away from

one and that the modified TTM will give better prediction than original TTM. Since the original TTM uses average heat capacity in the mushy zone, it will under predict the location of the interface when heat capacity ratio is less than one and it will over predict when the ratio is larger than one.

CHAPTER 4 MELTING AND SOLIDIFICATION IN POROUS MEDIA

Melting and solidification in porous media can find application in a wide range of problems, including the freezing of water in soil [37], frozen food [38], water barrier in construction and mining processes [39], chill casting [1], slab casting [40], liquid metal injection [41], latent-heat thermal-energy storage [42], laser annealing [43], selective laser sintering (SLS) [44, 45] and laser drilling [46, 47], etc. While the early studies about phase change in porous media treated melting and solidification as conduction-controlled, the effect of natural convection is often very important. With the proven capabilities of TTM in wide range of applications, the model was employed to analyze of the performance of latent heat thermal energy storage systems [48, 49]. Zhang and Faghri used TTM to study phase change in microencapsulated PCM [50] and externally finned tube [9, 10]. Other research areas that TTM was extended into are selective laser sintering (SLS) of metal powder [44, 45] and laser drilling process by Ganesh et. al. [46, 47].

As Haeupl and Xu [51] stated, the most famous and commonly used model for phase-change in soil science is the Harlan model [52] which is a two-temperature model. Although it is possible for a two-temperature model to give analytical solution on some simple problems, it requires heavy mathematical maneuvers and few assumptions to locate the phase-change front as indicated by Harris et al. [53]. Fortunately, it is possible to simplify the calculation for phase change in porous media by employing a single-

temperature model to a fixed grid. Beckermann and Viskanta [54] proposed a generalized model based on volume averaged governing equations that are applicable to the entire computational domain. This model includes the effect of inertia terms which consequently allow non-slip conditions at the wall, unlike Darcy's law which is valid only at very low velocity and assumes slip condition at the wall. Even with the assumption, the model can handle even more complicated problems when the density of PCM varies with temperature [55].

In this chapter, the results from Beckermann and Viskanta [54] will be compared to the present results for the validation of the model on both melting and solidification in porous media. Beckermann and Viskanta used a model that is based on the volumetric averaging technique for obtaining the macroscopic conservation equations. In that technique, the microscopic equations that are valid for each phase are integrated over a small volume element. Clearly, if the present result can match up well to the result from Ref [54], the present model will be more sufficient in term of computational time.

4.1. Physical Model

Melting and solidification inside a rectangular enclosure as shown in Fig. 4-1 will be studied in this chapter. For melting cases, the top and bottom walls are insulated, while the left and right walls are kept at high constant temperature T_h = 0.6 and low constant temperature T_c = -0.4, respectively. For melting problems, the phase change material starts in solid phase with the initial temperatures T_c in all cases, which is above the fusion temperature T_m = 0.0. The melting starts after the left wall is heated to temperature T_h,

and then progresses from left to right. For solidification cases, the top and bottom walls are insulated, while the left and right walls are kept at high constant temperature T_h = 0.5 and low constant temperature T_c = -0.5, respectively. The phase change material starts in solid phase with the initial temperatures T_h in all cases. The solidification process begins after the right wall is cooled down to temperature T_c, then it progresses from l to left. The dimensionless parameters for gallium/glass combination case are Pr = 0.0208, Da = 1.37 × 10^{-5}, Ra = 8.409 × 10^5, Ste = 0.1241, C_{sl} = 0.89, C_p = 0.765, H = 1.0, and ε = 0.385. The thermal conductivities used in the calculation of effective thermal conductivity are k_s = 33.5, k_l = 32.0, and k_p = 1.4 W/m.K.

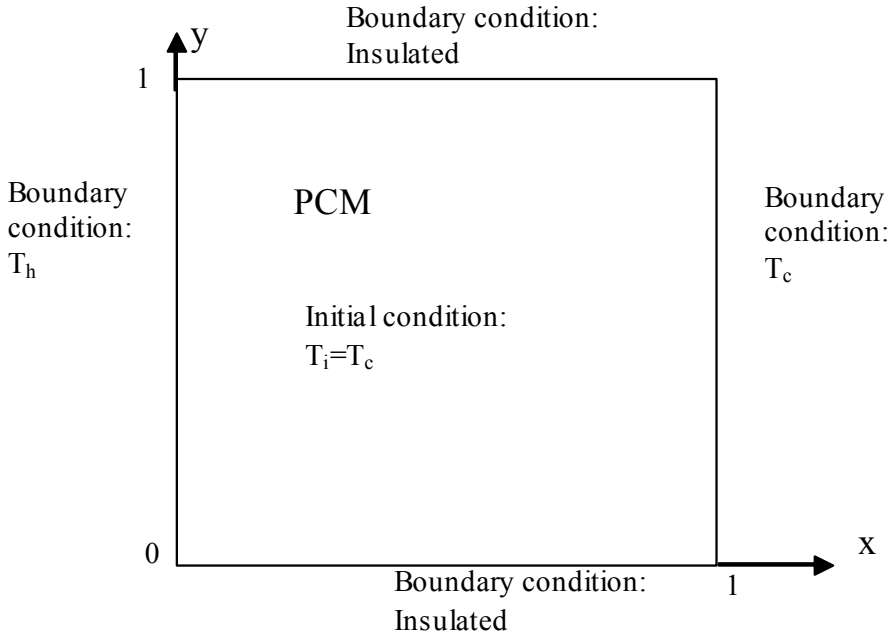

Fig. 4-1 Physical Model

4.2. Governing Equations

If the flow is incompressible and the Boussinesq approximation is valid, the continuity and momentum equations are

Continuity equation

$$\frac{\partial u}{\partial x}+\frac{\partial v}{\partial y}=0 \tag{4-1}$$

Momentum equations in x and y directions

$$\frac{\rho_l}{\varphi_l}\frac{\partial u_l}{\partial t}+\frac{\rho_l}{\varphi_l^2}\left(u_l\frac{\partial u_l}{\partial x}+v_l\frac{\partial u_l}{\partial y}\right)=-\frac{\partial p}{\partial x}+\frac{\mu_l}{\varphi_l}\left(\frac{\partial^2 u_l}{\partial x^2}+\frac{\partial^2 u_l}{\partial y^2}\right)-u_l\left(\frac{\mu_l}{K}+\frac{\rho C}{\sqrt{K}}|u_l|\right) \tag{4-2}$$

$$\frac{\rho_l}{\varphi_l}\frac{\partial v_l}{\partial t}+\frac{\rho_l}{\varphi_l^2}\left(u_l\frac{\partial v_l}{\partial x}+v_l\frac{\partial v_l}{\partial y}\right)=-\frac{\partial p}{\partial y}+\frac{\mu_l}{\varphi_l}\left(\frac{\partial^2 v_l}{\partial x^2}+\frac{\partial^2 v_l}{\partial y^2}\right)-v_l\left(\frac{\mu_l}{K}+\frac{\rho C}{\sqrt{K}}|v_l|\right)-\rho g\beta\left(T^0-T^0_{ref}\right) \tag{4-3}$$

where u_l is the average (pore) velocity of the liquid. The forth and fifth terms on the right hand side of equation (4-2) and (4-3) account for the first and second order drag forces, namely Darcy's term and Forchheimer's extension respectively. The Boussinesq approximation is represented by the last term of equation (4-3). It is important to note that the velocity used in the equation is the average velocity, not the superficial (Darcian) velocity which can be defined as

$$u=\varphi_l u_l \tag{4-4}$$

The value of the permeability, K, can be calculated from the Kozeny-Carman equation

$$K(\varphi_l)=\frac{d_m\varphi_l^3}{175(1-\varphi_l)^2} \tag{4-5}$$

where d_m is the mean diameter of the beads. The value of the inertia coefficient C in Forchheimer's extension has been measured experimentally by Ward [56], which was found to be 0.55 for many kinds of porous media. Since the modified TTM has been proven to perform well in phase change process, we used it for the energy equation.

Energy equation

$$\frac{\partial\left(C^0T^*\right)}{\partial t}+\frac{\partial\left(C^0uT^*\right)}{\partial x}+\frac{\partial\left(C^0vT^*\right)}{\partial y}=\frac{\partial}{\partial x}\left(k\frac{\partial T^*}{\partial x}\right)+\frac{\partial}{\partial y}\left(k\frac{\partial T^*}{\partial y}\right)-\left[\frac{\partial\left(S^0\right)}{\partial t}+\frac{\partial\left(S^0u\right)}{\partial x}+\frac{\partial\left(S^0v\right)}{\partial y}\right] \quad (4\text{-}6)$$

where $T^* = T^0 - T_m^0$ is scaled temperature and coefficients C^0 and S^0 in equation (4-6) are

$$C^0\left(T^0\right)=\begin{cases}\left(\rho c\right)_s, & T^0-T_m^0<-\Delta T^0\\ \dfrac{\left(\rho c\right)_l+\left(\rho c\right)_s}{2}+\dfrac{\rho h_{sl}}{2\Delta T^0}+\dfrac{\left(\rho c\right)_l-\left(\rho c\right)_s}{4}\left(T^0-T_m^0\right), & -\Delta T^0\le T^0-T_m^0\le\Delta T^0\\ \left(\rho c\right)_l, & T^0-T_m^0>\Delta T^0\end{cases} \quad (4\text{-}7)$$

$$S^0\left(T^0\right)=\begin{cases}\left(\rho c\right)_s\Delta T^0, & T^0-T_m^0<-\Delta T^0\\ \dfrac{\left(\rho c\right)_l+3\left(\rho c\right)_s}{4}\Delta T^0+\dfrac{\rho h_{sl}}{2}, & -\Delta T^0\le T^0-T_m^0\le\Delta T^0\\ \left(\rho c\right)_s\Delta T^0+\rho h_{sl}, & T^0-T_m^0>\Delta T^0\end{cases} \quad (4\text{-}8)$$

and the thermal conductivity is

$$k\left(T^0\right)=\begin{cases}k_{eff}, & T^0<T_m^0-\Delta T^0\\ k_{eff}+\left(k_l-k_{eff}\right)\dfrac{T^0-T_m^0+\Delta T^0}{2\Delta T^0}, & T_m^0-\Delta T^0\le T^0\le T_m^0+\Delta T^0\\ k_l, & T^0>T_m^0+\Delta T^0\end{cases} \quad (4\text{-}9)$$

where $T^0<T_m^0-\Delta T^0$ corresponds to the solid phase, $T_m^0-\Delta T^0\le T^0\le T_m^0+\Delta T^0$ to the mushy zone, and $T^0>T_m^0+\Delta T^0$ to the liquid phase. Note that the mushy zone is the

region where liquid and solid exist simultaneously. The effective conductivity of liquid phase, $k_{l,eff}$, should be calculated from

$$\frac{k_{eff}}{k_l} = (1-\alpha_0)\frac{\varepsilon f_0 + (1-\varepsilon f_0)k_p / k_l}{1-\varepsilon(1-f_0)+\varepsilon(1-f_0)k_p / k_l} + \alpha_0 \frac{2(1-\varepsilon)(k_p / k_l)^2 + (1+2\varepsilon)k_p / k_l}{(2+\varepsilon)k_p / k_l + 1 - \varepsilon} \quad (4\text{-}10)$$

where k_l is the thermal conductivity for the liquid phase of the PCM. The effective thermal conductivity of the solid phase can be obtained by replacing k_l in eq. (4-10) with k_s. Introducing these following non-dimensional variables:

$$X = \frac{x}{H},\ Y = \frac{y}{H},\ \mathrm{U} = \mathrm{u}\frac{\mathrm{H}}{\alpha_l},\ \mathrm{V} = \mathrm{v}\frac{\mathrm{H}}{\alpha_l},\ \tau = \frac{\alpha_l t}{H^2},\ T = \frac{T^0 - T_m^0}{T_h^0 - T_c^0},$$

$$\Delta T = \frac{\Delta T^0}{T_h^0 - T_c^0},\ C_L = \frac{C^0}{(\rho c)_l},\ C_P = \frac{(\rho c)_p}{(\rho c)_l},\ S = \frac{S^0}{(\rho c)_l (T_h^0 - T_c^0)},\ \kappa = \frac{K_\varepsilon}{K_l},\ Da = \frac{K_\varepsilon}{L^2},$$

$$Ste = \frac{c_l (T_h^0 - T_c^0)}{h_{sl}},\ C_{sl} = \frac{(\rho c)_s}{(\rho c)_l},\ K_{eff} = \frac{k_{eff}}{k_l},\ K_{s,eff} = \frac{k_{s,eff}}{k_l},\ K_{l,eff} = \frac{k_{l,eff}}{k_l}$$

$$Ra = \frac{g\beta(T_h^0 - T_c^0)H^3}{\nu_l \alpha_l},\ P = \frac{H^2}{\rho \nu_l^2}(p + \rho g) \quad (4\text{-}11)$$

The governing equations can be non-dimensionalized as:

$$\frac{\partial U}{\partial X} + \frac{\partial V}{\partial Y} = 0 \quad (4\text{-}12)$$

$$\frac{1}{\mathrm{Pr}_l}\left[\frac{1}{\varphi_l}\frac{\partial U}{\partial \tau} + \frac{1}{\varphi_l^2}\left(U\frac{\partial U}{\partial X} + V\frac{\partial U}{\partial Y}\right)\right] = -\frac{\partial P}{\partial X} + \frac{1}{\varphi_l}\left(\frac{\partial^2 U}{\partial X^2} + \frac{\partial^2 U}{\partial Y^2}\right) - U\left(\frac{\zeta}{Da} + \frac{C}{\mathrm{Pr}_l}\sqrt{\frac{\zeta}{Da}}|U|\right) \quad (4\text{-}13)$$

$$\frac{1}{\mathrm{Pr}_l}\left[\frac{1}{\varphi_l}\frac{\partial V}{\partial \tau} + \frac{1}{\varphi_l^2}\left(U\frac{\partial V}{\partial X} + V\frac{\partial V}{\partial Y}\right)\right] = -\frac{\partial P}{\partial Y} + \frac{1}{\varphi_l}\left(\frac{\partial^2 V}{\partial X^2} + \frac{\partial^2 V}{\partial Y^2}\right) - V\left(\frac{\zeta}{Da} + \frac{C}{\mathrm{Pr}_l}\sqrt{\frac{\zeta}{Da}}|V|\right) + RaT \quad (4\text{-}14)$$

$$\frac{\partial(CT)}{\partial\tau}+\frac{\partial(UC_LT)}{\partial X}+\frac{\partial(VC_LT)}{\partial Y}=\frac{\partial}{\partial X}\left(\frac{K_{eff}}{\mathrm{Pr}_l}\frac{\partial T}{\partial X}\right)+\frac{\partial}{\partial Y}\left(\frac{K_{eff}}{\mathrm{Pr}_l}\frac{\partial T}{\partial Y}\right)-\left(\frac{\partial S}{\partial\tau}+\frac{\partial(US)}{\partial X}+\frac{\partial(VS)}{\partial Y}\right) \quad (4\text{-}15)$$

where

$$C=(1-\varepsilon)C_P+\varepsilon C_L \quad (4\text{-}16)$$

$$C_L=\begin{cases}C_{sl}, & T<-\Delta T\\ \dfrac{1+C_{sl}}{2}+\dfrac{1}{2Ste\Delta T}+\dfrac{1-C_{sl}}{4\Delta T}T, & -\Delta T\le T\le\Delta T\\ 1, & T>\Delta T\end{cases} \quad (4\text{-}17)$$

$$S=\begin{cases}C_{sl}\Delta T, & T<-\Delta T\\ \dfrac{1+3C_{sl}}{4}\Delta T+\dfrac{1}{2Ste}, & -\Delta T\le T\le\Delta T\\ C_{sl}\Delta T+\dfrac{1}{Ste}, & T>\Delta T\end{cases} \quad (4\text{-}18)$$

and the thermal conductivity is

$$K_{eff}=\begin{cases}K_{s,eff}, & T<-\Delta T\\ \dfrac{K_{l,eff}+K_{s,eff}}{2}+\dfrac{\left(K_{l,eff}-K_{s,eff}\right)}{2\Delta T}T, & -\Delta T\le T\le\Delta T\\ K_{l,eff}, & T>\Delta T\end{cases} \quad (4\text{-}19)$$

The melting in porous media is now described by 7 dimensionless parameters: *Pr, Da, Ra, Ste* C_{sl}, C_p, *and* K_{eff}.

4.3. Numerical Solution Procedure

The dimensionless conservative equations were solved numerically utilizing the iterative SIMPLE algorithm. The power law scheme was used to approximate the combined convective and diffusive fluxes. The harmonic mean function was used for the diffusion coefficients which ensure physically realistic results for abrupt changes in these coefficients. The governing equations were solved throughout the physical domain including the solid region, in which the velocities were controlled to zero by RSOM.

After many trials of 20×20, 40×40, 50×50, 80×80, 100×100, 80×50, and 100×50 grids, a grid of 100×50 nodal points and a dimensionless time step of $\tau = 1\times10^{-3}$ were utilized for all cases because they give results at minimal computational time. The lower grids couldn't give reasonable results while the higher grids didn't significantly improve the results. Thus the selected grid sizes and time steps should be viewed as a compromise between accuracy and computational time. For each time step, the iterations were terminated when the relative dependent variables (values at each node divided by maximum values) were less than the convergence criteria: 1×10^{-3} for x- and y-velocities, 1×10^{-6} for temperature, and 1×10^{-7} for maximum residual source of mass. It must be stated that relaxation factor must be used for all source terms in all solidification cases to account for large amount of fluid at the beginning, while all melting cases do not need any relaxation. Additional test of the accuracy were performed for fluid flow in rectangular enclosure without porous media and good agreement was found.

4.4. Results and discussions for melting in porous media

The modified TTM is validated by comparison with numerical and experimental results provided by Beckermann and Viskanta [54]. They chose gallium as the phase change material and glass bead as the porous medium. We used the same values for all parameters to make sure the only difference is the treatment of energy equation.

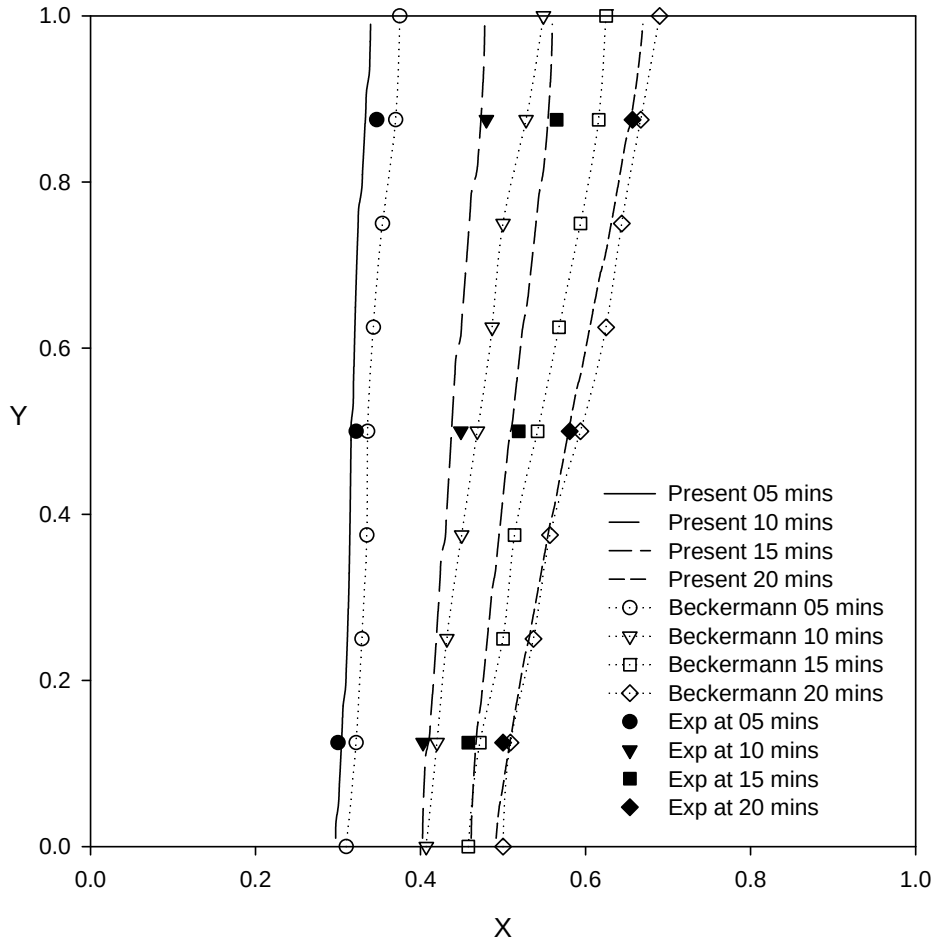

Fig. 4-2 Comparison of the locations of the melting fronts from experiment, Beckermann, and modified TTM at different times.

Fig. 4-2 shows the location of the melting front, which is identified by fusion temperature, at different time. The results show relatively weak natural convection when comparing to conduction. This is expected since the small Darcy number and the high effective thermal conductivity of gallium-glass mixture suppress natural convection flow. At the beginning, conduction dominates the melting process as represented by the interface aligning almost vertically. The interface becomes more incline as the melting continues toward steady state. This is an indication of natural convection showing its effects when the volume of fluid grows larger and the fluid circulates at increasing speed. The melting process reaches the steady state when heat received from the high-temperature wall on the left is equal to the heat released through the low-temperature wall on the right.

The modified TTM and the combined energy equation of Beckermann and Viskanta generally give very good prediction on the interface location comparing to the experimental results. However, the combined energy equation tends to over predict the speed of melting process especially after the natural convection started to show its effect, while the modified TTM can stay closer to the experimental results throughout the whole melting process. This could be the results of difference treatment to effective thermal conductivity and heat capacity in the mushy zone. The equation (4-10) gives effective thermal conductivity that is specialized for cases when the difference of thermal conductivities of PCM and porous media are very large, and it has wider range of applications (see [57]). The modified TTM also threat the fluid fraction as a function of temperature as shown in equation (4-13). Consequently, the latent heat is included into heat capacity calculation and has direct link to temperature, unlike in combined energy

equation which threats latent heat as a separate source term. The modified TTM can predict the interface location with the error less than 6% at any point and any time.

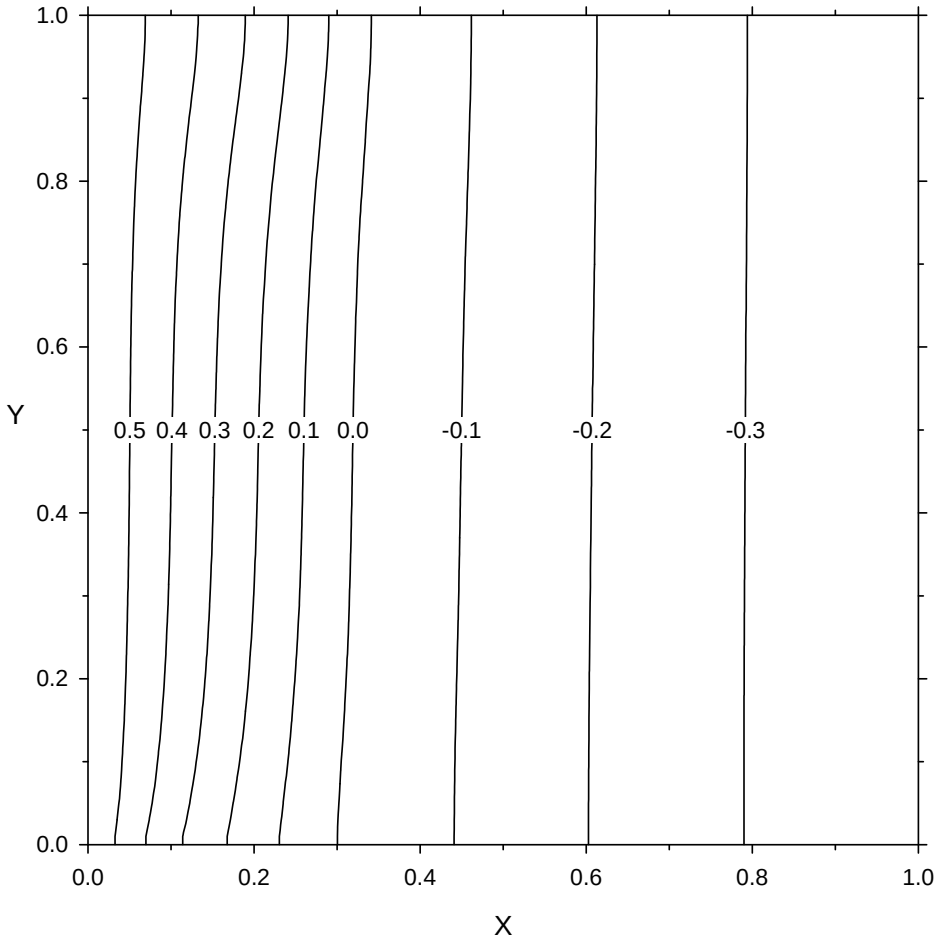

(a)

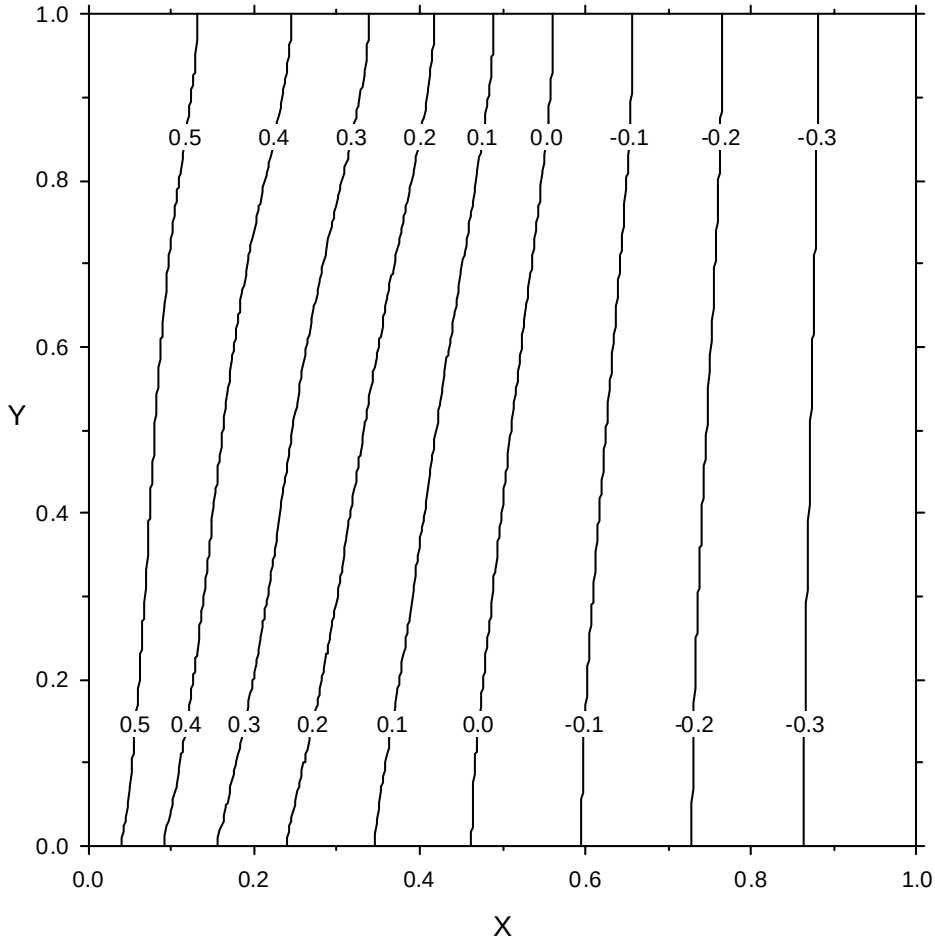

(b)

Fig. 4-3 Temperture distribution from modified TTM at (a) 5 min and (b) 15 min.

It is a good idea to study deeper into temperature distribution to acquire more detailed analysis. Fig. 4-3 shows temperature distribution at 5 and 15 minutes which confirms that the melting process starts from conduction dominated then converts to convection dominated in later stages. The more subtle information that can be deducted from Fig. 4-3 is that, in the earlier stage, the temperature gradients in the liquid region are much

higher than those in the solid region. If we focus on a very small control volume at the interface, keeping in mind that the thermal conductivities of solid and liquid gallium are very close (solid is only 5% higher liquid), it is clear that heat transferring into the control volume is much higher than transferring out hence melting occurs. As time goes on, temperature gradients in liquid region decrease while gradients in solid region increase, meaning the difference of heat going in and out of the control volume decreases. In other word, the heat responsible for phase change decreases, so the melting process consequently slows down. We want to clarify that temperature profiles are always perpendicular to the top and bottom walls just because of the adiabatic boundary conditions. Also, it can be seen that the mushy zone, identified by $-\Delta T \leq T \leq \Delta T$, may start with lower average temperature because majority of the region is in the lower part of the temperature range. As the melting progresses, the average temperature of the mushy should increase. This indicates that the movement in mushy zone is restricted hence the effect of convection is minimal in the beginning, and then the restriction is gradually lifted when the average temperature increases. This mechanism contributes to, and once again confirms, the transition from conduction to convection dominated melting process. Fig. 4-4 shows the approximate size of the mushy zone which identified by temperature.

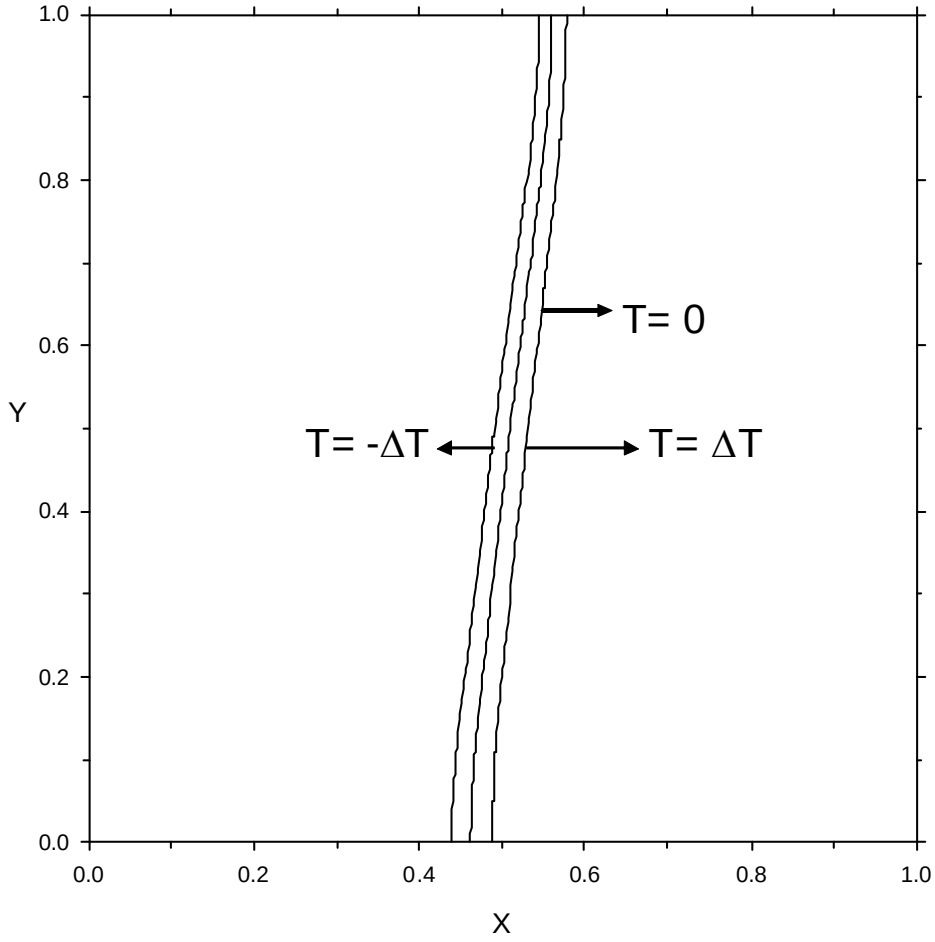

Fig. 4-4 The approximation of mushy zone.

This temperature validation has established some reliability of the model, so we further study streamline to strengthen our confidence in the model. The streamline is defined as

$$\psi = \int U dY - \int V dX. \tag{4.19}$$

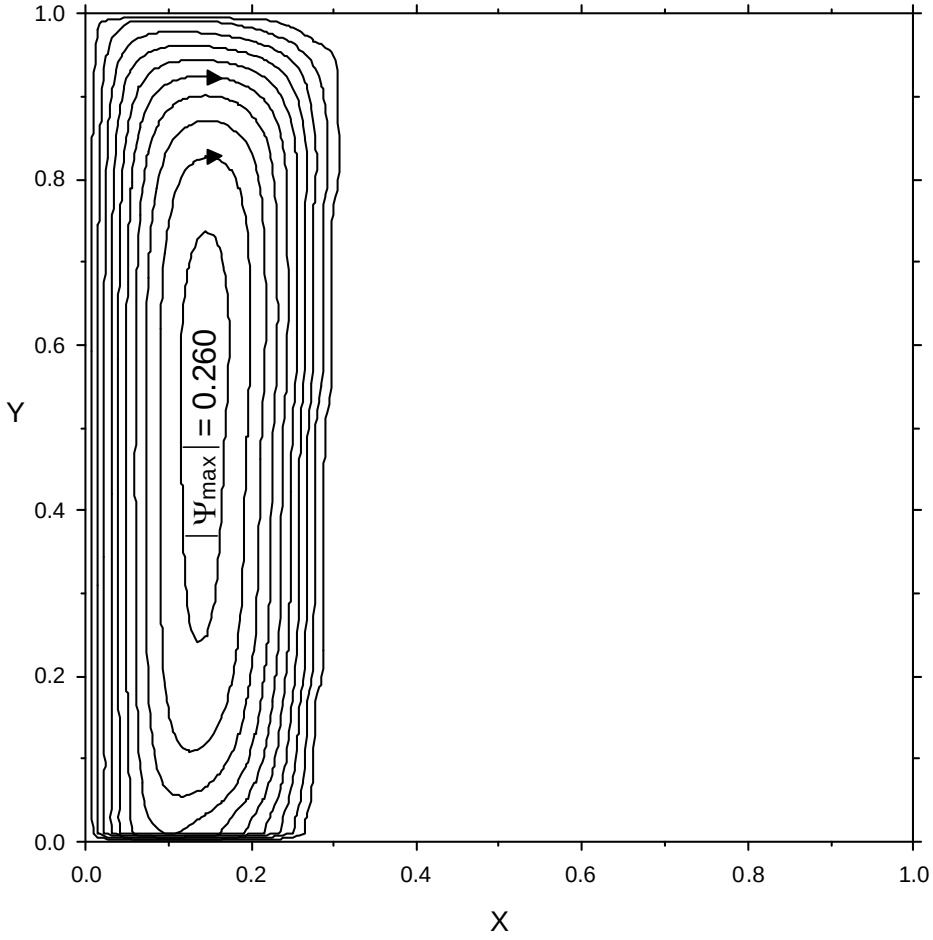

(a)

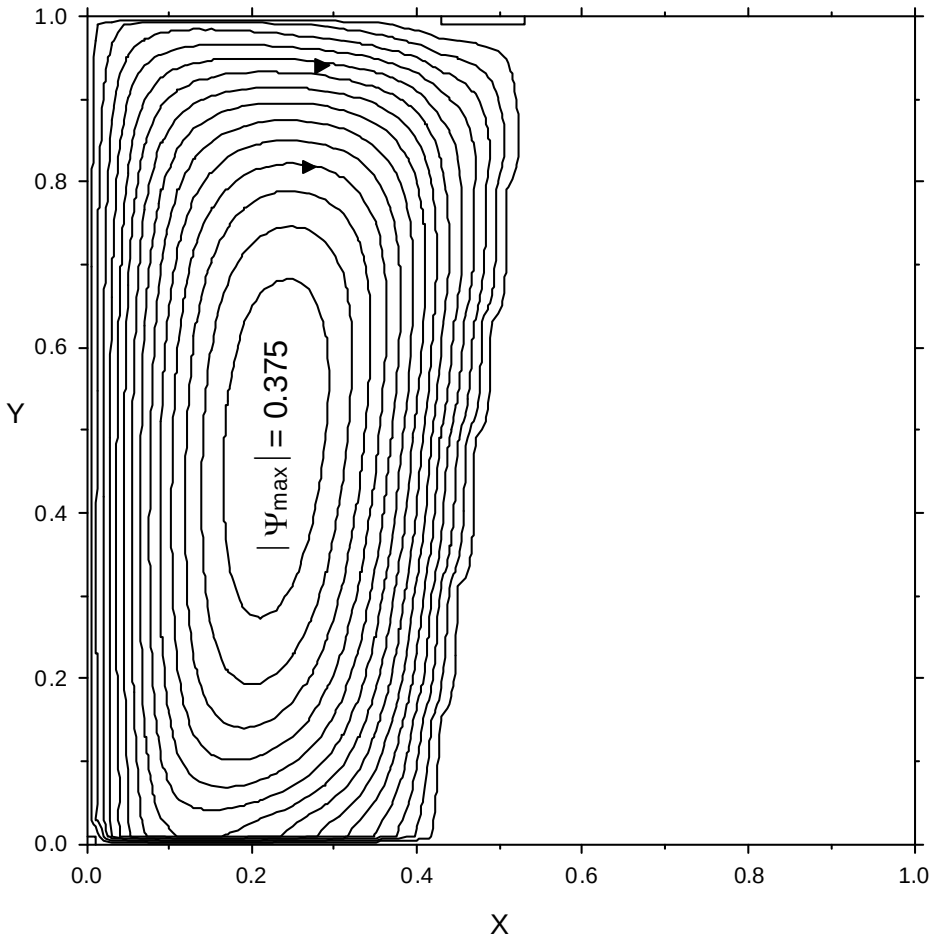

(b)

Fig. 4-5 Streamlines from modified TTM at (a) 5 min and (b) 15 min.

Fig. 4-5 shows streamline at 5 and 15 minutes where melting process is influenced by typical natural convection. The fluid is heated by the left wall and rises toward the top wall. The hot fluid near the top wall moves faster and impinges upon the solid causing it to melt faster. The melting rate decreases because the fluid is cooled down as it descends along the interface and toward the bottom wall. It may also be seen that the streamline

values increases as the flow develops, which illustrates increasing average velocity of the liquid flow. As a result, the curvature of the interface increases when convection is stronger. We would like to point out that the temperature and streamline distribution at 15 minute mark are similar to those at steady state (nearly 30 minutes), so it can be concluded that the flow filed and temperature are almost fully developed at this stage.

The very strong agreement between experimental results [54] and the numerical results from the modified TTM, as described above, has led to a successful validation of the model. With full confidence that the modified TTM can give good results for melting in porous media problems, we would like to apply the model to another combination of materials which is more suitable for real applications. The combination consists of copper as PCM and steel as porous medium. The dimensionless parameters for copper/steel combination case are $Pr = 1.55 \times 10^{-3}$, $Da = 1.37 \times 10^{-5}$, $Ra = 1.28 \times 10^{6}$, $Ste = 0.0295$, $C_{sl} = 0.93$, $C_p = 1.09$, $H = 1.0$, and $\varepsilon = 0.385$. The thermal conductivities used in the calculation of effective thermal conductivity are $k_s = 352$, $k_l = 339$, and $k_p = 30$ W/m.K.

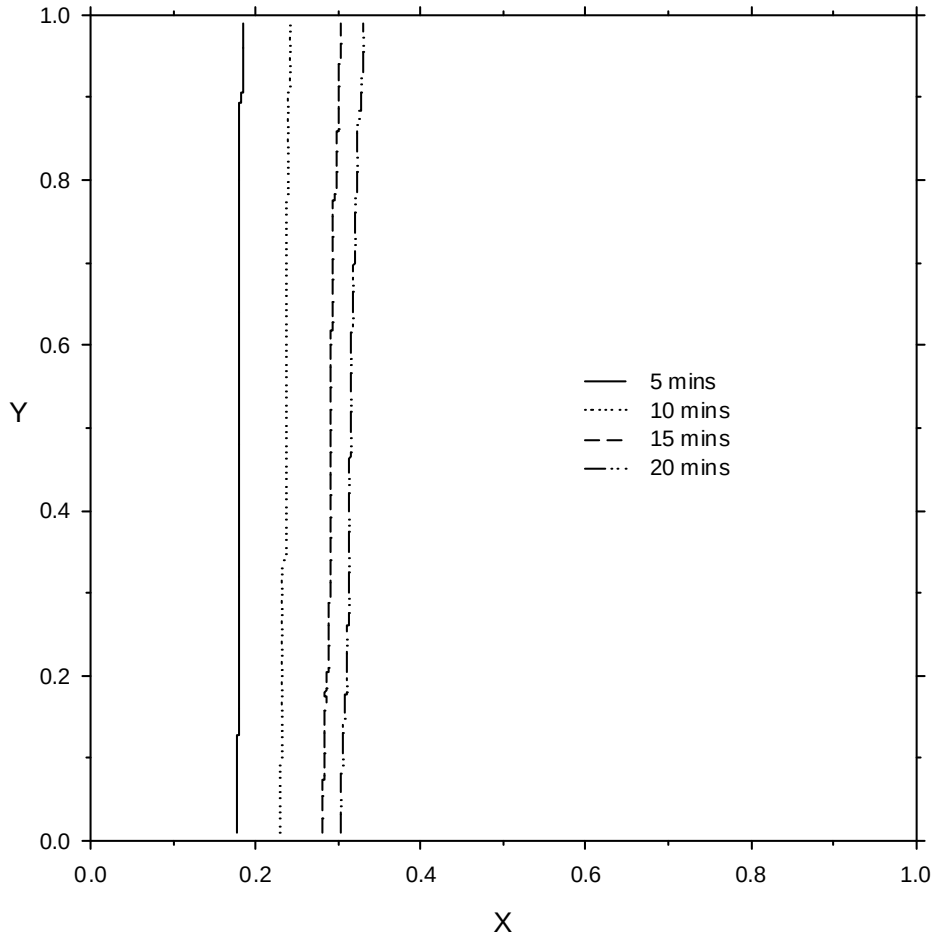

Fig. 4-6 Interface locations at different times for copper-steel combination.

Fig. 4-6 shows the melting front of copper at different time representing the melting process. The melting front is almost perpendicular to the insulated walls at the early stages. As time passes, there is little sign of convection effects. The melting at the top section of the domain only progresses slightly faster than the bottom section, which shows the dominance of conduction in the melting process. This is because the effective thermal conductivity of the copper-steel mixture is roughly twice as high as that of the gallium-glass mixture while the Rayleigh number increases only in a small percentage.

Such high effective thermal conductivity tends to suppress natural convection flow. Without the assistance of convection, the melting clearly progresses with slower speed, hence it reaches the steady state at lower volume of fluid.

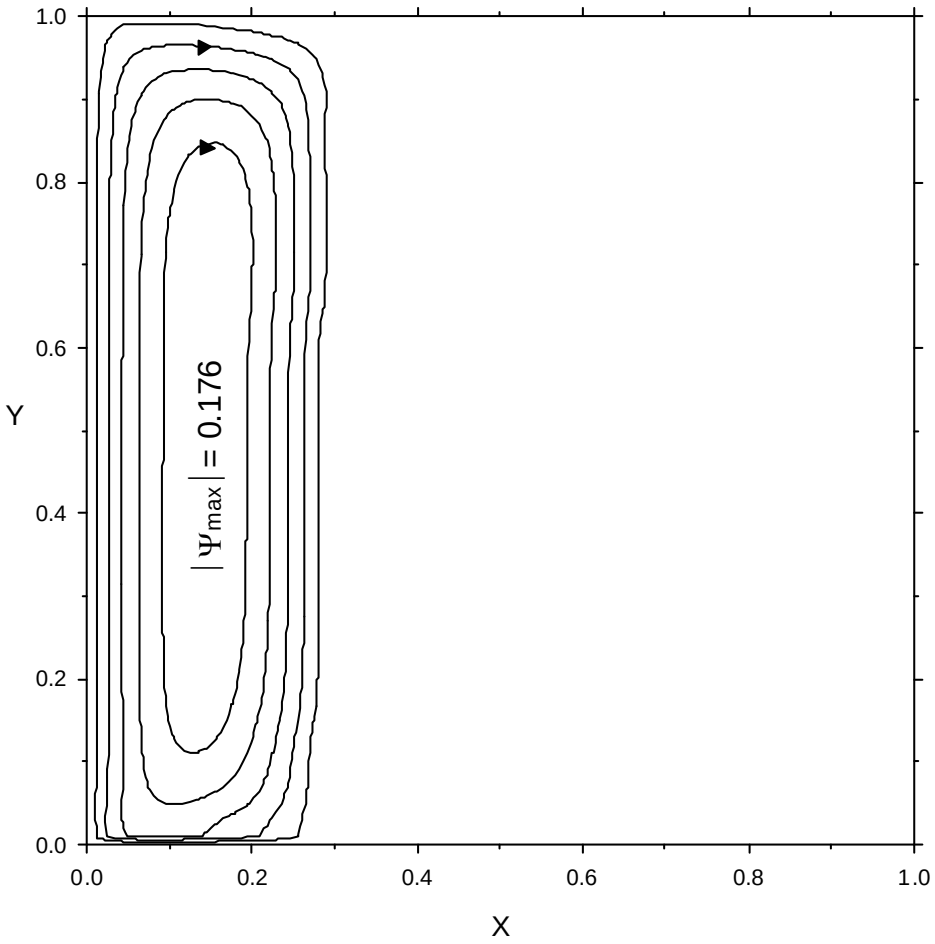

Fig. 4-7 Streamlines for copper-steel combination at 20 min.

Fig. 4-7 illustrates that natural convection still exists even when conduction very highly dominates the melting process. However, the circulation is too slow to cause any significant effects. The fluid still rises up along the hot wall and falls down along the

colder melting front. The impingement still causes the solid at the upper section to melt faster even at this slow velocity. The temperature distribution in Fig. 4-8 confirms the conduction dominated melting and the small effects of convection. The conduction dominated melting is represented through the parallel temperature distribution, while slightly incline temperature line shows the effects of convection.

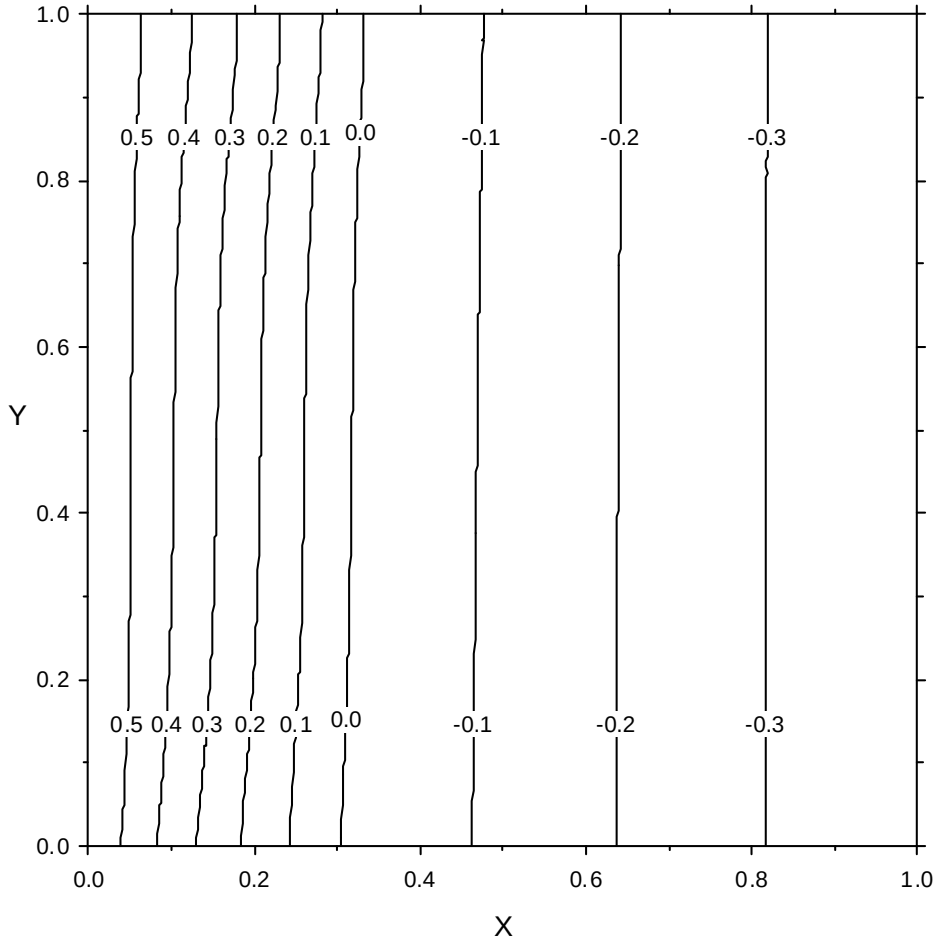

Fig. 4-8 Temperature distribution for copper-steel combination at 20 min.

The changes occurring after we study different materials lead us to a question of what parameters actually control the melting process. In other words, it is interesting to know the parameters that dictate types of melting process. After a careful consideration on the parameters involve in the governing equations, there are three parameters that may be the controlling parameters: Rayleigh number, Darcy's number, and subcooling number. To study the effects of these parameters, all other settings were kept unchanged and we only changed the focused parameter. The first parameter we studied was Rayleigh number as shown in Fig. 4-9. The case with actual Rayleigh number was compared with two other cases, one with an order of magnitude lower and the other with an order higher.

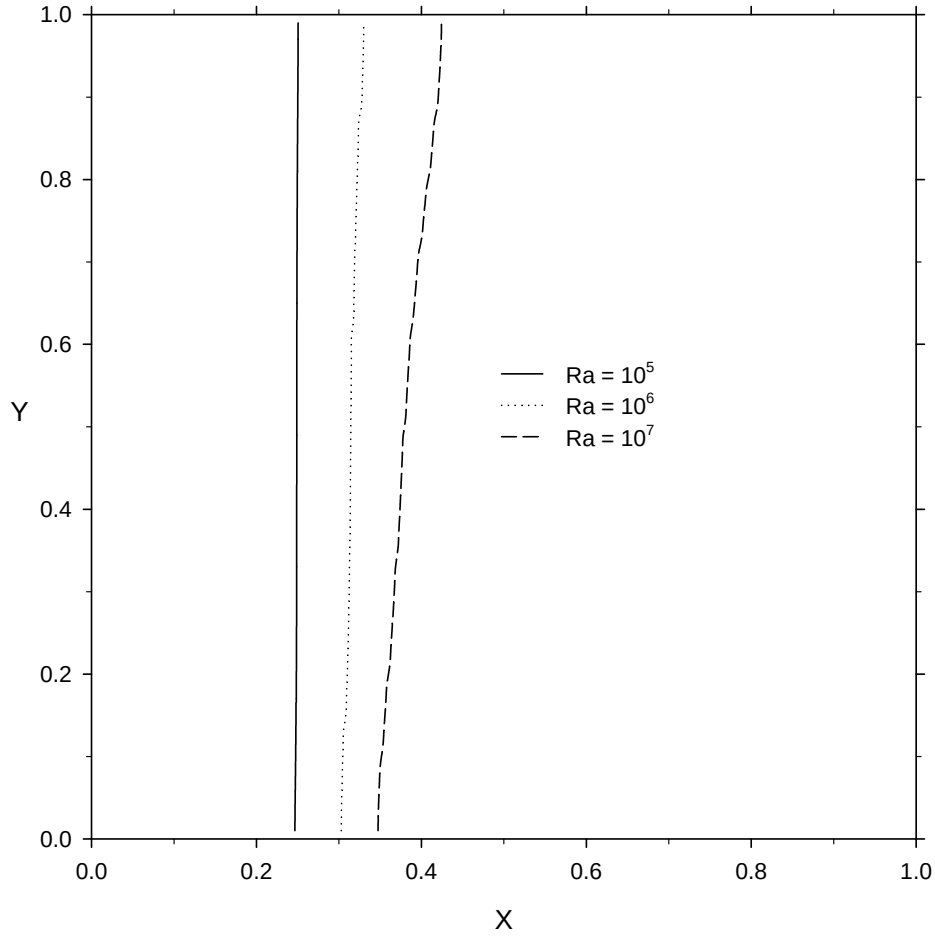

Fig. 4-9 Effects of Rayleigh number on melting process.

Fig. 4-9 shows that the interface becomes more incline when Rayleigh number increases; this means the significant of convection increasing with Rayleigh number. The higher Rayleigh number equals the larger body force due to natural convection pushing the fluid to move faster, hence increases convection effects. Fast moving fluid impinges on the melting front at higher velocity and increases melting rate near the top wall. Also high fluid velocity usually represent high convective heat transfer coefficient causing higher over all melting rate, hence melting process is faster with high Rayleigh number.

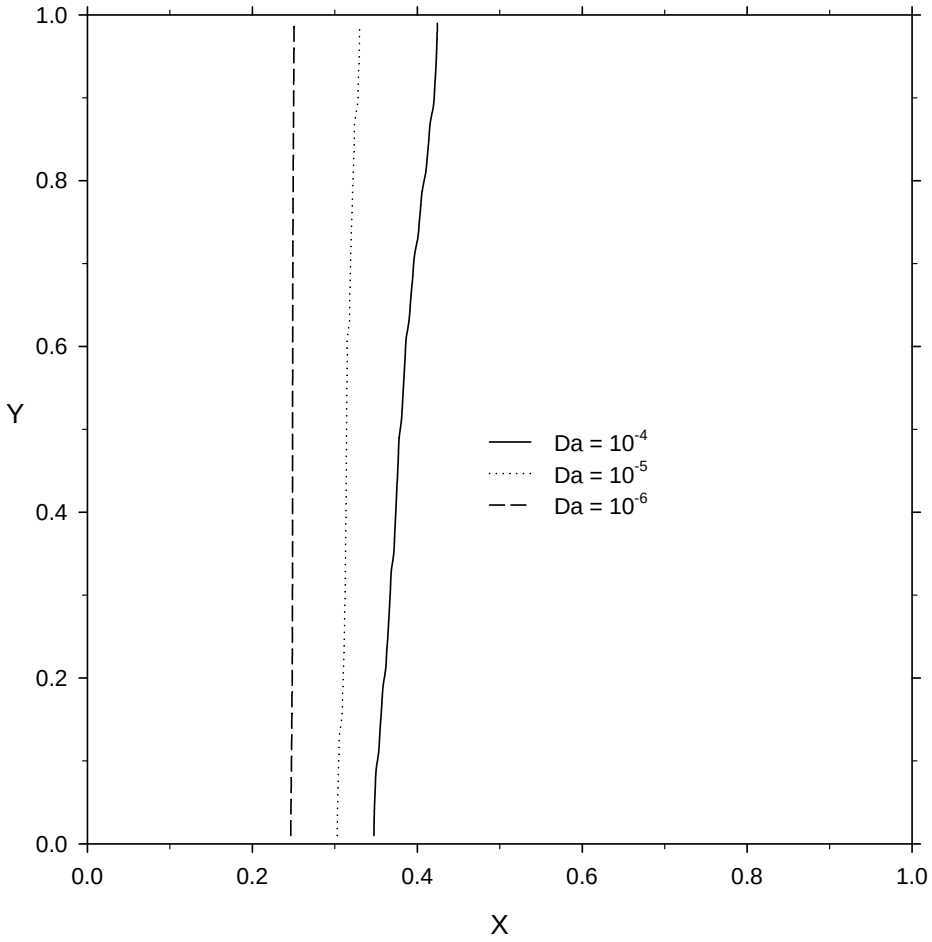

Fig. 4-10 Effects of Darcy's number on melting process.

Effects of Darcy's number is then studied and shown in Fig. 4-10. The similar results can be observed in this figure too. The presence of convection also increases with higher Darcy's number and it only indirectly affects the conduction. The increasing Darcy's number results in larger holes inside porous medium, which allows fluid to move with less restriction. When the fluid with same Ra moves with smaller drags it will move with higher speed and consequently promotes convection.

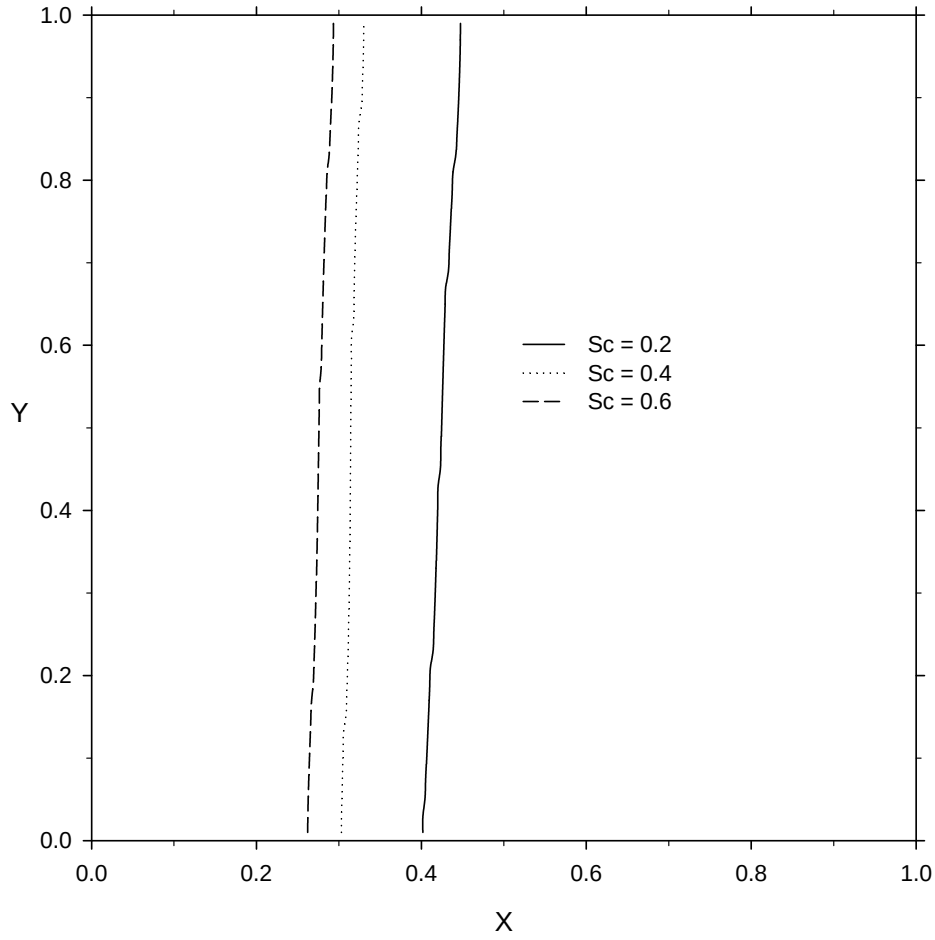

Fig. 4-11 Effects of subcooling number on melting process.

The last parameter is subcooling number shown in Fig. 4-11. The temperature at the hot wall remains the same for three cases of subcooling: 0.2, 0.4, and 0.6. The results show that the melting front moves faster with lower subcooling number, but it shows very little change in convection. The interface moves faster because of the higher temperature gradient caused by larger temperature difference between two vertical walls causing higher rate of conduction heat transfer. Even though the temperature difference also appears in Boussinesq approximation and one would expect its effects on convection, the results clearly show that the effects are negligible in this case.

4.5. Results and discussions for solidification in porous media

Fig. 4-12 shows the comparison between results from the modified TTM and numerical and experimental results of Beckermann and Viskanta. It is a comparison of interface location at different time. The solidification starts from the right wall and move toward the left wall as time passes. The results show relatively weak natural convection when comparing to conduction, which is reasonable since the small Darcy number and the high effective thermal conductivity of gallium-glass mixture suppress natural convection flow. At the beginning, it can be seen that the natural convection is strong in liquid region.

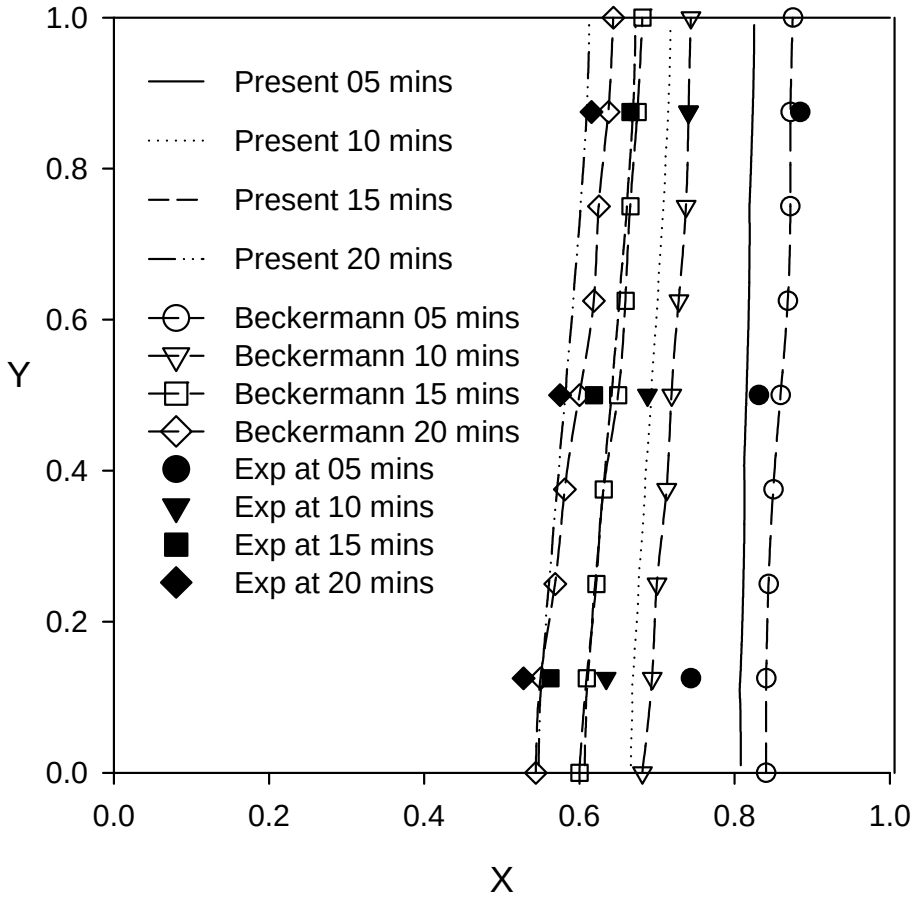

Fig. 4-12 Comparison of the locations of the interface from experiment, Beckermann, and modified TTM at different times.

As time increases, the solidification becomes conduction dominated and the interface becomes more vertical as the solidification continues toward steady state. This is because temperature gradient in solid decreases causing the solidification to slow down. The modified TTM and the combined energy equation of Beckermann and Viskanta generally give very good prediction on the interface location comparing to the experimental results. Although both models under predict the effects of natural convection at the early stage of the solidification, their performances improve as the process moves toward steady state. Generally, the combined energy equation tends to under predict the speed of melting process, while the modified TTM can stay relatively closer to the experimental results. The treatment of effective thermal conductivity and heat capacity in the mushy zone used in the modified TTM might be the reasons that enable the modified TTM to yield good results. The effective thermal conductivity obtained from equation (4-10) is suitable in wider range of material combination especially for cases when the difference of thermal conductivities of PCM and porous media are very large [57]. The modified TTM includes the latent heat into heat capacity calculation and has direct link to temperature, so it does not need to threat latent heat as a separate source term.

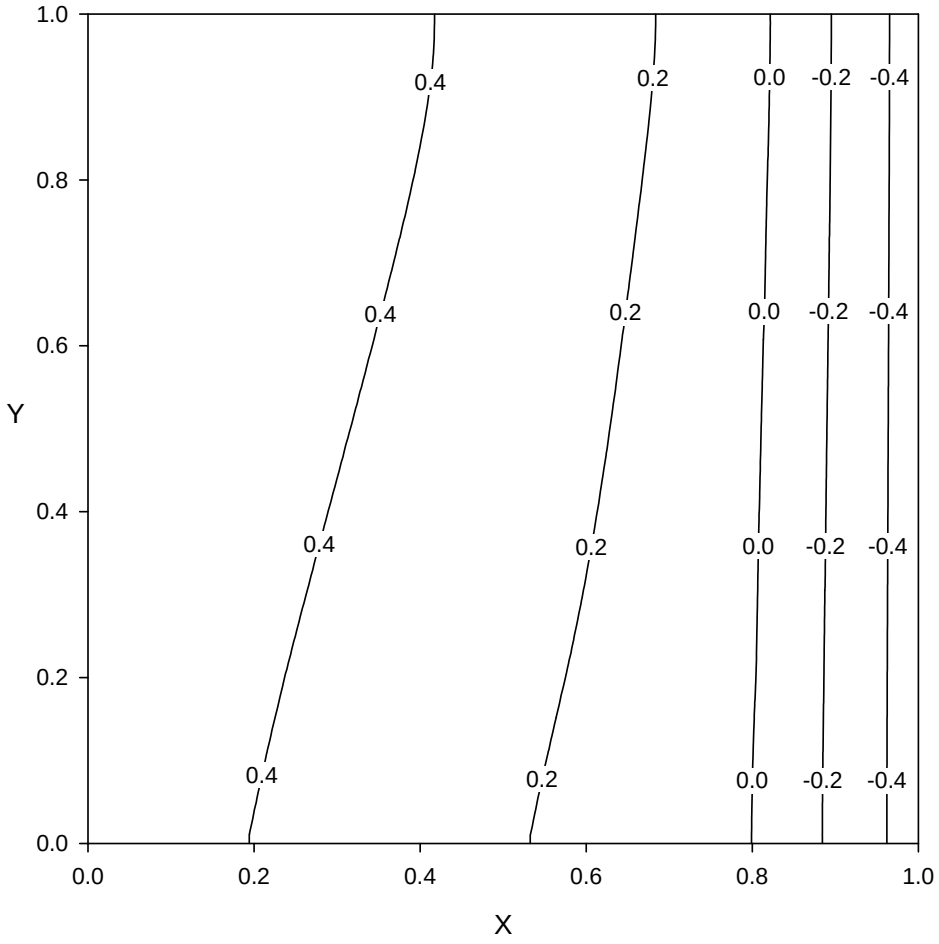

(a)

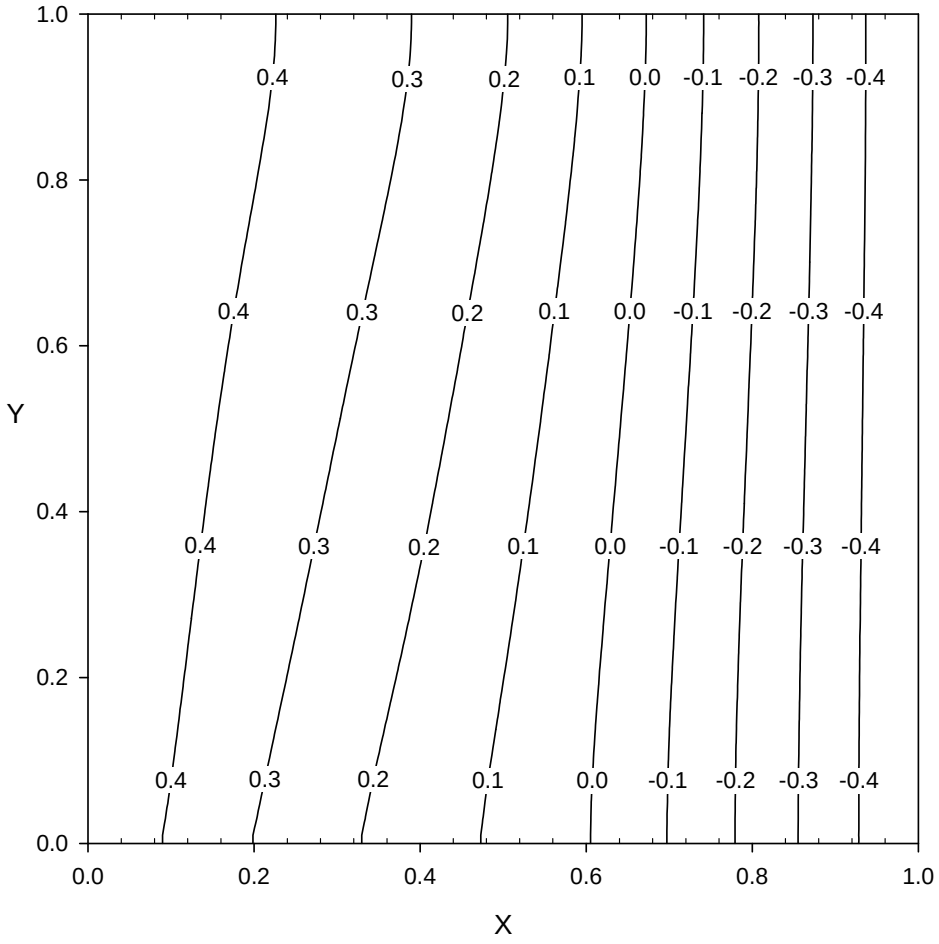

(b)

Fig. 4-13 Temperture distribution from modified TTM at (a) 5 min and (b) 20 min.

To achieve more detailed analysis, temperature distribution is studied in Fig. 4-13, which shows temperature distribution at 5 and 20 minutes. In the earlier stage, the temperature gradients in the solid region are much higher than those in the liquid region. That allows heat to move out of solid and consequently reduce the temperature in solid region. As a result, the solidification can process faster in earlier time. As time goes on, temperature gradients in liquid region increase while gradients in solid region decrease,

meaning the difference of heat going in and out at the interface decreases and solidification process consequently slows down.

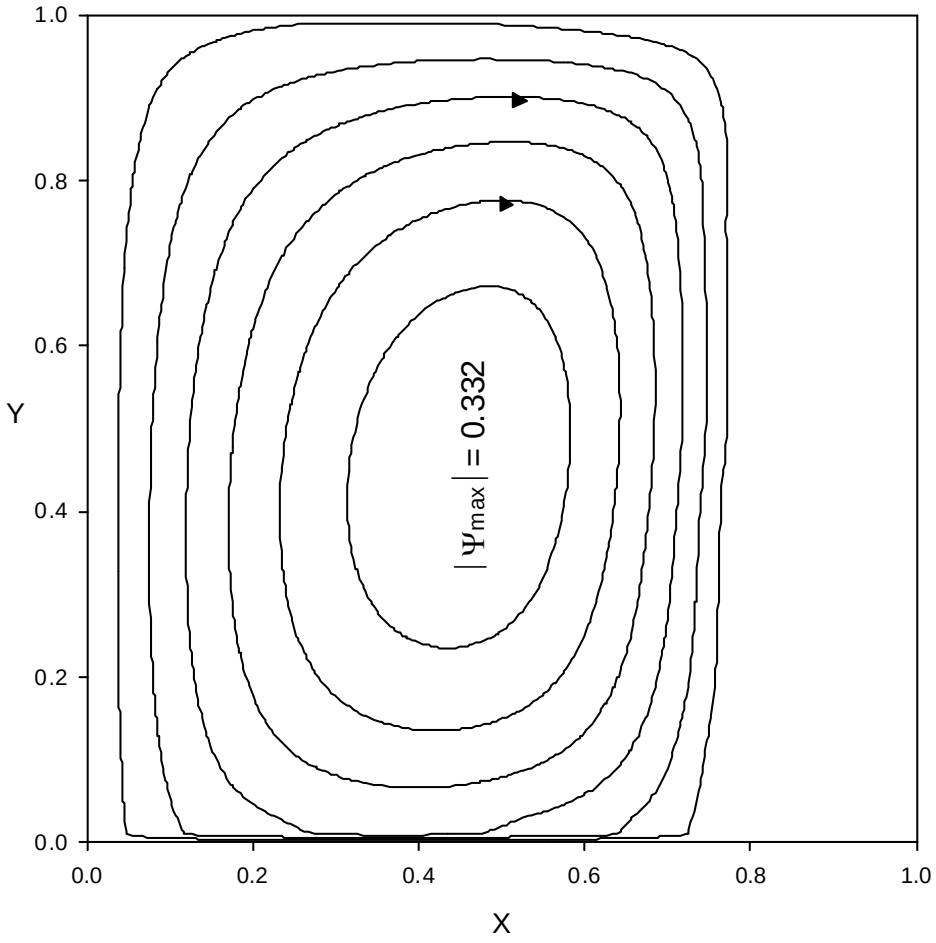

(a)

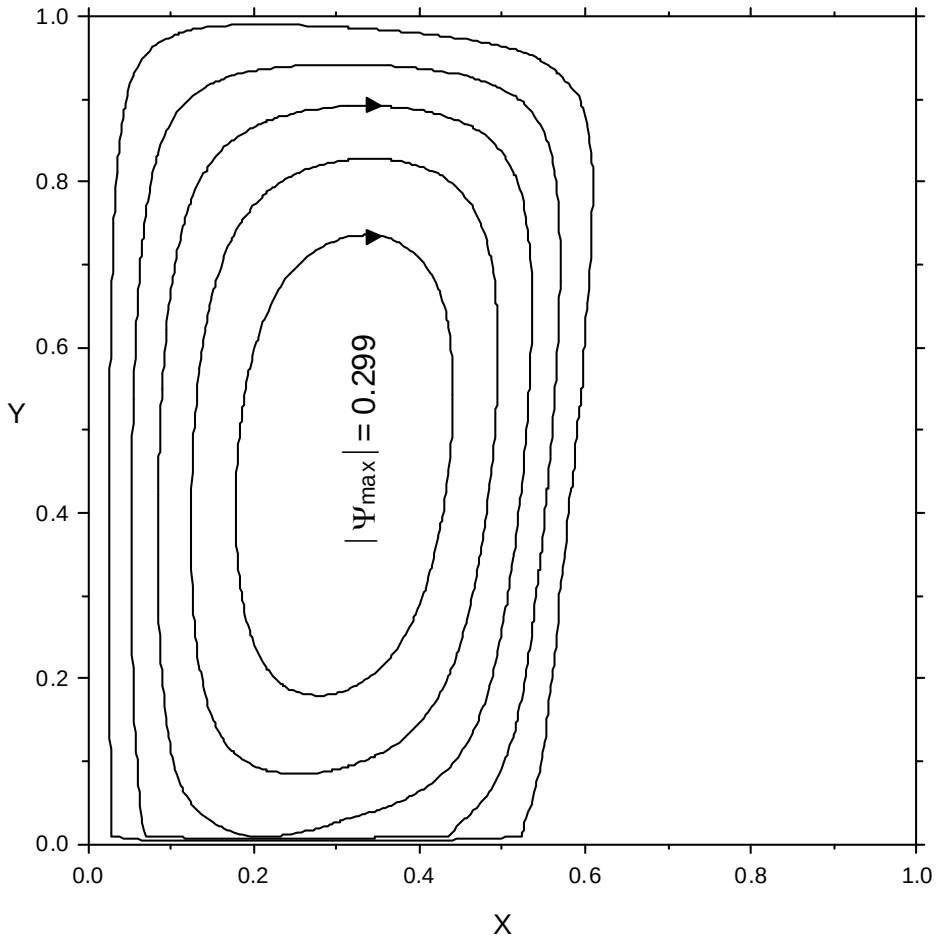

(b)

Fig. 4-14 Streamlines from modified TTM at (a) 5 min and (b) 20 min.

The streamline is then studied as shown in Fig. 4-14 to obtain more information on the solidification process. Fig. 4-14 shows streamline at 5 and 20 minutes to illustrate the development natural convection in solidification process. It is clear that the natural convection is fully-developed and takes place at the entire domain at the beginning. The hot fluid rises toward the top wall and impinges upon the solid causing faster solidification at the bottom. As time passes, the average temperature of bulk fluid is

cooled down making the fluid to move slower. Thus, the difference in solidification rate between the top and bottom wall decreases and consequently the solidification becomes conduction dominated. It may also be seen that the streamline values decreases as the flow develops, which illustrates decreasing average velocity of the liquid flow. It is notable that the temperature and streamline distribution at 20 minute mark are similar to those at steady state (nearly 30 minutes), so it would be wise to get results at the 20 minutes mark and not waste computational time just to reach the real steady state.

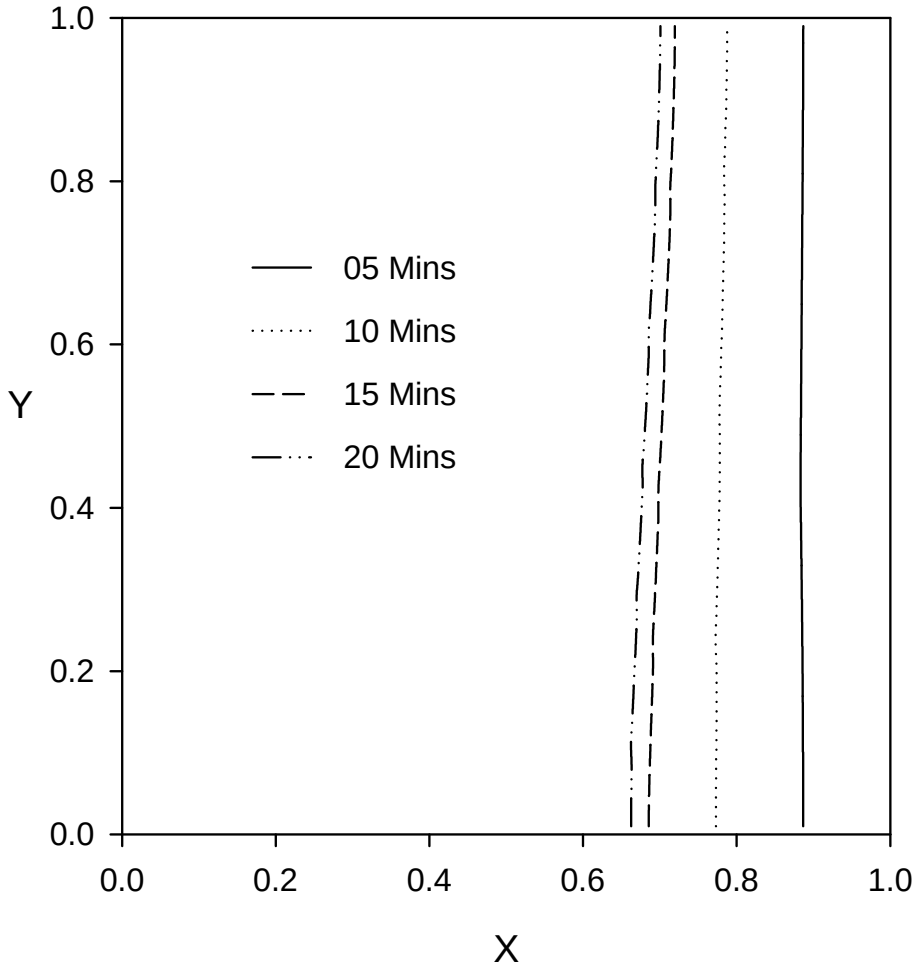

Fig. 4-15 Interface locations at different times for copper-steel combination.

Since the modified TTM can have very strong agreement with experimental and numerical results of Beckermann and Viskanta [54], it can be concluded that the validation of the modified TTM is successful. With full confidence that the modified TTM can give good results for solidification in porous media problems, it is a good idea to apply the model to another combination of materials which is more suitable for real applications. The combination consists of copper as PCM and steel as porous medium. The dimensionless parameters for copper/steel combination case are $Pr = 1.55 \times 10^{-3}$, $Da = 1.37 \times 10^{-5}$, $Ra = 1.28 \times 10^{6}$, $Ste = 0.0295$, $C_{sl} = 0.93$, $C_p = 1.09$, $H = 1.0$, and $\varepsilon = 0.385$. The thermal conductivities used in the calculation of effective thermal conductivity are $k_s = 352$, $k_l = 339$, and $k_p = 30$ W/m.K. Fig. 4-15 shows the solidification process through the movement of the interface at different time. The interface is almost perpendicular to the insulated walls throughout the whole process and there is little sign of convection effects. This illustrates the dominance of conduction in this solidification process. The reason is the effective thermal conductivity of the copper-steel mixture is roughly twice as high as that of the gallium-glass mixture, and this high effective thermal conductivity tends to suppress natural convection flow. Without the convection, the solidification can reach steady state faster at larger volume of fluid.

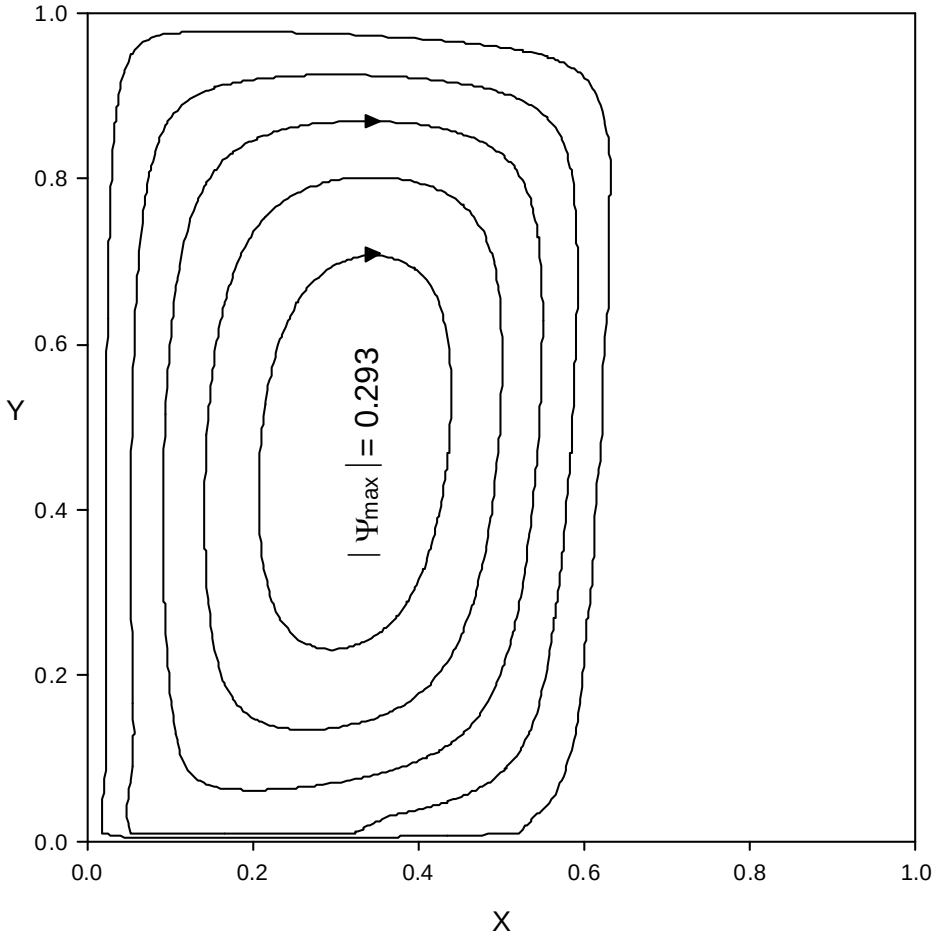

Fig. 4-16 Streamlines for copper-steel combination at 20 min.

Although the solidification is conduction dominated, the natural convection still exists as shown in Fig. 4-16. However, the circulation is too slow to cause any significant effects. The fluid still rises up along the hot wall and falls down along the colder interface, but the impingement very small effects due to the very slow velocity. The temperature distribution in Fig. 4-17 confirms the conduction dominated solidification and the existence of convection. The conduction dominated solidification is represented

through the parallel temperature distribution in the solid region, while slightly incline temperature line shows the effects of convection in the liquid region.

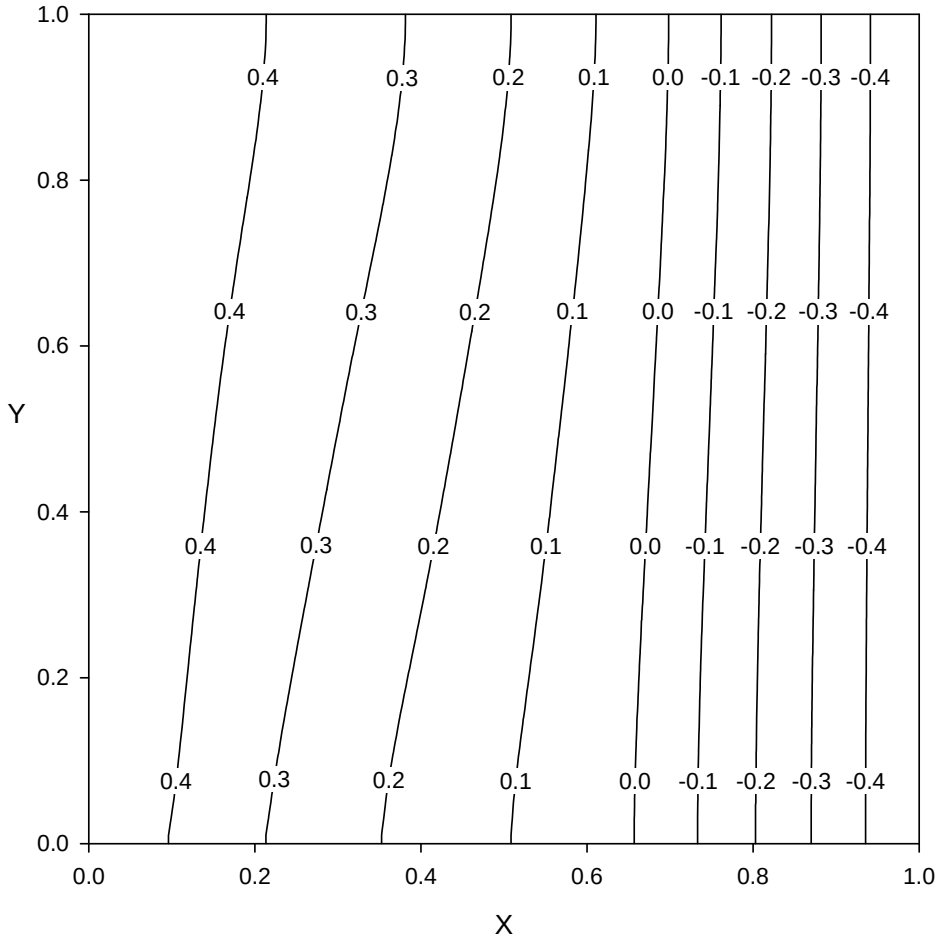

Fig. 4-17 Temperature distribution for copper-steel combination at 20 min.

The changes occurring after we study different materials initiates an interesting question of what parameters actually control the solidification process. After a careful consideration on the parameters involve in the governing equations, there are three parameters that may be the controlling parameters: Rayleigh number, Darcy's number, and the temperature on the cooled wall. To study the effects of these parameters, the only

parameter that is changed is the focused parameter while all other settings were kept unchanged. The first parameter we studied was Rayleigh number as shown in Fig. 4-18. There are three Rayleigh numbers that were studied: 10^5, 10^6, and 10^7. The Rayleigh number of 10^6 is the actual number for copper while two other cases, one with an order of magnitude lower and the other with an order higher, are studied to provide the sole effect of Rayleigh number. Fig. 4-18 shows that the interface becomes more incline when Rayleigh number increases, this means the significant of convection increasing with Rayleigh number. This is because higher Rayleigh number equals the larger body force due to natural convection pushing the fluid to move faster, hence increases convection effects. When the fluid moves faster the effect of impingement is larger, hence it causes more incline interface. On the other hand, when the Rayleigh number decreases below certain order of magnitude, the solidification becomes pure conduction because the fluid moves too slowly for convection to show any effects.

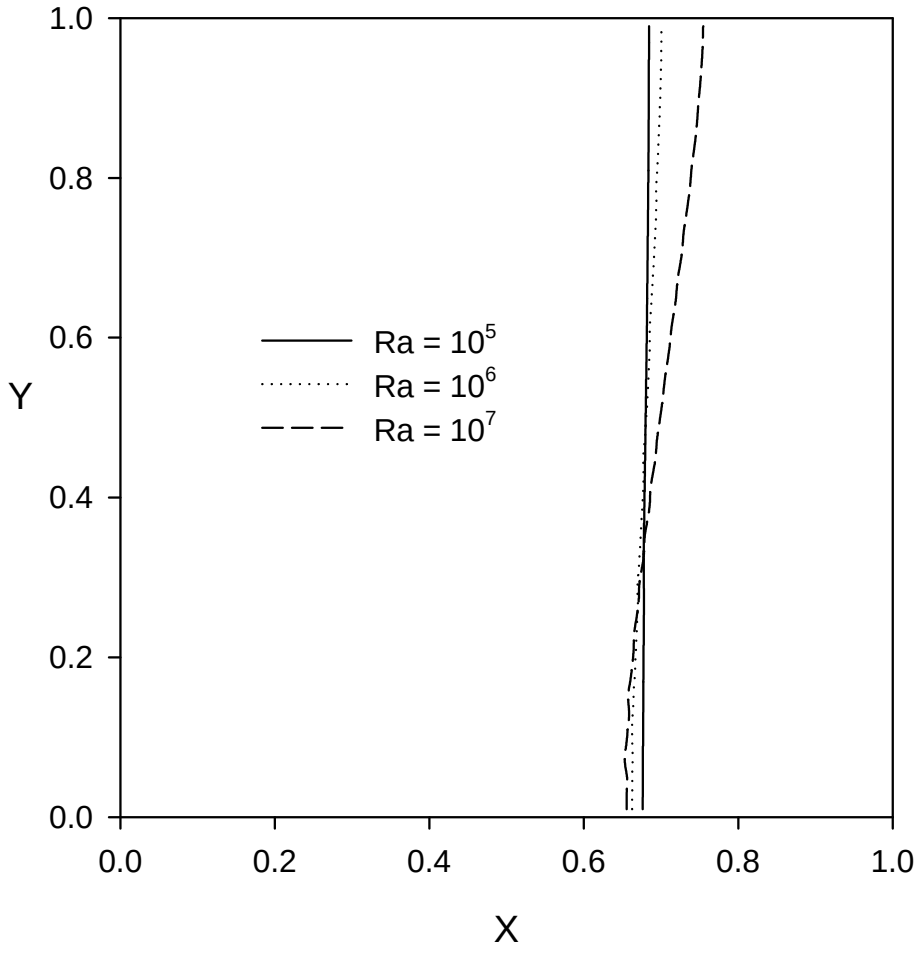

Fig. 4-18 Effects of Rayleigh number on solidification process shown through the slope of the interface.

Effects of Darcy's number is then studied and shown in Fig. 4-19. There are three Darcy's numbers that were studied: 10^{-4}, 10^{-5}, and 10^{-6}. The similar results can be observed in this figure too. The presence of convection also increases with higher Darcy's number. The increasing Darcy's number means that there is less drag forces asserted on the fluid due to the larger holes inside porous medium, which allows fluid to

move with less restriction. When the fluid with same Ra moves with smaller drags it will move with higher speed and consequently promotes convection. Similarly, if Darcy's number decreases below a certain order of magnitude the solidification becomes pure conduction. Such cases are caused by very small diameter of particles in porous bed or very small void space.

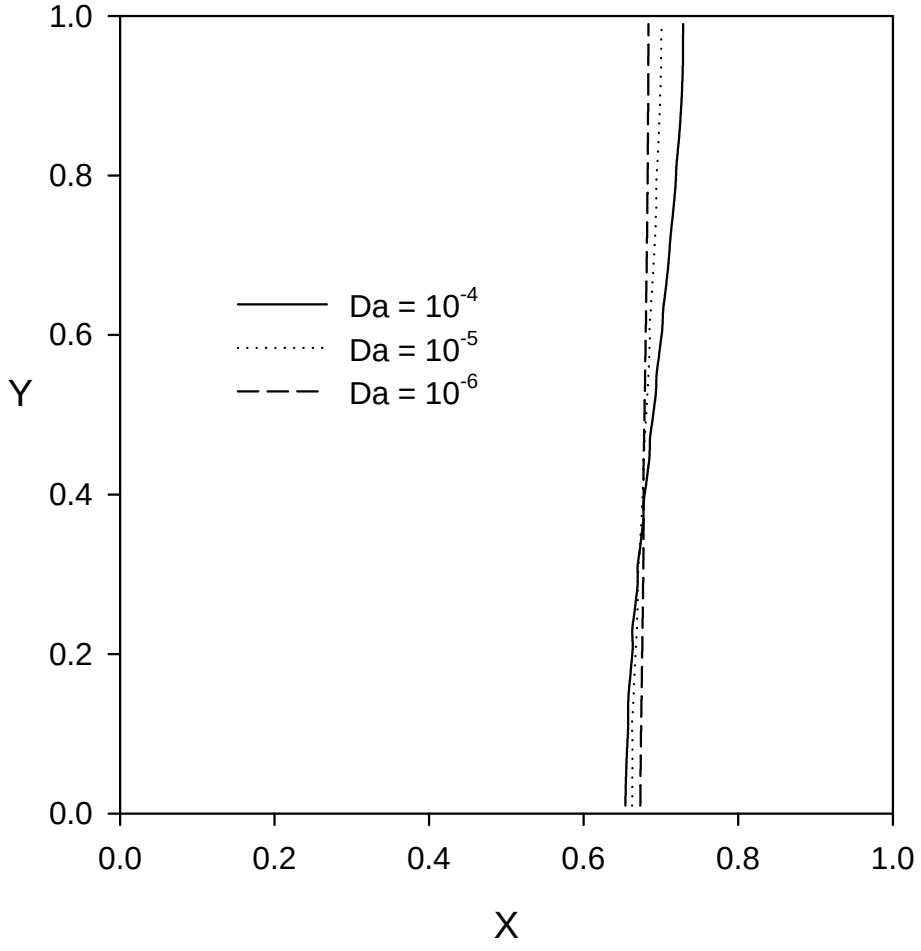

Fig. 4-19 Effects of Darcy's number on solidification process shown through the slope of the interface.

The last parameter is the temperature on the cooled wall shown in Fig. 4-20. The temperature at the hot wall remains the same for three cases of cooled wall temperature: 0.3, 0.5, and 0.7. The results show that the interface moves faster with lower temperature at the cooled wall, but it shows very little change in convection. The interface moves faster because of the higher temperature gradient caused by larger temperature difference between two vertical walls causing higher rate of conduction heat transfer. The results clearly show that the effects of Boussinesq approximation are negligible in this case even though the temperature difference also appears in and one would expect its effects on convection.

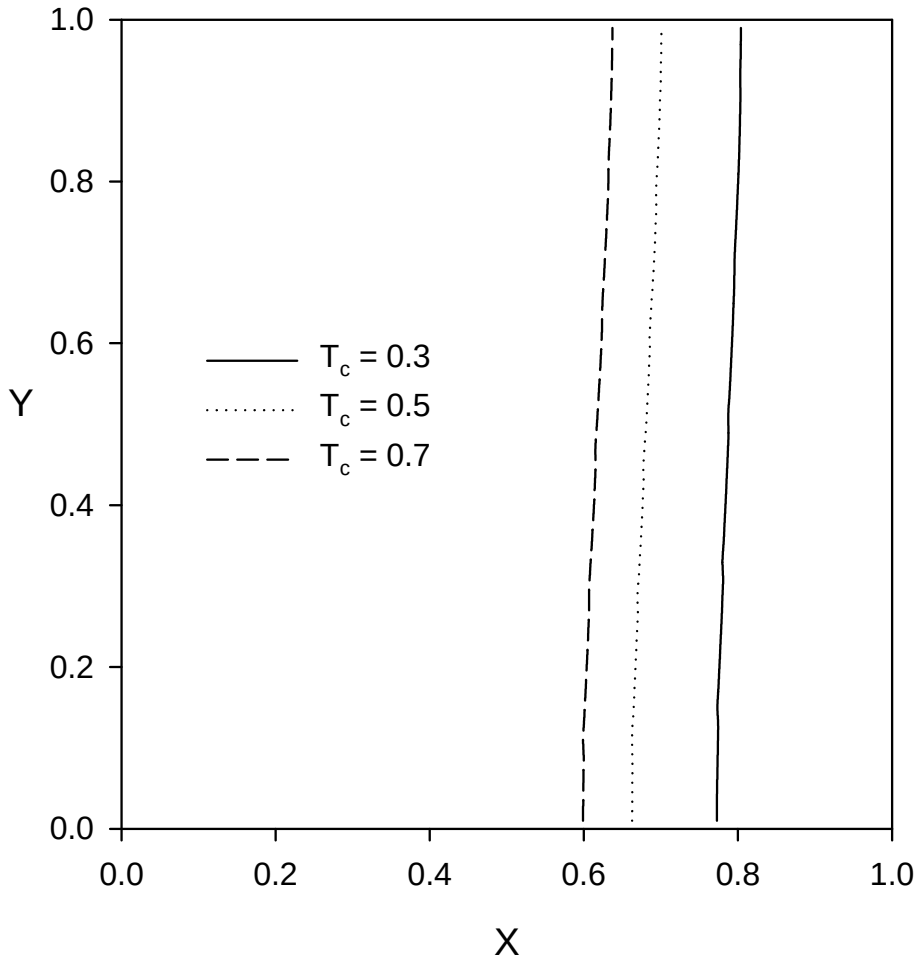

Fig. 4-20 Effects of cooled wall on solidification process shown through the location of the interface.

4.6. Conclusions

The Temperature Transforming Model was modified to improve its performance in cases with large heat capacity difference between solid and liquid phase. The modified TTM was compared with existing experimental and numerical results. The numerical

method used in the comparison was based on a combined energy equation which is wildly used in phase change problems. The modified TTM, however, clearly gave better predictions while the combined energy equation tended to over predict the speed of melting process and under predict the solidification process. After the successful validation of the modified TTM performance on both melting and solidification, it was then used to study a case that is closer to real application. The combination of materials was changed from gallium-glass used in the validation to copper-steel.

For the melting cases, the results confirmed that higher effective thermal conductivity tends to suppress natural convection flow. Such finding led us to consider other parameters that may control the melting process. Rayleigh number, Darcy's number, and subcooling number were carefully studied. It was found that the significant of convection effects increases with Rayleigh number and Darcy's number. The increment of either number results in faster fluid movement, but they do so with different physical prospects. Large Rayleigh number increases body force from natural convection while large Darcy's number reduces drags on the fluid. Both numbers, however, only have small effect conduction because they can only indirectly affect the temperature dissipation. On the other hand, subcooling number only effect the conduction because larger different temperatures on both vertical walls results in higher temperature gradient.

For the solidification cases, the changes in results after considering different materials led to deeper study of more parameters that may control the solidification process. Rayleigh number, Darcy's number, and cooled wall temperature were carefully studied. It was found that the significant of convection effects increases with Rayleigh number and Darcy's number. Large Rayleigh number increases body force from natural

convection while large Darcy's number reduces drags on the fluid. On the other hand, the temperature on the cooled wall only affects the conduction because larger different temperatures on both vertical walls results in higher temperature gradient.

The study on the effects of these parameters will be an excellent tool when we need to preemptively estimate a melting process in everyday applications. Obviously, the modified TTM can be extended into many other research areas. It can be a supreme tool in other processes involving solid/liquid phase change in porous media.

CHAPTER 5 POST-PROCESSING BY INFILTRATION

Selective laser sintering (SLS) [58] is a rapid prototyping/manufacturing technology that can fabricate functional parts from powdered materials by a directed laser beam. Fabrication of a three dimensional part by selective laser sintering is a layer-by-layer additive process that each layer is formed by selectively sintering the powders with a focused laser beam. The laser beam scans a selective area and consolidates thin tracks of powder. Upon completion of sintering of one layer, the whole powder bed is lowered and a fresh powder layer is spread to the build zone. The sintering process is repeated until the entire part is fabricated. Depending on the powder materials, the powder particles can be bond together by glass transition (for amorphous powder, such as polycarbonate), solid state sintering (for ceramic or metal powders) or liquid phase sintering (metal powders). Current state of SLS in terms of material, laser and process control of laser-material interaction were reviewed by Kruth *et al.* [59] and Kumar [60].

The parts produced by SLS with single or multiple components metal powders are usually not fully densified and have porous structure. In order to produce fully densified part, a post-processing is necessary. The existing post processing techniques include sintering, Hot Isostatic Pressing (HIP) [2, 61, 62], and infiltration [3, 63, 64]. Compared to sintering and HIP processes, the advantage of infiltration is that the full density can be achieved *without shrinkage* in the post-processing. The additional advantages of post-processing with infiltration include: it is relative inexpensive and the tooling is similar to casting process. Infiltration is a process where a liquid metal is drawn into the pores of a

solid (part produced by SLS of metal powder) by capillary forces. The liquid, as it advances through the solid, displaces gas(es) from the pores and leaves behind a relatively dense structure. The rate of infiltration is related to the viscosity and surface tension of the liquid, and the pore size of the SLS parts. The infiltration process requires that the liquid is able to wet the solid and that the surface tension of the liquid is high enough to induce capillary motion of the liquid metal into the pores of the porous solid. In addition to capillary force, the infiltration process can also be influenced by the gravitational forces.

In order to allow the liquid metal infiltrate into the pores in the SLS parts, the pore structure generated during SLS need to be interconnected. The large pore size is not desirable because it cannot produce sufficient capillary force to drive the liquid metal flow into the pore structure. On the other hand, small pore size will provide small path for the liquid metal flow and higher friction, which is not favorable to the infiltration. Fluid flow in porous media can find applications in many areas and it is well documented in the literature [57, 65, 66]. While post-processing of laser sintered metal part by liquid metal infiltration and solidification SLS is fairly new, infiltration and solidification have been used in fabrication of Metal-Matrix Composite (MMC) for a long time [5, 67-69]. The progresses on numerical simulation of metal matrix composite and polymer matrix composites processing by infiltration was reviewed by Lacoste et al. [70]. During fabrication of MMC, an external pressure is usually applied to drive the liquid metal into the preform.

When infiltration is employed in the post-processing of the subcooled SLS parts, solidification accompanies the infiltration process. If the initial temperature of the

preform is too low, the solidification of the liquid metal may completely block the path of liquid flow and prevent the liquid metal from thoroughly infiltrate into the pore in the SLS parts. Therefore, the SLS part must be preheated to the temperature near the melting point of the liquid metal. On the other hand, the temperature of the liquid metal that infiltrates the SLS parts must not be too high because melting of the preform may occur and the part may be distorted. Therefore, the temperatures of both liquid metal and preform are important processing parameters of post-processing of laser sintered parts by infiltration. In this paper, infiltration, solidification and remelting of metal in subcooled laser sintered porous structure will be analytically investigated. The temperature distributions in the remelting and uninfiltrated regions were obtained by an exact solution and an integral approximate solution, respectively. A processing map that can aid the selection of various processing parameters will be presented. The effects of porosity, Stefan number, subcooling parameter and dimensionless infiltration pressure will also be investigated.

5.1. Physical Model

Fig. 5-1 shows the physical model of infiltration problem under consideration. The porosity and initial temperature of the preform are uniformly equal to φ and T_i, respectively. At time $t = 0$, the liquid metal with a temperature of T_0 infiltrates to the porous preform due to a pressure difference induced by capillary force. Since the initial temperature of the preform, T_i, is well below the melting point of the liquid metal, heat transfer from liquid metal to the preform takes place as liquid metal infiltrates to the preform.

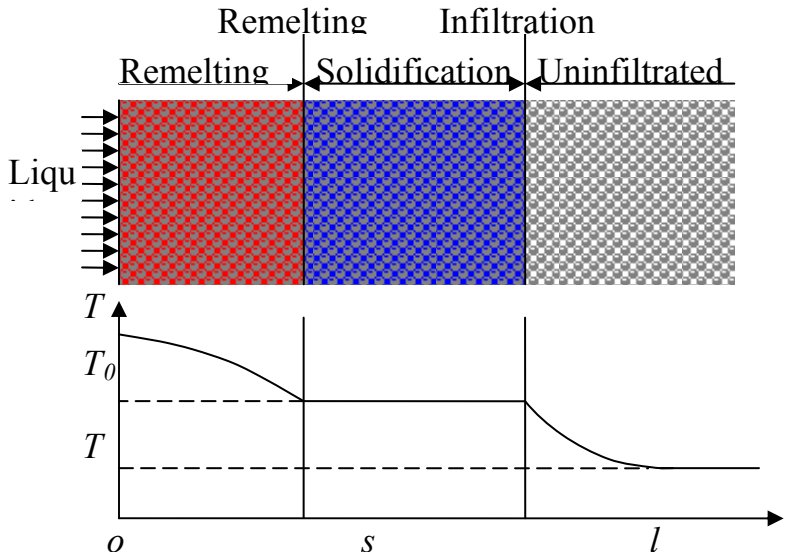

Fig. 5-1 Physical model

As the results, the liquid metal is cooled as it is in contact with the porous preform. Once the temperature of the liquid metal decreases to the melting point, partial solidification of liquid metal occurs and the available flow area for the liquid metal is reduced. As the hot liquid metal flows into the preform, the partially resolidified metal may be remelted. Therefore, there exist three regions: (1) remelting region, (2) solidification region, and (3) uninfiltrated region, separated by two interfaces: (1) remelting front ($x = s$), and (2) infiltration front ($x = l$) (see Fig. 5.1). It is assumed that the liquid metal and the preform are in local thermal equilibrium so that the local instantaneous temperatures of liquid metal and the preform can be represented by a single value. The temperature in the remelting region is higher than the melting point of the liquid metal, while the temperature in the uninfiltrated region is lower than the melting point of the liquid metal. In the solidification region, the temperature is uniformly equal to the melting point of the liquid metal.

In the remelting and solidification regions, the superficial velocity of the liquid metal can be described by Darcy's law:

$$u = -\frac{K}{\mu}\frac{\partial p}{\partial x} \tag{5-1}$$

where K is permeability. In the remelting and solidification regions, eq. (5-1) can be rewritten as:

$$u = \frac{K_1}{\mu}\frac{p_0 - p_s}{s} \tag{5-2}$$

$$u = \frac{K_2}{\mu}\frac{p_s - p_l}{l - s} \tag{5-3}$$

where p_0, p_s, and p_l are the liquid pressures at inlet, remelting front, and infiltration front, respectively. In the remelting region, the permeability can be expressed as

$$K_1 = \frac{d_p^2 \varphi^3}{150(1-\varphi)} \tag{5-4}$$

where d_p is the diameter of the particle in the laser sintered porous preform. In the solidification region, the particle size is increased to d_{ps} due to solidification at the surface of the particle. If the fraction of liquid metal solidified in the solidification region is f, the particle diameter in the solidification region can be obtained by a simple volume balance:

$$\frac{d_{ps}}{d_p} = \left[\frac{1-\varphi(1-f)}{1-\varphi}\right]^{1/3} \tag{5-5}$$

The permeability in the solidification is

$$K_2 = \frac{d_{ps}^2[\varphi(1-f)]^3}{150[1-\varphi(1-f)]} \tag{5-6}$$

where $\varphi(1-f)$ is the porosity in the solidification region. Combining eqs. (5-2) and (5-3) and considering eqs. (5-4) – (5-6), the superficial liquid metal velocity becomes

$$u = \frac{K_1 \Delta p}{\mu\left\{s + (1-f)^3\left[\frac{1-\varphi}{1-\varphi(1-f)}\right]^{1/3}(l-s)\right\}} \tag{5-7}$$

where $\Delta p = p_0 - p_l$ is the pressure difference between the inlet and the infiltration front. For post-processing of the laser sintered metal part, this pressure difference is usually created by capillary force at the infiltration front. The superficial velocity is related to the location of the infiltration front by

$$u = \varphi \frac{dl}{dt} \tag{5-8}$$

Combining eqs. (5-7) and (5-8) yields

$$\varphi \frac{dl}{dt} = \frac{K_1 \Delta p}{\mu\left\{s + (1-f)^3\left[\frac{1-\varphi}{1-\varphi(1-f)}\right]^{1/3}(l-s)\right\}} \tag{5-9}$$

The energy equation in the remelting region is

$$\rho_c c_c \frac{\partial T}{\partial t} + \rho_l c_l u \frac{\partial T}{\partial x} = k_c \frac{\partial^2 T}{\partial x^2},\ 0 < x < s,\ t > 0 \tag{5-10}$$

where the heat capacity and thermal conductivity can be obtained by

$$\rho_c c_c = (1-\varphi)\rho_p c_p + \varphi \rho_l c_l \tag{5-11}$$

$$k_c = (1-\varphi)k_p + \varphi k_l \tag{5-12}$$

where the subscripts p and l represent preform and liquid metal, respectively.

The boundary conditions of eq. (5-10) are

$$T = T_0, \quad x = 0 \tag{5-13}$$

$$T = T_m, \quad x = s \tag{5-14}$$

$$-k_c \frac{\partial T}{\partial x} = \varphi f \rho_l h_{sl} \frac{ds}{dt}, \quad x = s \tag{5-15}$$

In the solidification region, the temperature is uniformly equal to the melting point of the liquid metal so that no governing equation is needed.

The energy equation in the uninfiltrated region is

$$(1-\varphi)\rho_p c_p \frac{\partial T}{\partial t} = k_{p,eff} \frac{\partial^2 T}{\partial x^2}, \ x > l, \ t > 0 \tag{5-16}$$

where the effective thermal conductivity in the uninfiltrated region (sintered metal powder) can be expressed as

$$k_{p,eff} = (1-\varphi)k_p \tag{5-17}$$

Substituting eq.(5-17) into eq.(5-16), the energy equation in the uninfiltrated region becomes

$$\frac{\partial T}{\partial t} = \alpha_p \frac{\partial^2 T}{\partial x^2}, \ x > l, \ t > 0 \tag{5-18}$$

where α_p is the thermal diffusivity of the material in the uninfiltrated region.

The corresponding initial and boundary conditions of eq. (5-16) are:

$$T = T_i, \quad t = 0 \tag{5-19}$$

$$T = T_m, \quad x = l \tag{5-20}$$

$$-(1-\varphi)k_p \frac{\partial T}{\partial x} = \varphi f \rho_l h_{sl} \frac{dl}{dt}, \quad x = l \tag{5-21}$$

$$T = T_i, \quad x \to \infty \tag{5-22}$$

Defining the following dimensionless variables

$$\left.\begin{aligned} X = \frac{x}{L},\ S = \frac{s}{L},\ \Lambda = \frac{l}{L},\ \tau = \frac{\alpha_p t}{L^2},\ U = \frac{uL}{\alpha_p}, \theta = \frac{T - T_m}{T_0 - T_m} \\ Sc = \frac{T_m - T_i}{T_0 - T_m},\ \gamma = \frac{\rho_l c_l}{\rho_p c_p},\ \kappa = \frac{k_l}{k_p}, P = \frac{\Delta p K_1}{\alpha_p},\ \mathrm{Ste} = \frac{c_l (T_0 - T_m)}{h_{sl}} \end{aligned}\right\} \tag{5-23}$$

where L is a characteristic length, eqs. (5-8) – (5-10), (5-13) – (5-15), and (5-18) – (5-22) can be nondimensionalized to

$$U = \varphi \frac{d\Lambda}{d\tau} \tag{5-24}$$

$$\varphi \frac{d\Lambda}{d\tau} = \frac{P}{S + (1-f)^3 \left[\dfrac{1-\varphi}{1-\varphi(1-f)}\right]^{1/3} (\Lambda - S)} \tag{5-25}$$

$$[(1-\varphi) + \varphi\gamma]\frac{\partial \theta}{\partial \tau} + \gamma U \frac{\partial \theta}{\partial X} = [(1-\varphi) + \varphi\kappa]\frac{\partial^2 \theta}{\partial X^2}, \quad 0 < X < S, \ \tau > 0 \tag{5-26}$$

$$\theta = 1, \quad X = 0 \tag{5-27}$$

$$\theta = 0, \quad X = S \tag{5-28}$$

$$\frac{dS}{d\tau} = -[(1-\varphi) + \varphi\kappa]\frac{\mathrm{Ste}}{\gamma\varphi f}\frac{\partial \theta}{\partial X}, \quad X = S \tag{5-29}$$

$$\frac{\partial \theta}{\partial \tau} = \frac{\partial^2 \theta}{\partial X^2}, \quad X > \Lambda, \quad \tau > 0 \tag{5-30}$$

$$\theta = -Sc, \quad \tau = 0 \tag{5-31}$$

$$\theta = 0, \quad X = \Lambda \tag{5-32}$$

$$\frac{d\Lambda}{d\tau} = -\frac{(1-\varphi)\mathrm{Ste}}{\gamma \varphi f} \frac{\partial \theta}{\partial X}, \quad X = \Lambda \tag{5-33}$$

$$\theta = -Sc, \quad X \to \infty \tag{5-34}$$

The infiltration, solidification and remelting problem is now described by eqs. (5-24) – (5-34) and the dimensionless temperature distribution is shown in Fig. 5-2.

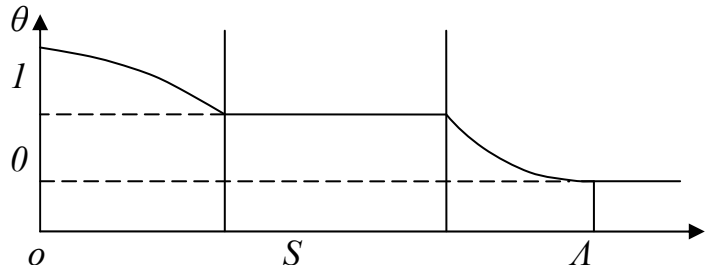

Fig. 5-2 Dimensionless temperature distribution

5.2. Semi Exact Solution

At the point that is sufficiently far away from the infiltration front in the uninfiltrated region, the dimensionless temperature is equal to $-Sc$ as indicated by eq. (5-34). One can define the thermal penetration depth, Δ, beyond which the temperature of the uninfiltrated region is not affected by the liquid metal infiltration (see Fig. 5-2), i.e., the

dimensionless temperature satisfies the following two conditions at the thermal penetration depth

$$\theta(\Delta,\tau) = -Sc \tag{5-35}$$

$$\left.\frac{\partial\theta}{\partial X}\right|_{X=\Delta} = 0 \tag{5-36}$$

Heat transfer in the uninfiltrated region can be solved by using integral approximate solution [13]. Integrating eq. (5-30) in the interval of (Λ, Δ), one obtains

$$\int_{\Lambda}^{\Delta}\frac{\partial\theta}{\partial\tau}dX = \left.\frac{\partial\theta}{\partial X}\right|_{X=\Delta} - \left.\frac{\partial\theta}{\partial X}\right|_{X=\Lambda} \tag{5-37}$$

where the first term on the right-hand side is zero according to eq. (5-36). Equation (5-37) can be rewritten into the following form by using Leibnitz's rule:

$$\frac{d}{d\tau}(\Theta + Sc\Delta) = -\left.\frac{\partial\theta}{\partial X}\right|_{X=\Lambda} \tag{5-38}$$

where

$$\Theta = \int_{\Lambda}^{\Delta}\theta dX \tag{5-39}$$

Assuming the temperature distribution in the uninfiltrated region is a second degree polynomial function and determining the constants using eqs. (5-32), (5-35) and (5-36), one obtains:

$$\theta = Sc\left[\left(\frac{\Delta - X}{\Delta - \Lambda}\right)^2 - 1\right],\ \ \Lambda < X < \Delta \tag{5-40}$$

Substituting eq.(5-40) into eq.(5-38), the following relationship between the thermal penetration depth and the location of infiltration front is obtained:

$$2\frac{d\Lambda}{d\tau}+\frac{d\Delta}{d\tau}=\frac{6}{\Delta-\Lambda} \tag{5-41}$$

Substituting eq. (5-40) into eq. (5-33) yields

$$\frac{d\Lambda}{d\tau}=\frac{2(1-\varphi)\mathrm{Ste}Sc}{\gamma\varphi f(\Delta-\Lambda)} \tag{5-42}$$

Equations (5-41) and (5-42) suggest that both infiltration front and thermal penetration depth are proportional to $\sqrt{\tau}$. Therefore, the infiltration front and the thermal penetration depth can be expressed as:

$$\Lambda=2\lambda\sqrt{\tau} \tag{5-43}$$

$$\Delta=2\delta\sqrt{\tau} \tag{5-44}$$

where λ and δ are two constants that need to be determined. Substituting eqs. (5-43) and (5-44) into eqs. (5-41) and (5-42), the following equations about λ and δ can be obtained:

$$\lambda=\frac{\delta+\sqrt{9\delta^2-24}}{4} \tag{5-45}$$

$$\delta=\lambda+\frac{2(1-\varphi)\mathrm{Ste}Sc}{\gamma\varphi f\lambda} \tag{5-46}$$

It is seen that the solid fraction, *f*, in the solidification region appears in eq. (5-46) and it must be determined before λ and δ can be solved for from eqs. (5-45) and (5-46).

The temperature distribution in the liquid region can be obtained by a similarity solution. Inspired by eqs. (5-43) and (5-44), one can introduce the following similarity variable:

$$\eta = \frac{X}{2\sqrt{\bar{\alpha}_c \tau}} \tag{5-47}$$

where

$$\bar{\alpha}_c = \frac{(1-\varphi)+\kappa\varphi}{(1-\varphi)+\gamma\varphi} \tag{5-48}$$

is the dimensionless thermal diffusivity in the remelting region. The energy equation (5-26) of the remelting region can be transformed into the following ordinary differential equation:

$$\theta'' = -2(\eta - \sigma\lambda)\theta' \tag{5-49}$$

where

$$\sigma = \frac{\gamma\varphi}{[(1-\varphi)+\gamma\varphi]\sqrt{\bar{\alpha}_c}} \tag{5-50}$$

is the heat capacity of liquid in the remelting region. The boundary conditions specified by eqs. (5-27) and (5-28) becomes

$$\theta = 1, \quad \eta = 0 \tag{5-51}$$

$$\theta = 0, \quad \eta = \beta / \sqrt{\bar{\alpha}_c} \tag{5-52}$$

where

$$\beta = \frac{S}{2\sqrt{\tau}} \tag{5-53}$$

is a constant that describes the location of remelting front. The general solution of eq. (5-49) is

$$\theta = C_1 \mathrm{erf}(\eta - \sigma\lambda) + C_2 \tag{5-54}$$

where erf is the error function defined by

$$\mathrm{erf}(\eta) = \frac{2}{\sqrt{\pi}} \int_0^{\eta} e^{-\eta^2} d\eta \tag{5-55}$$

which is an odd function that satisfies $\mathrm{erf}(-\eta) = -\mathrm{erf}(\eta)$. After determining the two constants C_1 and C_2 in eq. (5-54) from eq. (5-51) and (5-52), the temperature distribution in the remelting region becomes

$$\theta = \frac{\mathrm{erf}(\eta - \sigma\lambda) - \mathrm{erf}(\beta / \sqrt{\overline{\alpha}_c} - \sigma\lambda)}{\mathrm{erf}(-\sigma\lambda) - \mathrm{erf}(\beta / \sqrt{\overline{\alpha}_c} - \sigma\lambda)} \tag{5-56}$$

Substituting eq. (5-47) into eq. (5-56) and considering the effort function is an odd function, one obtains:

$$\theta = \frac{\mathrm{erf}[\sigma\lambda - X/(2\sqrt{\overline{\alpha}_c \tau})] - \mathrm{erf}(\sigma\lambda - \beta / \sqrt{\overline{\alpha}_c})}{\mathrm{erf}(\sigma\lambda) - \mathrm{erf}(\sigma\lambda - \beta / \sqrt{\overline{\alpha}_c})} \tag{5-57}$$

Substituting eq. (5-57) into eq. (5-29), the following equation about β is obtained

$$\beta e^{-(\sigma\lambda - \beta/\sqrt{\overline{\alpha}_c})^2} \left[\mathrm{erf}(\sigma\lambda) - \mathrm{erf}(\sigma\lambda - \beta / \sqrt{\overline{\alpha}_c}) \right] = \frac{[(1-\varphi) + \kappa\varphi]\sqrt{\overline{\alpha}_c}\,\mathrm{Ste}}{\gamma\varphi f} \tag{5-58}$$

where the solid fraction, f, in the solidification region is still unknown at this point.

Substituting eqs. (5-43), (5-44), and (5-53) into eq. (5-25), an equation for the solid fraction is obtained as follows

$$(1-f)^3\left[\frac{1-\varphi}{1-\varphi(1-f)}\right]^{1/3}=\frac{P-2\beta\varphi\lambda}{(\lambda-\beta)\varphi\lambda} \tag{5-59}$$

which serves as a bridge between the solutions in the uninfiltrated region and the remelting regions. The infiltration, solidification and remelting problem is now described by four unknowns, δ, λ, β and f, which can be solved iteratively from four algebraic equations (5-45), (5-46), (5-58) and (5-59).

5.3. Results and Discussions

The infiltration, solidification and remelting problem is described by six dimensionless parameters: the heat capacity ratio, γ, thermal conductivity ratio, κ, porosity, φ, Stefan number, Ste, subcooling parameter, *Sc*, and dimensionless pressure difference, *P*. While there is no apparent relationship between these six parameters, improper combination of these parameters may result in complete solidification of the liquid metal near the inlet and further infiltration will not be possible. On the other hand, if the liquid metal inlet temperature and/or the initial are sufficiently high, the solidification region may not appear.

A simple processing map can be obtained by analyzing energy balance when a preform with a small volume, ΔV and porosity φ is infiltrated by the liquid metal. Although the result of such analysis is accurate only if the heat conduction in both remelting and uninfiltrated regions are negligible, it will provide the first order estimation

on the appropriateness of the processing parameters. The amount of sensible heat required to bring the temperature of the preform to the melting point of the liquid metal is $q_{p,s} = (1-\varphi)\Delta V \rho_p c_p (T_m - T_i)$. The amount of sensible heat can be released by the liquid metal when its temperature decreases from its initial value to its melting point is $q_{l,s} = \varphi \Delta V \rho_l c_l (T_0 - T_m)$. If all of the liquid infiltrated into ΔV is solidified, the amount of latent heat released is $q_{l,l} = \varphi \Delta V \rho_l h_{sl}$. Therefore, the condition under which liquid is not completely solidified is $q_{l,s} + q_{l,l} > q_{p,s}$, i.e.,

$$\varphi \Delta V \rho_l c_l (T_0 - T_m) q_{p,s} + \varphi \Delta V \rho_l h_{sl} > (1-\varphi)\Delta V \rho_p c_p (T_m - T_i) \tag{5-60}$$

Substituting eq. (5-23) into eq. (5-60) yields

$$Sc < Sc_{\max} = \frac{\varphi \gamma}{1-\varphi}\left(1 + \frac{1}{\mathrm{Ste}}\right) \tag{5-61}$$

where $Sc_{\max}$ is the maximum allowable subcooling parameter, above which infiltration becomes impossible.

On the other hand, solidification will occur only if $q_{l,s} < q_{p,s}$, i.e.,

$$\varphi \Delta V \rho_l c_l (T_0 - T_m) q_{p,s} < (1-\varphi)\Delta V \rho_p c_p (T_m - T_i) \tag{5-62}$$

Substituting eq. (5-23) into eq. (5-62) yields

$$Sc > Sc_{\min} = \frac{\varphi \gamma}{1-\varphi} \tag{5-63}$$

where $Sc_{\min}$ is the minimum subcooling parameter below which there will be no solidification.

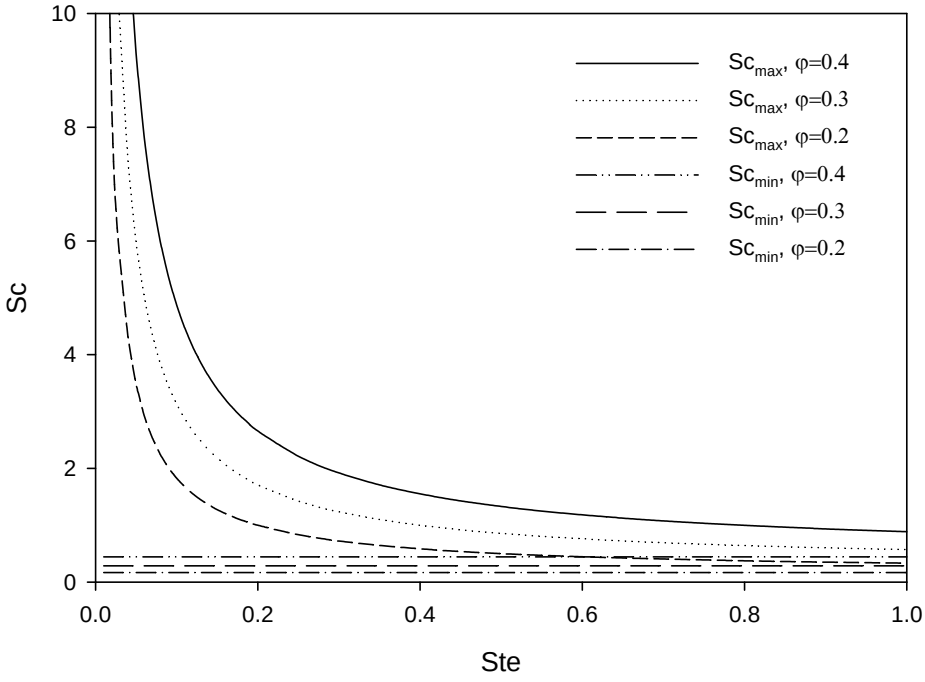

Fig. 5-3 Processing map

Fig. 5-3 shows a processing map for infiltration of liquid aluminum into the preform fabricated by laser sintering copper powder particles. The heat capacity ratio and thermal conductivity ratio for this combination are $\gamma = 0.664$ and $\kappa = 0.257$, respectively. As Stefan number increases, $Sc_{\max}$ significantly decreases while $Sc_{\min}$ is not affected by change of Stefan number. Although $Sc_{\max}$ is the upper limit of subcooling parameter above which infiltration is impossible, $Sc_{\min}$ is only the limit below which no solidification will occur. When Sc is below $Sc_{\min}$, infiltration is still possible except there will be no solidification region and the solution will be much simpler. A subcooling parameter below $Sc_{\min}$ means that the preform must preheated to an initial temperature

very close to the melting of the liquid metal. In this paper, only the cases that the subcooling parameters are between $Sc_{\min}$ and $Sc_{\max}$ will be investigated.

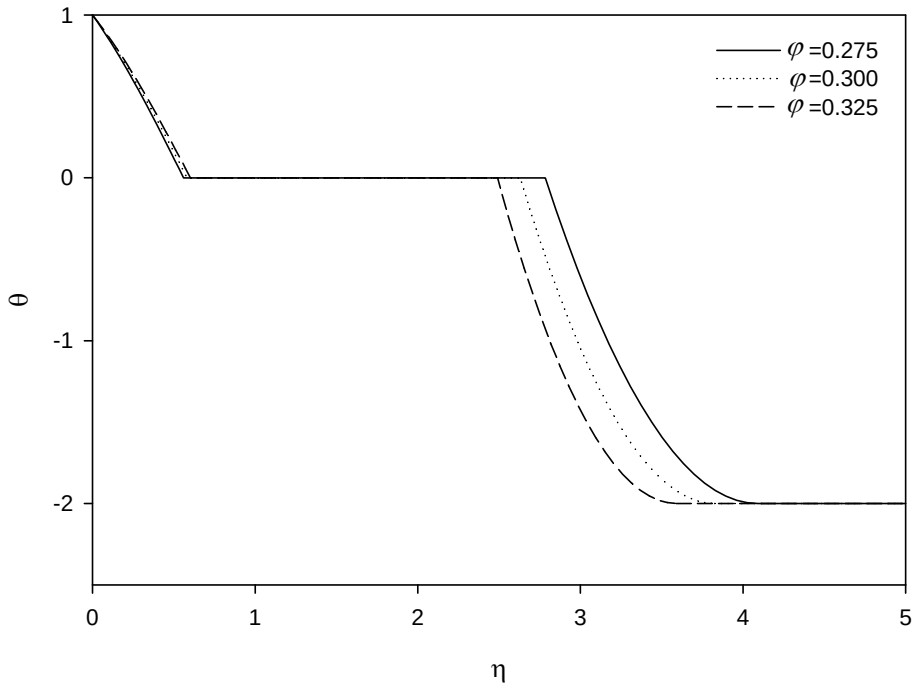

Fig. 5-4 Temperature distributions at different porosity ($\mathrm{Ste} = 0.1,\ Sc = 2,$ and $P = 1.5$)

Fig. 5-4 shows the temperature distributions at different porosity while all other parameters are kept at $\mathrm{Ste} = 0.1,\ Sc = 2,$ and $P = 1.5$. The values of β that represent the locations of remelting front for the three porosities are 0.56, 0.58 and 0.60, respectively. Thus, the velocity of the remelting front slightly increases with increasing porosity. The values of λ that represent the locations of infiltration fronts are 2.78, 2.63, and 2.49, respectively. Therefore, the velocity of infiltration front significantly decreases with increasing porosity. The thermal penetration depth also decreases with increasing porosity. The values of δ that represent the thermal penetration depth are 4.09, 3.82, and

3.59, respectively. The solid fractions for these three cases are 0.436, 0.447, and 0.456, respectively.

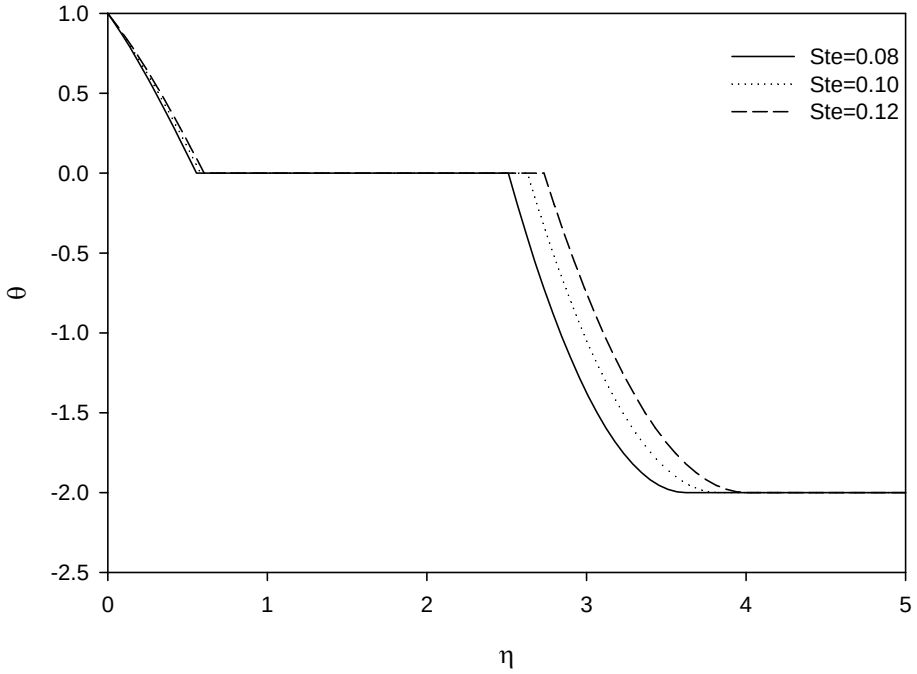

Fig. 5-5 Temperature distributions at different Stefan number

($\varphi = 0.3,\ Sc = 2,$ and $P = 1.5$)

Fig. 5-5 shows the temperature distributions at different Stefan number while all other parameters are kept at $\varphi = 0.3,\ Sc = 2,$ and $P = 1.5$. It can be seen that the velocity of the remelting front slightly increases with increasing Stefan number. The values of β for the three Stefan numbers are 0.56, 0.58 and 0.61, respectively. The effect of Stefan number on the velocity of infiltration front is more significant than its effect on the remelting front: the values of λ for three Stefan numbers are 2.51, 2.63, and 2.73, respectively. The values of δ for the three Stefan numbers are 3.62, 3.82, and 4.00, respectively. The solid

fractions for these three cases are 0.403, 0.447, and 0.486, respectively. The reason that the solid fraction increases with increasing Stefan number (increasing liquid metal inlet temperature) is that the initial temperature of the uninfiltrated region decrease as T_0 increases even Sc is unchanged.

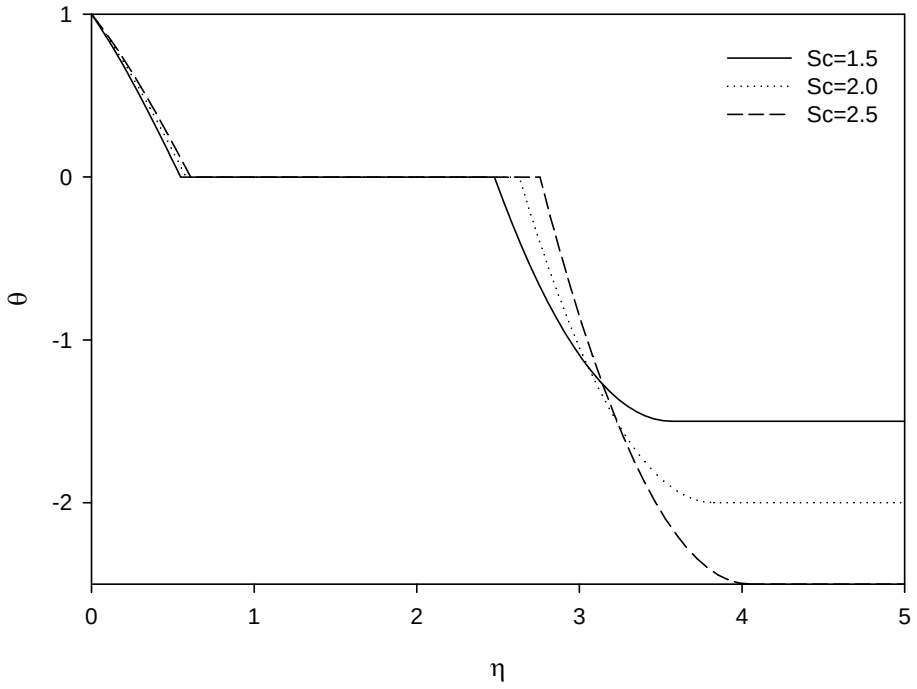

Fig. 5-6 Temperature distributions at different subcooling parameters

$(\mathrm{Ste} = 0.1,\ \varphi = 0.3,\ \text{and}\ P = 1.5)$

Fig. 5-6 shows the temperature distributions at different subcooling parameters while the other parameters are kept at $\mathrm{Ste} = 0.1,\ \varphi = 0.3,\ \text{and}\ P = 1.5$. The velocity of the remelting front slightly increases with increasing subcooling parameter. The values of β for the three subcooling parameters are 0.55, 0.58 and 0.61, respectively. The effect of

subcooling parameter on the velocity of infiltration front is more significant than its effect on remelting front: the values of λ for three subcooling parameters are 2.48, 2.63, and 2.76, respectively. The thermal penetrate depth significantly increase with increasing subcooling: the values of δ for the three subcooling parameters are 3.57, 3.82, and 4.05, respectively. As expected, the solid fraction increases with increasing subcooling parameters: the solid fractions for these three cases are 0.390, 0.447, and 0.495, respectively.

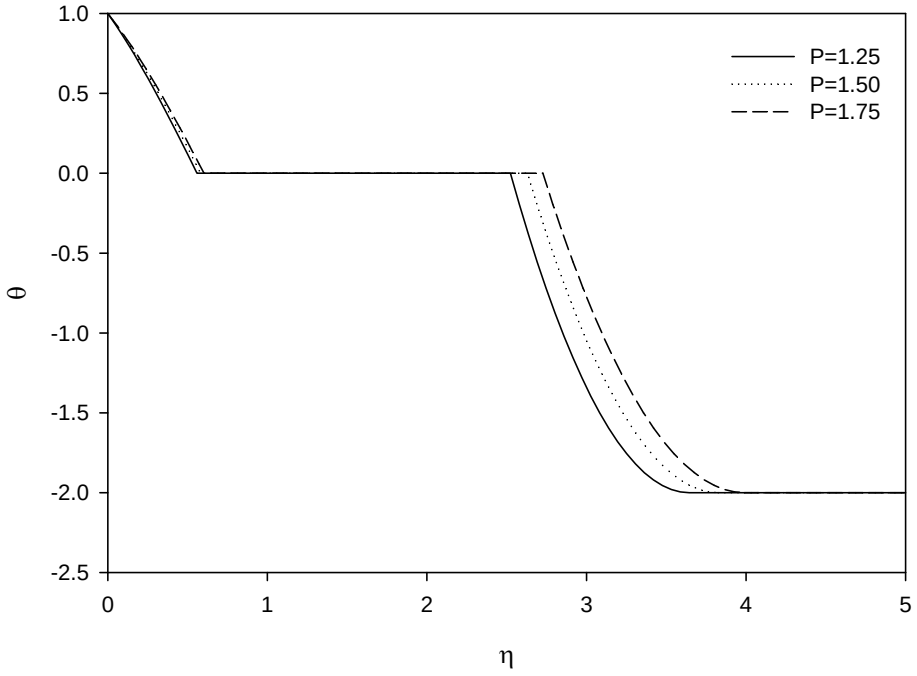

Fig. 5-7 Temperature distributions at different dimensionless pressure differences

($\mathrm{Ste} = 0.1$, Sc=2, and $\varphi = 0.3$)

Fig. 5-7 shows the temperature distributions at different dimensionless pressure differences while the other parameters are kept at $\mathrm{Ste} = 0.1$, Sc=2, and $\varphi = 0.3$. Since the

pressure difference is the driving force for the liquid metal infiltration, higher P allows the liquid metal being pushed further into the uninfiltrated region. The effect of P on β is very insignificant: the values of β for the three pressure differences are 0.56, 0.58 and 0.60, respectively. The effect of pressure difference on the velocity of infiltration front is stronger than its effect on the remelting front: the values of λ for three pressure difference are 2.52, 2.63, and 2.73, respectively. The values of δ for the three subcooling parameters are 3.64, 3.82, and 3.99, respectively. The solid fraction decreases with increasing pressure difference: the solid fractions for these three cases are 0.497, 0.447, and 0.408, respectively.

5.4. Conclusions

Infiltration, solidification and remelting of metal in subcooled laser sintered porous structure are analyzed in this paper. The governing equations are nondimensionlized and the problem is described by six dimensionless parameters: the heat capacity ratio, γ, thermal conductivity ratio, κ, porosity, φ, Stefan number, Ste, subcooling parameter, *Sc*, and dimensionless pressure difference, *P*. A processing map that identifies the conditions of complete solidification and no solidification was obtained by analyzing the overall energy balance of the control volume. As Stefan number increases, the maximum allowable subcooling parameter significantly decreases while the minimum subcooling parameter, below which no melting will occur, is not affected by change of Stefan number.

The effects of porosity, Stefan number, subcooling parameter and dimensionless pressure difference on the infiltration are investigated. The velocity of the remelting front slightly increases with increasing porosity, Stefan number, subcooling parameter, and dimensionless pressure difference. The velocity of infiltration front significantly decreases with increasing porosity, decreasing Stefan number, subcooling parameter, and pressure difference. The solid fraction in the solidification region increase with increasing porosity, Stefan number and subcooling parameter, and decreasing dimensionless pressure difference.

CHAPTER 6 SUMMARY

The main purpose of this research is to develop a weak solution model for solving post-processing by infiltration problem. Unlike many strong solution models that are mostly used be researchers in this area, this weak solution model requires simpler equations and less calculation time. This new model will improve efficiency of future researches in this area. Certain steps are taken in the process of developing this model. The first step was to develop a program that can solve a simple flow inside a porous medium. The second step was to implement TTM model into the program so that it can be used in melting and solidification problems. Those two steps were completed and the model was proved to be accurate and efficient. The next step is to combine the first to step by simplifying the complicated governing equations in melting in porous media problem and using the modified TTM to solve it.

6.1. Flow in Porous Media

A numerical study of transient fluid flow and heat transfer in a porous medium with partial heating and evaporation on the upper surface is performed. The dependence of saturation temperature on the pressure was accounted for by using Clausius-Clapeyron equation. The model was first tested by reproducing the analytical results given in a previous research. A new kind of boundary condition was applied in order to reduce restrictions used in analytical solution and to study changes in velocity and temperature distributions before reaching the steady state evaporation. The results showed that as time

passes the magnitude of velocity increases until the process reached steady state. The maximum velocity occurred near the end of heated plate. Also, the temperature near the heated surface was higher than saturation temperature representing superheated liquid.

Transient fluid flow and heat transfer in a porous medium with partial heating and evaporation on the upper surface was investigated. The numerical model was able to reproduce steady-state analytical solution given by Cao and Faghri (1994). The history of velocity vector and temperature contour from the starting of the process until it reached steady state under new boundary condition is investigated. The results showed that as time passes the magnitude of velocity increases until the process reached steady state. The maximum velocity occurred near the end of heated plate. The temperature near the heated surface was higher than saturation temperature representing superheated liquid.

6.2. Melting in an Enclosure

a modified TTM is proposed to consider the dependence of heat capacity on the fractions of solid and liquid in the mushy zone. The Ramped Switch-Off Method (RSOM) is used for solid velocity correction scheme. The results are then compared with existing experimental and numerical results for a convection/diffusion melting problem in a rectangular cavity. The results show that TTM with the new assumption are closer to experimental results with octadecane as PCM even though its heat capacity ratio is very close to one. The modified TTM is then tested on substances that have heat capacity further from one, such as 0.4437 for water and 1.2034 for acetic acid. The results show that the original TTM under predicts the velocity of the solid-liquid interface when the

heat capacity ratio is less than one and over predicts the velocity when the ratio is higher than one.

A modified TTM was proposed and numerical simulation for three substances were carried out. Even for the PCM with heat capacity ratio close to one, the present model yields results closer to the experimental results than the original TTM. The difference in melting rate prediction becomes larger when the heat capacity ratio is further away from one and that the modified TTM will give better prediction than original TTM. Since the original TTM uses average heat capacity in the mushy zone, it will under predict the location of the interface when heat capacity ratio is less than one and it will over predict when the ratio is larger than one.

6.3. Melting and Solidification in Porous Media

The modified TTM is employed to solve melting in porous media. The model considers the dependence of heat capacity on the fractions of solid and liquid in the mushy zone. The velocity in the solid region is set to zero by the Ramped Switch-Off Method (RSOM). For the liquid region, the momentum equations are modified and two drag forces (Darcy's term and Forchheimer's extension) are included to account for flows in porous media. This model also considers effects of natural convection through Boussinesq approximation. The results show that TTM with the heat capacity dependency are closer to experimental results with gallium as PCM and glass beads as porous structure. The modified TTM is then further used to study affects of various parameters on melting and solidification process in the porous media: Raleigh number,

Darcy number, and initial temperature. The results show that substances with higher Raleigh number will melt faster due to the stronger convection effect. Also, the conduction effect dominates the melting process when the Darcy number is small because there are less spaces for fluid. Obviously, the modified TTM can be extended into many other research areas. It can be a supreme tool in other processes involving solid/liquid phase change in porous media.

6.4. Infiltration

One dimensional selective laser sintering was investigated. Infiltration, solidification and remelting of metal in subcooled laser sintered porous structure are analytically investigated.The governing equations are nondimensionlized and the problem is described using six dimensionless parameters. The temperature distributions in the remelting and uninfiltrated regions were obtained by an exact solution and an integral approximate solution, respectively. The effects of porosity, Stefan number, subcooling parameter and dimensionless infiltration pressure are investigated. A processing map that identifies the conditions of complete solidification and no solidification was obtained by analyzing the overall energy balance of the control volume. As Stefan number increases, the maximum allowable subcooling parameter significantly decreases while the minimum subcooling parameter, below which no melting will occur, is not affected by change of Stefan number. The velocity of the remelting front slightly increases with increasing porosity, Stefan number, subcooling parameter, and dimensionless pressure difference. The velocity of infiltration front significantly decreases with increasing porosity, decreasing Stefan number, subcooling parameter, and pressure difference. The solid

fraction in the solidification region increase with increasing porosity, Stefan number and subcooling parameter, and decreasing dimensionless pressure difference

REFERENCES

[1]. M'Hamdi, M., Mo, A., and Martin, C. L., 2002, "Two-phase modeling directed toward hot tearing formation in aluminum direct chill casting," Metallurgical and Materials Transactions A: Physical Metallurgy and Materials Science, 33(7): pp. 2081-2093.

[2]. Das, S., Beaman, J. J., Wohlert, M., and Bourell, D. L., 1998, "Direct Laser Freeform Fabrication of High Performance Metal Components," Rapid Prototyping Journal, 4: pp. 112-117.

[3]. Sindel, M., Pintat, T., Greul, M., Nyrhilaa, O., and Wilkening, C., Direct Laser Sintering of Metals and Metal Infiltration for Near Net Shape Fabrication of Components, in Proceedings of Solid Freeform Fabrication Symposium 1994. 1994. p. 102.109.

[4]. Stierlen, P. and Eyerer, P., 1999, "Si/SiC-Ceramics Prototyping via LS2I – Process (Liquid Silicon Infiltration of Laser Sintered C-SiC Parts)," *Proceedings of Solid Freeform Fabrication Symposium 1999*.

[5]. Tong, X. and Kahn, J. A., 1996, "Infiltration and Solidfication/Remelting of a Pure Metal in a Two-Dimensional Porous Preform," ASME Journal of Heat Transfer, 118: pp. 173-180.

[6]. Viskanta, R., ed. Phase Change Heat Transfer. Solar Heat Storage: Latent Heat Materials, ed. G.A. Lane. 1983, CRC Press: Boca Raton, FL.

[7]. Yao, L. C. and Prusa, J., 1989, "Melting and freezing," Advances in Heat Transfer, 19(1): pp. 1-96.

[8]. Zhang, Y. and Faghri, A., 1996, "Semi-Analytical Solution of Thermal Energy Storage System with Conjugate Laminar Forced Convection," Int. J. Heat Mass Transfer, 39(4): pp. 717-724.

[9]. Zhang, Y. and Faghri, A., 1996, "Heat Transfer Enhancement in Latent Heat Thermal Energy Storage System by Using an External Radial Finned Tube," Int. J. Heat Mass Transfer, 3: pp. 119-127.

[10]. Zhang, Y. and Faghri, A., 1996, "Heat transfer enhancement in latent heat thermal energy storage system by using the internally finned tube," International Journal of Heat and Mass Transfer, 39(15): pp. 3165-3173.

[11]. Voller, V. R., *An Overview of Numerical Methods for Solving Phase Change Problems, in W. J. Minkowycz and E. M. Sparrow (Eds)*, in Advances in Numerical Heat Transfer. 1997, Taylor & Francis, Basingstoke.

[12]. Sasaguchi, K., Ishihara, A., and Zhang, H., 1996, "Numerical Study on Utilization of Melting of Phase Change Material for Cooling of a Heated Surface at a Constant Rate," Numerical Heat Transfer Part A, 29: pp. 19-31.

[13]. Binet, B. and Lacroix, M., 2000, "Melting from heat sources flush mounted on a conducting vertical wall," International Journal of Numerical Methods for Heat and Fluid Flow, 10(3): pp. 286-306.

[14]. Morgan, K., 1981, "A Numerical Analysis of Freezing and Melting with Convection," Computer Methods in Applied Mechanics and Engineering, 28(3): pp. 275-284.

[15]. Hsiao, J. S., 1984, "An Efficient Algorithm for Finite Difference Analysis of Heat Transfer with Melting and Solidification," ASME paper (84-WA/HT-42).

[16]. Cao, Y. and Faghri, A., 1990, "Numerical analysis of phase-change problems including natural convection," Journal of Heat Transfer, 112(3): pp. 812-816.

[17]. Voller, V. R., 1987, "An Enthalpy Method for Convection/Diffusion Phase Change," Int. J. Num. Meth. Eng., 24: pp. 271-284.

[18]. Yang, M. and Tao, W. Q., 1992, "Numerical study of natural convection heat transfer in a cylindrical envelope with internal concentric slotted hollow cylinder," Numerical Heat Transfer; Part A: Applications, 22(3): pp. 289-305.

[19]. Ma, Z. and Zhang, Y., 2006, "Solid velocity correction schemes for a temperature transforming model for convection phase change," International Journal of Numerical Methods for Heat and Fluid Flow, 16(2): pp. 204-225.

[20]. Bazzo, E. and Riehl, R. R., 2003, "Operation characteristics of a small-scale capillary pumped loop," Journal of Applied Thermal Engineering, 23: pp. 687-705.

[21]. Dupont, V., Joly, J. L., Miscevic, M., and Platel, V., 2003, "Capillary pumped loop startup: Effects of the wick fit on Boiling Incipience," Journal of Thermophysics and Heat Transfer, 17(2): pp. 138-144.

[22]. Chen, P. C. and Lin, W. K., 2001, "The application of capillary pumped loop for cooling of electronic component," Journal of Applied Thermal Engineering, 21: pp. 1739-1754.

[23]. Mo, B., Ohadi, M. M., Dessiatoun, S. V., and Wrenn, K. R., 2000, "Capillary pump loop thermal performance improvement with electrohydrodynamic technique," Journal Thermophysics and Heat Transfer, 14(1): pp. 103-108.

[24]. Yan, Y. H. and Ochterbeck, J. M., 2003, "Numerical Investigation of the Steady-State Operation of a Cylindrical Capillary Pumped Loop Evaporator," Journal of Electronic Packaging, 125: pp. 251-260.

[25]. Chung, T. J., Park, J. H., Choi, C. K., and Yoon, D. Y., 2002, "The onset of vortex instability in laminar forced convection flow through a horizontal porous channel," International Journal of Heat and Mass Transfer, 45: pp. 3061-3064.

[26]. Poulikakos, D., 1984, "Maximum density effects on natural convection in a porous layer differentially heated in the horizontal direction," International Journal of Heat and Mass Transfer, 27: pp. 2067-2075.

[27]. Stamp, D. W., Arpaci, V. S., and Clark, J. A., 1990, "Unsteady three-dimensional natural convection in a fluid saturated porous medium," Journal of Fluid Mechanics, 213: pp. 377-396.

[28]. Kubitschek, J. P. and Weidman, P. D., 2003, "Stability of a fluid-saturated porous medium heated from below by forced convection " International Journal of Heat and Mass Transfer, 46: pp. 3697-3705.

[29]. Cao, Y. and Faghri, A., 1994, "Analytical solutions of flow and heat transfer in a porous structure with partial heating and evaporation on the upper surface," International Journal of Heat and Mass Transfer, 37(10): pp. 1525-1533.

[30]. Huang, X. Y. and Liu, C. Y., 1996, "The pressure and velocity fields in the wick structure of a localized heated flat plate heat pipe," International Journal of Heat and Mass Transfer, 39(6): pp. 1325-1330.

[31]. Mantelli, M. B. H. and Bazzo, E., 2000, "Solar absorber plates: Design and Application to Microgravity Capillary-Pumped-Loop Experiments," Journal of Spacecraft and Rockets, 37(1): pp. 100-107.

[32]. Laclair, T. J. and Mudawa, I., 2000, "Thermal Transients in a Capillary Evaporator Prior to the Initiation of Boiling," Int. J. Heat Mass Transfer, 43: pp. 3937-3952.

[33]. Pouzet, E., Joly, J. L., Paltel, V., Grandpeix, J. Y., and Butto, C., 2004, "Dynamic Response of a Capillary Pumped Loop Subjected to Various Heat Load Transients," International Journal of Heat and Mass Transfer, 47: pp. 2293-2316.

[34]. Pantankar, S. V., ed. Numerical Heat Transfer and Fluid Flow. 1980, McGraw-Hill: New York.

[35]. Okada, M., 1984, "Analysis of heat transfer during melting from a vertical wall," International Journal of Heat and Mass Transfer, 27(11): pp. 2057-2066.

[36]. Ho, C. J. and Chu, C. H., 1993, "The melting process of ice from a vertical wall with time-periodic temperature perturbation inside a rectangular enclosure," International Journal of Heat and Mass Transfer, 36(13): pp. 3171-3186.

[37]. Lunardini, V. J., *Heat Transfer in Cold Climates*, 1981, Van Nostrand Co.: New York.

[38]. Albin, F. V., Srinivasamurthy, S., and Krishnamurthy, M. V., Analysis of the food freeze drying process with predetermined surface temperature variation, in Drying '82, A.S. Mazumdar, Editor. 1982, Hemisphere Publishing Corp.: Washington, DC. p. 151-156.

[39]. Sager, F. J., 1968, "Ground freezing in Construction," ASCE Mechanics and Foundations Division, 94: pp. 131-158.

[40]. Meng, Y. and Thomas, B. G., 2003, "Heat-Transfer and Solidification Model of Continuous Slab Casting: CON1D," Metallurgical and Materials Transactions B: Process Metallurgy and Materials Processing Science, 34(5): pp. 685-705.

[41]. Del Borrello, C. and Lacoste, E., 2003, "Numerical simulation of the liquid flow into a porous medium with phase change: Application to metal matrix composites processing," Numerical Heat Transfer; Part A: Applications, 44(7): pp. 723-741.

[42]. Sasaguchi, K., Kusano, K., and Nishimizu, N., 1993, "Solid/liquid phase change heat transfer in porous media (Effects of fins on the solidification process)," Heat Transfer - Japanese Research, 22(4): pp. 398-415.

[43]. Kisdarjono, H., Voutsas, A. T., and Solanki, R., 2003, "Three-dimensional simulation of rapid melting and resolidification of thin Si films by excimer laser annealing," Journal of Applied Physics, 94(7): pp. 4374-4381.

[44]. Chen, T. and Zhang, Y., 2003, "Melting and resolidification of a two-component metal powder layer heated by a moving Gaussian heat source," *American Society of Mechanical Engineers, Heat Transfer Division, (Publication) HTD*.

[45]. Zhang, Y., Faghri, A., Buckley, C. W., and Bergman, T. L., 2000, "Three-Dimensional Sintering of Two-Component Metal Powders with Stationary and Moving Laser Beams," ASME J. Heat Transfer, 122(1): pp. 150-158.

[46]. Ganesh, R. K., Faghri, A., and Hahn, Y., 1997, "A generalized thermal modeling for laser drilling process - I. Mathematical modeling and numerical

methodology," International Journal of Heat and Mass Transfer, 40(14): pp. 3351-3360.

[47]. Ganesh, R. K., Faghri, A., and Hahn, Y., 1997, "A generalized thermal modeling for laser drilling process - II. Numerical simulation and results," International Journal of Heat and Mass Transfer, 40(14): pp. 3361-3373.

[48]. Cao, Y. and Faghri, A., 1991, "Performance characteristics of a thermal energy storage module: a transient PCM/forced convection conjugate analysis," International Journal of Heat and Mass Transfer, 34(1): pp. 93-101.

[49]. Cao, Y., Faghri, A., and Juhasz, A., 1991, "PCM/forced convection conjugate transient analysis of energy storage systems with annular and countercurrent flows," Journal of Heat Transfer, 113(1): pp. 37-42.

[50]. Zhang, Y. and Faghri, A., 1995, "Analysis of forced convection heat transfer in microencapsulated phase change material suspensions," Journal of Thermophysics and Heat Transfer, 9(4): pp. 727-732.

[51]. Haeupl, P. and Xu, Y., 2001, "Numerical simulation of freezing and melting in porous materials under the consideration of the coupled heat and moisture transport," Journal of Thermal Envelope and Building Science, 25(1): pp. 4-31.

[52]. Harlan, R. L., 1973, "ANALYSIS OF COUPLED HEAT-FLUID TRANSPORT IN PARTIALLY FROZEN SOIL," WAT. RESOUR. RES., 9(5).

[53]. Harris, K. T., Haji-Sheikh, A., and Agwu Nnanna, A. G., 2001, "Phase-change phenomena in porous media - a non-local thermal equilibrium model," International Journal of Heat and Mass Transfer, 44(8): pp. 1619-1625.

[54]. Beckermann, C. and Viskanta, R., 1988, "Natural convection solid/liquid phase change in porous media," International Journal of Heat and Mass Transfer, 31(1): pp. 35-46.

[55]. Chang, W. J. and Yang, D. F., 1996, "Natural convection for the melting of ice in porous media in a rectangular enclosure," International Journal of Heat and Mass Transfer, 39(11): pp. 2333-2348.

[56]. Ward, J. C., 1964, "Turbulent flow in porous media," ASCE J. Hydraul. Div., 90(HY5): pp. 1-12.

[57]. Faghri, A. and Zhang, Y., *Transport Phenomena in Multiphase Systems*, 1st ed, 2006, Elsevier Inc.

[58]. Beaman, J. J., Barlow, J. W., Bourell, D. L., Crawford, R. H., Marcus, H. L., and Mcalea, K., eds. Solid Freeform Fabrication: A New Direction in Manufacturing. 1997, Kluwer Academic Publishers: Dordrecht.

[59]. Kruth, J. P., Wang, X., Laoui, T., and Froyen, L., 2003, "Lasers and Materials in Selective Laser sintering," Rapid Prototyping Journal, 23(4): pp. 357-371.

[60]. Kumar, S., 2003, "Selective laser sintering: A qualitative and objective approach," J. Minerals, Metals, Material Society, 55(10): pp. 43-47.

[61]. Das, S., Beaman, J. J., and Bourell, D. L., 1998, "Producing Metal Parts with Selective Laser Sintering/Hot Isostatic Pressing," Journal of Materials, 50: pp. 17-20.

[62]. Wohlert, M., Bourell, D. L., Das, S., and Beaman, J. J., 2000, "Application of Powder Densification Maps to Direct Metal SLS/HIP Processing," *Proceedings of Solid Freeform Fabrication Symposium 2000*.

[63]. Nield, D. A. and Bejan, A., eds. Convection in Porous Media. 1992, Springer-Verlag: New York.

[64]. Wohlert, M., Bourell, D. L., and Beaman, J. J., Production of Full Density Metal-Matrix Composites by a Combined Selective Laser Sintering/Metal Infiltration Process, in Processing and Fabrication of Advanced Materials V, T.M. Srivatsan and J.J. Moore, Metals & Materials Society, Editor. 1996. p. 293-302.

[65]. Faghri, A., ed. Heat Pipe Science and Technology. 1995, Taylor & Francis: Bristol, PA.

[66]. Kaviany, M., ed. Princeples of Heat Transfer in Porous Media. 2nd ed. 1995, Springer Verlag: New York.

[67]. Masur, L. J., Mortensen, A., Comie, J. A., and Flemings, M. C., 1989, "Infiltration of Fibrous Preform by a Pure Metal: Part II. Experiment," Metall. Trans. A. , 20A: pp. 2549-2557.

[68]. Mortensen, A., Comie, J. A., and Flemings, M. C., 1988, "Solidification Processing of Metal-Matrix Composites," J. of Metals, 40(2): pp. 12-19.

[69]. Mortensen, A., Masur, L. J., Comie, J. A., and Flemings, M. C., 1989, "Infiltration of Fibrous Preform by a Pure Metal: Part I. Theory," Metall. Trans. A. , 20A: pp. 2535-2547.

[70]. Lacoste, E., Mantaux, O., and Danis, M., 2002, "Numerical Simulation of Metal Matrix Composites and Polymer Matrix Compotes Processing by Infiltration: A Review," Composites, Part A., 33: pp. 1605-1614.

VITA

Piyasak Damronglerd was born and grown up in Bangkok, the capital city and the highest populated city in Thailand. After attending elementary, middle, and high schools at Chulalongkorn University Demonstation School, He took entrance exam to further my study in university level. He was able to received B.S.from the Engineering Department at Chulalongkorn University, the number one ranked department in the country. Then He received M.S. from Southern Illinois University Edwardsville.